Developing Applications of Atomic Force Microscopy in Cellular Imaging and Mechanical Property Measurement

by

Tong Liu

A thesis
presented to the University of Waterloo
in fulfillment of the
thesis requirement for the degree of
Master of Applied Science
in
Mechanical Engineering

Waterloo, Ontario, Canada, 2014

Author's Declaration

I hereby declare that I am the sole author of this thesis. This is a true copy of the thesis, including any required final revisions, as accepted by my examiners.

I understand that my thesis may be made electronically available to the public.

Abstract

Health of human body is strongly associated with the mechanical properties of living cells. Here, atomic force microscope (AFM) was applied to obtain surface microscopy of individual and non-individual biological cells, which is essential to determining the cell migration behavior for studying the pathogenesis. In order to track a single cell and measure its deformation, digital image correlation (DIC) technique was performed on AFM images. Unlike ordinary optical images, AFM images are composed of massive spatial information. Thus, image reconstruction and specific two-dimension DIC codes were developed and optimized by using MATLAB, and then applied to images of cells. The results of this study showed the capability of DIC as a cell migration tracker and suggested the potential as a deformation sensor, or even a diagnosing tool for the onset and progression of disease.

Mechanical properties (elastic moduli) of live and dead human corneal epithelial cells (HCECs) were also presented in this thesis. All of the modulus measurements were achieved by using AFM nano-indentation technique. In the calculation of elasticity, the most commonly used model is Hertzian model. An overview of the Hertzian model with the assumptions and resulting limitations for the use on cells were discussed in detail. This study had been extended to find elastic moduli distribution of a single cell and compare the elastic moduli difference between living and dead cells. It showed that the center part of a cell was less stiff than the outer part; moreover, Young's modulus increased from 8-20 kPa to 33-101 kPa after the cells died. Lastly, investigation on whether changes in the elastic modulus of the substrate affected HCECs was performed. The results indicated that the stiffness of HCECs increased as the substrate became stiffer.

Keywords: atomic force microscopy, topography, cells, young's modulus

Acknowledgements

I would like to express my sincere gratitude to my supervisor, Dr. HJ Kwon, for giving me a chance to know about digital image correlation technology and applications of AFM. He provided me with his knowledgeable guidance and invaluable experience throughout my M.A.Sc program. I want to show him my appreciation for not only the academic aspect, but also his continuous support and encouragements in my daily life. Without his considerate help, it would be much tougher for me, especially as an international student, to fulfil the degree smoothly.

Many thanks also go to my project colleague Sara, who helped me with my research and sample preparation. Without her, I could not have my research done. I would like to thank my lab seniors: Hyunsung Jung and Bonghun Shin for sharing their abundant industry experience and interpersonal knowledge that would help me greatly throughout my life and future career. Moreover, my thanks go to Jiwon Lee for his best friendship and creating a cheerful working environment.

I would like to show my deepest thanks to my parents for their constant mental support throughout my M.A.Sc program. Finally, I express my thanks to my girlfriend, Yue Dong, for her love, understanding, and all she did to me through these years. I think this achievement contains their efforts and supports as well.

Table of Contents

List of Figures

List of Tables

Chapter 1
Introduction

In 1665, when British Scientist Robert Hooke observed a thin cutting of cork he found empty spaces contained by walls, and termed them 'cells'[1]. This is the first discovery of cells in the history of human civilization. Since then, people started the process of studying, understanding, and learning from cells. Schleiden and Schwann stated that all living organisms are composed of one or more cells in their book [2] and introduced to the world the unit of life – the "cell". Because of this notion of life unit, cell is tied to all kinds of life related fields, such as biology, agriculture, and medical science. Among these fields, medical science is especially important since it is closely related to our health and life. Through the practical studies of cells (i.e. bioengineering and biomechanics), people could seek out the pathogenesis of various disease and eventually develop corresponding medicine and treatment methods.

After the first cell was observed by Robert Hooke, scientist and researchers have kept exploring the "secrets" of cells. The structure and morphology of normal and diseased cells, and of disease-causing microorganisms, were observed for the first time using the light microscope [3]. Then in the 1930s, accompanied with the birth of first transmission electron microscope (TEM) with twice resolution of a light microscope, our perception of cells had been furthered again. A number of subcellular organelle were discovered and their functions were determined using the electron microscope [4, 5, 6, 7]. Viruses, the new life forms, were studied and implicated in diseases ranging from the common cold to autoimmune disease (AIDS) [8]. Despite electron microscope dawned a new era with the resolution at near nanometer, morphological alterations resulted in biological sample processing remained a major concern. Until 1980s, scanning probe microscopy was invented, which extend our perception to the near atomic realm. One of such scanning probe microscope, the atomic force microscope (AFM) broke the magnification limitations of light microscope and overcame the drawback of electron microscope [9]. The dominant advantage of AFM is that it provided a platform for 2D&3D imaging and manipulating living cells to nanometer resolution in real time, thereby enabling us to address questions in key area of cell studies, including connecting structures and function of cells [10, 11, 12], measuring forces in biology [13, 14], single-molecule mechanics [15, 16, 17, 18, 19], cell migration and tissue formation [20, 21], cell division and shape [22, 23], and microbial pathogenesis [24, 25, 26]. Because of its superior performance, AFM has been widely using in recent research and scientific studies.

Populations of cells are almost always heterogeneous in function and fate [27]. To understand cells in more detail, it is vital to measure quantitatively and dynamically the processes that underlie cells in single form. However, living cells exhibit slow migrations and tend to gather together into small colonies inherently, which may affect the measurements on specific single cell. Therefore, in this paper, digital imaging correlation (DIC) technique had been applied to AFM cell image, contributing to tracking and strain analysis of single cell. DIC technique is one of the image processing methods frequently employed for strain measurement of biological tissues and soft materials [28, 29]. It tracks the movement of multiple grid points (which forms a selected area on the digital images of samples) by comparing images in different deformed states to a reference image via a certain mathematical algorithm. If the object sample deforms, relative displacements of the grid points will be calculated and thus deformation of objects (strain) can be estimated. Several tracking algorithms had been developed in recent years, such as cross-correlation [30], gradient descent search [31], snake method [32], sum of squared differences [33], and fast normalized cross-correlation (FNCC) [34] algorithms.

Among numerous single cell studies, cell mechanics is one of the prime ones, involving cellular processes (e.g. cell growth and division) and diseases (e.g. cancer study). Many fundamental aspects of cellular function, including shape, deformability, motility, division, and adhesion, are critically dependent on mechanical properties (e.g., stiffness, nonlinearity, anisotropy, and heterogeneity) of the cell. As the most dominant factors in mechanical engineering, elastic properties gain a lot of popularity from scientists and researchers. The appearance of AFM and its force-spectroscopy realize the feasibility of measurements on elastic properties of cells, which open a nanoscopic window on the cell surface. By using AFM force-spectroscopy, researchers are trying to find the evidence that the state of health or disease of a cell might be detectable from changes in cell mechanical properties [35, 36, 37, 38]. Inspired by difference of mechanical properties between healthy and unhealthy cells, some researchers also started to investigate how various drugs that disrupt or stabilize actin or microtubule networks affect the elasticity of cells [24], and to characterize the mechanisms by which stress reversibly softens actin networks and contributes to cell stiffness by using AFM [39].

AFM “understands” the surface through a tiny mechanical probe. It serves as soft nanoindenters allowing local elasticity measurements of small and inhomogeneous samples like cells or tissues. To calculate the stiffness from AFM testing data, two most common models are used: Hertz model and Oliver-Pharr model. In Hertzian model, it assumes no other interaction other than elasticity and

therefore no plastic deformation between sample and tip. Young's modulus will be calculated from a function of loading force and indentation depth [40]. On the other hand, Oliver-Pharr model assumes that any deformation occurring during unloading is totally due to elasticity. At this point, the relationship between tip and sample can be calculated with the modulus of elasticity [41].

This thesis comprises two independent studies performed in my Master's study: (i) developing a tracking and strain measurement tool for AFM images by using DIC technique; (ii) using AFM force-displacement microscopy to study mechanical properties of cells. Since AFM is the major experiment instrument throughout my research, detailed introductions and fundamentals are described at first in chapter 2. Then in chapter 3, the DIC algorithm of the first study is introduced before the DIC technique is applied to AFM images. The result showed the good performance of DIC as a basic cell tracker, which is more economical and practical than other conventional techniques. Chapter 4 stated the second study in regards to the mechanical properties of living and dead cells. The concept and assumptions of two indentation models (Hertzian and Oliver-Pharr) are presented. The young's modulus estimated by Hertzian model indicated that modulus in different part of cell varied along the cell; moreover, dead cells became stiffer than living cells. The results suggest potential of mechanical property as an index to show vitality of cells, thereby reflect physical situation of human.

Chapter 2
Methods

2.1 Introduction

Originated with the invention of the scanning tunneling microscope (STM) [42], scanning probe microscope (SPM) emerged as a conceptually new family member of microscopes. As one of the most successful derivatives of SPM, AFM can measure the physical, chemical, mechanical, electrical and the magnetic properties of a sample' surface, which are essential for various researches in basic sciences (i.e. physics, chemistry, and biology) and applied industry (i.e. mechanical and electrical engineering). To help readers have a better understanding of AFM and make this paper accessible to a broad range of investigators, this chapter focuses on fundamental knowledge of AFM operation including: AFM operation principle, performance range, cantilever selection, in-air imaging and in-liquid imaging, and limitations of AFM. The AFM setup used in our laboratory and described herein is XE-100 from Park System Corp (see Figure 1).

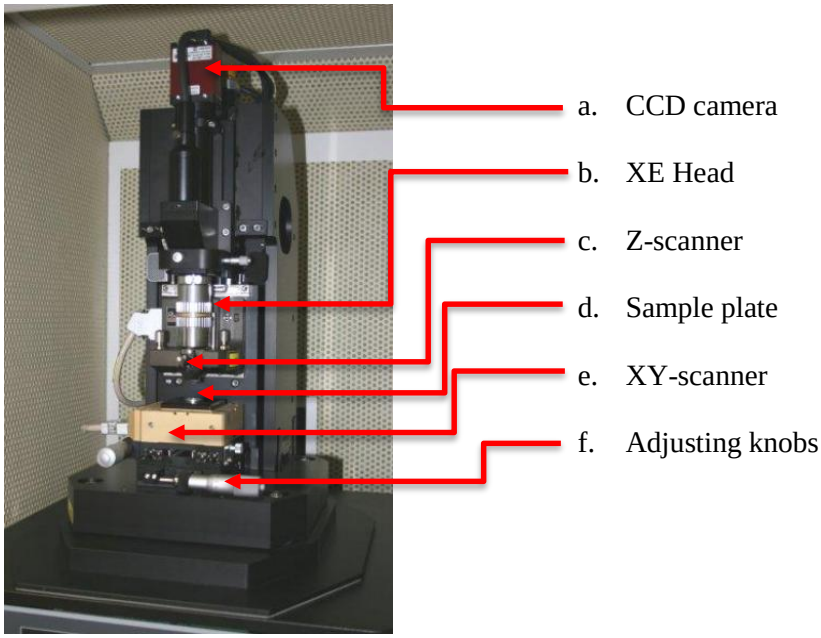

Figure 1: XE-100 AFM setup includes (a) direct on-axis high resolution (<1μm) digital CCD camera. (b) Optical Head to deliver optical beam. (c) Up to 25μm Flexure-guided force Z-scanner (high force multi-stack piezo). (d) Sample plate. (e) Up to 100 $\mu m \times 100 \mu m$ Flexure-based closed-loop XY-scanner. (f) Adjusting knobs for locate the sample plate.

2.1.1 Operation principle

Atomic force microscopy (AFM) has recently become one of the most popular instruments applied to the study of micro and nano cellular structures [10-12]. Modern AFM techniques allow solving many problems of cell biomechanics as a result of its high sensitivity (sub-piconewton), high spatial resolution (sub-nanometer), and the ability to be used for real-time measurements (topography and mechanical properties) in a physiologic aqueous cell culture environment.

In principle, the AFM can bring to mind the record player, but it is composed of a number of high-tech refinements that enable it to achieve atomic-scale resolution, such as a very sharp tip, a flexible cantilever, a sensitive deflection sensor, and high-resolution tip–sample positioning (scanner). A schematic diagram is shown in Figure 2.

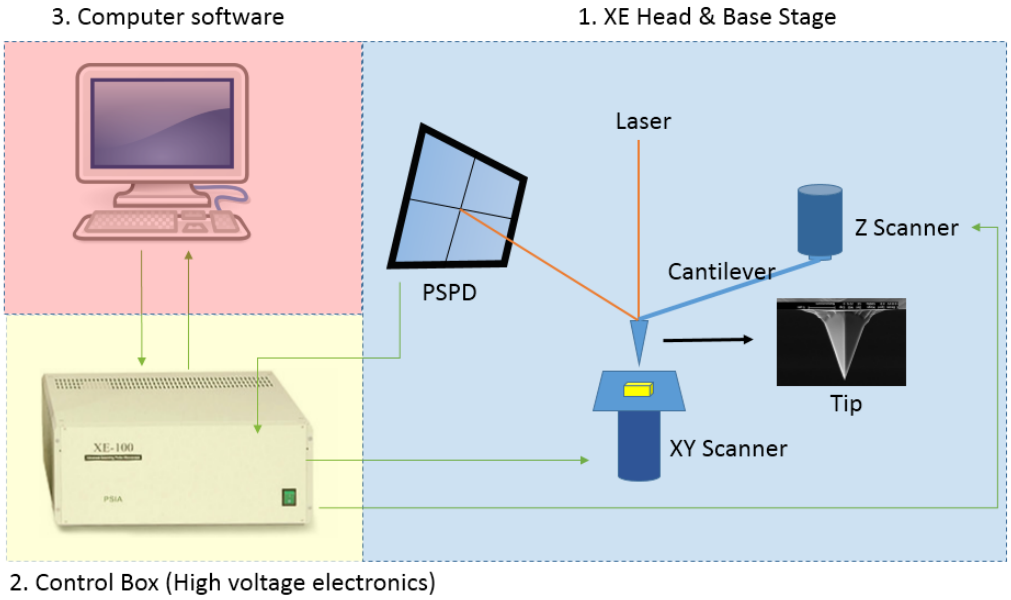

Figure 2: Schematic diagram of AFM's scanning.

In Figure 2, it could be found that the AFM setup consists of three main components. (i) The XE head and base stage: The AFM contains the tip holder, the laser, and the position-sensitive photodiode (PSPD). It also includes positioning mechanisms for focusing the laser beam on the back side of the cantilever and PSPD and small electronics for processing the signals coming from the PSPD. From this, the vertical and lateral deflections of the laser beam and total intensity are obtained. The XE head is placed over a base stage that holds the piezoelectric scanner that moves the sample and also a coarse, micrometer-ranges approaching mechanism, usually based on step motors. (ii) Control box: It

amplifies the signals coming from the digital signal processor (DSP) (XYZ low voltage) to drive the piezoelectric scanner with voltages of about 100 V (XYZ high voltage). The electronics also transfers the analog voltage signals from the PSPD to DSP. The high voltage (HV) electronics must be able to amplify small signals from the computer (of some volts) to hundreds of volts needed to move the piezoelectric tube over micrometer distances. It is therefore essential that this amplification does not introduce electrical noises that may affect the resolution of the AFM. (iii) Computer and software: The DSP performs all the signal processing and calculations involved in the real-time operation of the AFM. The DSP is mainly located in a board plugged in the computer. It contains the chips to perform the translation from digital to analog signals (digital to analog converters (DACs)), which are further managed by the HV electronics. Analog signals from the HV amplifier are converted to digital signals also at the DSP board using analog to digital converters (ADCs). Finally, all computer-based systems need software (XEP, data acquisition program) to run the setup. Raw images can later be processed with imaging-processing software (XEI).

A detailed detection and imaging methods are illustrated in Figure 3. As shown in Figure 3a, a laser beam is used to detect cantilever deflections towards or away from the surface. Via reflecting an incident beam off the flat top of the cantilever, any cantilever deflections will cause small changes in the direction of the reflected beam. The PSPD mentioned above can be used to track and record these changes. Thus, if an AFM TIP passes over a raised (or lowered) surface feature, the resulting and the subsequent cantilever deflection is observed by the PSPD (shown in Figure 3b).

As we all know, the basic function and initial intention of AFM is to get the topography of an object. The AFM scans sample surface by moving the mechanical tip over a region of interest and images its topography. The fluctuating features on the sample surface influence the deflection of the cantilever, which is monitored by the PSPD. For complicated surface with large fluctuations, it may damage the cantilever thereby break the probes. To improve this, our AFM applies a feedback loop to control the height of the tip above the surface (raising the height of Z Scanner) - thus maintaining a constant laser position (shown in Figure 3b & Figure 3c). From figure 3d, the topography is obtained but with the deflection adjusted back to the original position. Therefore, AFM can generate an accurate topographic map of the surface features.

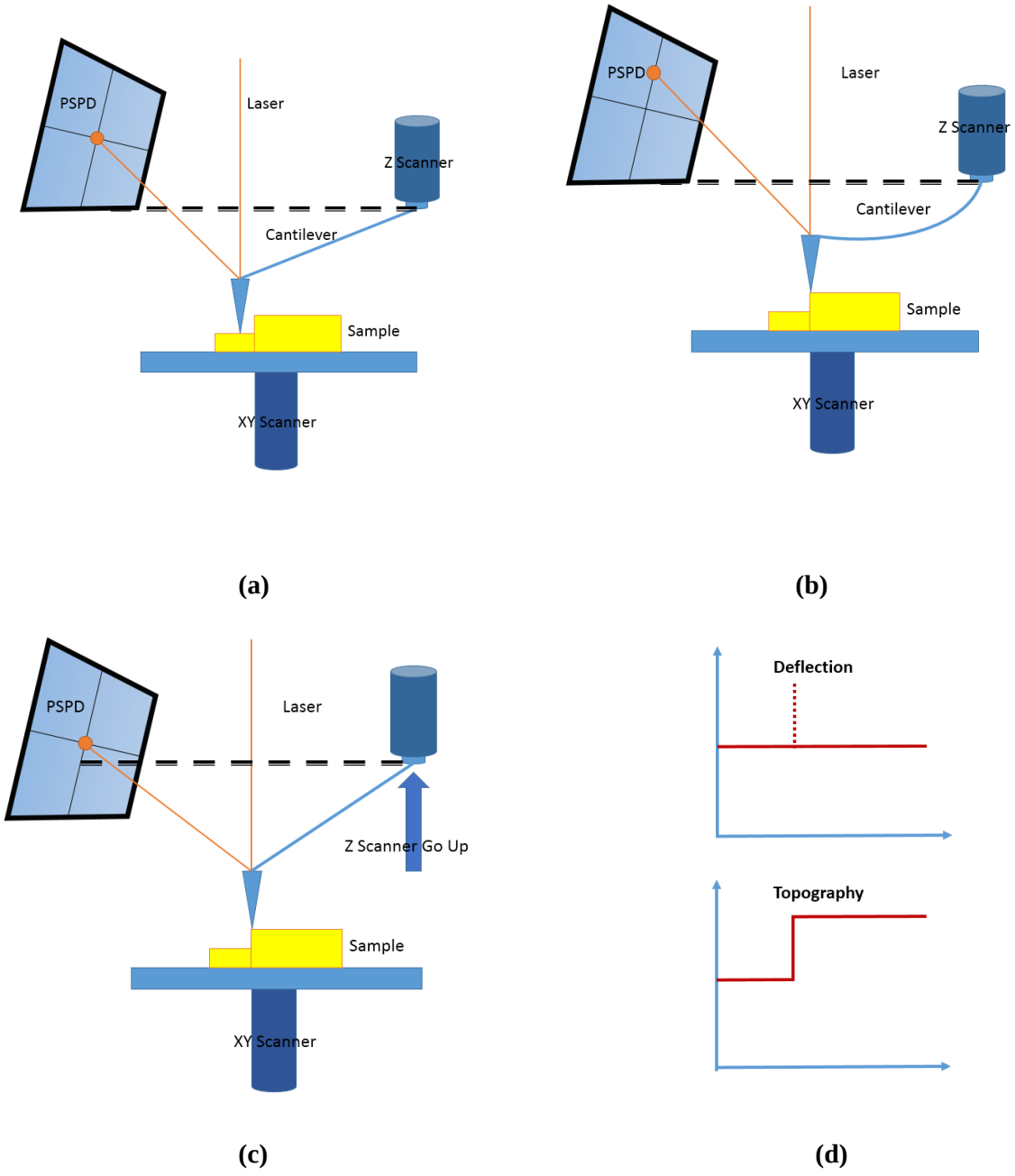

Figure 3: AFM detection and imaging methods: (a) Original position of Z scanner and PSPD. (b) Deflected cantilever due to surface topography. (c) Auto adjustment of Z scanner. (d) Deflection and topography trace

2.1.2 Performance range of AFM

AFM images are able to show significant information about surface features with unprecedented clarity. The AFM can examine any rigid surface as well as soft tissues either in air or with the specimen immersed in a liquid. Recently developed AFM can allow temperature control of the sample, can be equipped with a closed chamber for environmental control, and can be mounted on an inverted microscope for simultaneous imaging through advanced optical techniques [44]. The plane scanning size (size of AFM images) can be determined by the performance of horizontal piezoelectric positioners (XY scanner), which varies from 50 × 50 μm scale up to 100 × 100 μm. On the other hand, the vertical range of standard AFM head is from 8 to 10 μm [45] so that AFM may scan relatively rough surfaces. As to our AFM, the rated range of XY scanner is 100 × 100 μm, and maximum vertical range is 25μm, which is superior to most of AFMs in current market and provides precise measurements.

The samples which are under radius of 2.5 cm can be fitted directly on the sample plate without cutting. With stand-alone instruments, any area on flat or nearly flat specimens can be investigated. In addition to its outstanding resolution with respect to optical microscopes, the AFM has these key advantages with respect to electron microscopes. (i) Compared with the scanning electron microscope (SEM), the AFM provides better topographic contrast, as well as quantitative height information of sample surface. (ii) The sample of AFM need not be electrically conductive, no metallic coating of the sample is required. Hence, no dehydration of the sample is necessary as with SEM, and samples may be imaged in their hydrated state. This eliminates the shrinkage of biofilm associated with imaging using SEM, yielding a nondestructive technique. (iii) The resolution of AFM is higher than that of SEM, where hydrated images can also be obtained and extracellular polymeric substances may not be imaged. (iv) Compared with TEM which generates 2D profiles available from cross-sectioned samples, AFM can provide 3D images without expensive sample preparations and will yield far more complete information.

2.1.3 Cantilever selection

In general, the term “cantilever” includes the silicon chip, a cantilever hanging from the chip, and a tip hanging from the end of the cantilever. Figure 4a below shows the overall view and the name of each part of the cantilever used in the AFM; moreover, figure 4b is an SEM image to give reader a conceptual size of cantilever. The common materials of chip, cantilever, and tip are Silicon (Si) or Silicon Nitride (Si3N4), and are manufactured using micro-machining techniques. On the upper

surface of the cantilever (the opposite side of the tip), it is always coated very thinly with a metal such as gold (Au) or aluminum (Al) to enhance the high reflectivity. To adapt different experiment environment, cantilevers with different coating need to be considered.

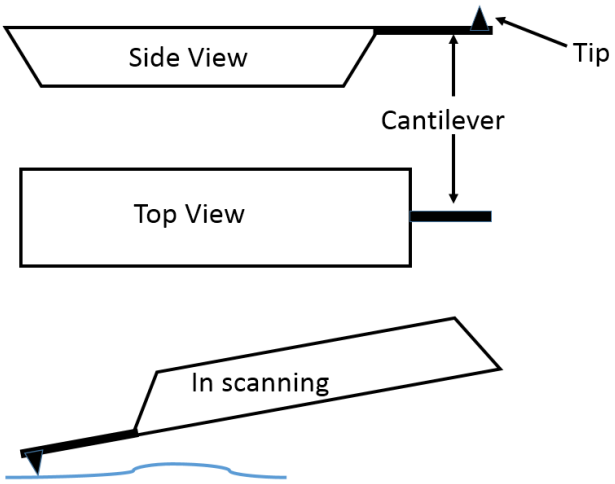

(a)

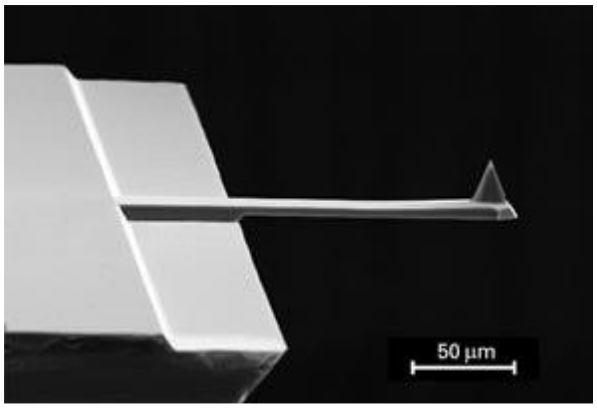

(b)

Figure 4: Cantilever chip (a) Overview and parts' name (b) SEM image of cantilever

There are many types of cantilevers varying in material, shape, softness (represented by the spring constant), resonant frequency, and Q-factor. The choice of a cantilever from among these is primarily determined by the type of AFM operation mode. Generally, there are two most common operation modes in current AFMs: contact mode and non-contact mode (details can be found in subheading 2.2).

In the contact mode, a "soft" cantilever, which has a small spring constant of about 0.01 N/m ~ 3N/m to respond sensitively to the tiny force between atoms is usually chosen. The probe tip used in the contact mode has a thickness of about 1μm to achieve a small spring constant. This is because a cantilever with a small spring constant makes a relatively large deflection to a small force, and can thus provide a very fine image of the surface structure.

On the other hand, in non-contact mode, a cantilever has a greater thickness, which is around 4μm, compared to contact mode. It has a spring constant of 40N/m which is very "stiff", and a relatively large resonant frequency. While contact mode detects the bending of a cantilever, the non-contact mode vibrates a cantilever at a high resonant frequency, and measures the force gradient by the amplitude and phase change due to the interaction between the probe and the sample, which yields the topography of the sample. When an AFM is operating in the atmosphere, or if the probe tip is situated on a moist or contaminated layer, it may often stick to the layer due to the surface tension of the tip. This happens more frequently if the spring constant of the cantilever is smaller. Because of the small spring constant, it is difficult to bring it back to the original position. Therefore we need a cantilever with a spring constant which can overcome the surface tension. The sharper the tip, the more stable operation can be expected because the surface area of the tip and the surface tension are reduced.

2.1.4 In-air imaging and in-liquid imaging

Samples to be imaged in atmospheric environment are often glued to a sample holder (e.g. petridish, ceramic or metal disk, and etc.). The metal disk can be inserted in the AFM, where it is held firmly by a small magnet. An essential point is that the sample has to be firmly adherent to the sample holder; otherwise, very poor imaging will be achieved. For this reason, one has to be careful in the choice of the glue or sticky tape: slow drying glue or thick sticky tape should be avoided. A drawback is that after use in the AFM, the sample is difficult to take off without damage.

For some other systems, samples can be accepted directly, securing them with a metal clip or springs. This method allows sample recovery without damage for further use in other experiments, but it can be less stable and needs special care for high-resolution work. Sometimes, because of the ease of use of the AFM, one forgets to be careful while handling the sample and either fingerprints or dust from a dirty environment contaminates the sample. It is best to keep a reserved area of the laboratory free from contaminants for the operations of sample and cantilever mounting.

One of the main reasons for the success of AFM in biomedical investigations is its ability to scan samples in physiological condition since most biological samples' morphological information can

only be obtained in liquid conditions [46, 47]. In-liquid imaging is not standard configuration for most of commercial AFMs. For our AFM, switching in-air imaging and in-liquid imaging can be realized by changing specific probehand. In order to do an AFM measurements in aqueous environment, a liquid probehand is required (as shown in Figure 5).

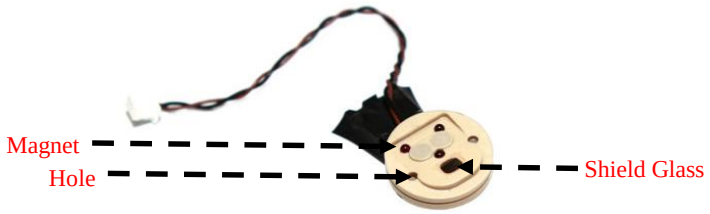

(a)

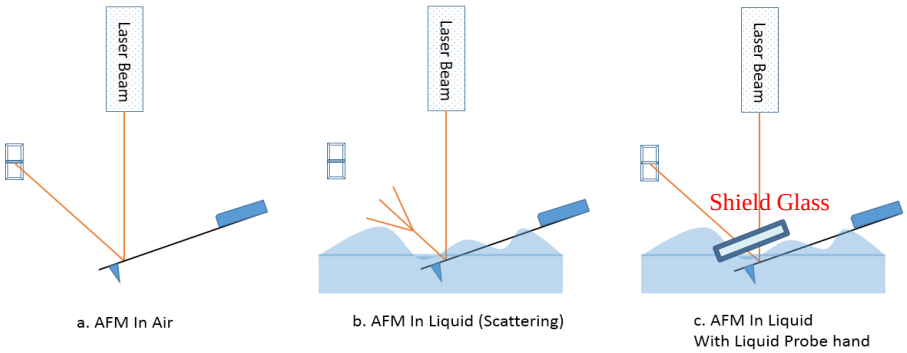

(b)

Figure 5: The liquid probe-hand

The feedback system of our AFM uses a super luminescent diode (SLD) beam (as shown in Figure 3a: laser beam) reflected from the cantilever to measure the surface morphology. However, the SLD beam can be scattered by an unstable liquid surface. To prevent this drawback, the liquid probehand with shield glass is applied to make the AFM images possible and reliable.

2.1.5 Limitations and problems

As mentioned above, the AFM can easily take a measurement of a conductor, a non-conductor, and even soft biological samples without delicate sample preparation (unlike SEM or TEM). Also, it is a powerful tool that can measure extremely small structures which other instruments have difficulties investigating. Despite its many advantages, the AFM does have some drawbacks as well, which have been listed as following:

(a) Low measurement speed: Since the tip has to mechanically follow a sample surface and proceeds a progressive scanning, the measurement speed of getting an AFM image is much slower than that of an optical microscope or an electron microscope. The higher resolution of AFM images is, the longer time it will take for AFM to scan.

(b) Inherent instrument errors: The scanners used in AFMs are piezoelectric ceramic tubes. Due to the non-linearity and hysteresis of piezoelectric materials, this may result in measurement errors.

(c) Limitation of tip scanning: Since the tip has a finite tiny size, it is very difficult and sometimes impossible to measure a narrow, deep indentation or a steep slope. The common height of an AFM tip is from 10-20μm. If the surface of sample has relatively large fluctuations with regard to height of tip, measurement errors can occur and low quality images will obtain.

(d) Tip cleaning and consuming: AFM tip is easily getting damaged and contaminated. Especially for biological experiments, due to viscosity of soft materials, AFM tip is always get contaminated or get adhered with tiny objects. These contaminations will directly affect the performance of AFM measurements and imaging. Though it sometimes can be removed by soaking tip into water and ethanol, most of them remain on tip and AFM users have to replace new tip to assure good experiment results.

2.2 AFM imaging modes

One can easily distinguish between two general imaging or operation modes of AFM depending on absence or presence of oscillating cantilever at the proximity of its resonant frequency. The first case is usually called contact mode, or DC mode, because it records the deflection of the cantilever while AFM probe physically contacts the sample surface and scans across; whereas, the second one is named Non-contact mode or AC mode (it takes a variety of names in different commercial AFMs). In this case, the feedback loop keeps at a constant value not for the deflection but the amplitude of the oscillation of the cantilever while scanning the surface. From a physical point of view, one can also

make a distinction between these two modes depending on the sign of the forces involved in the interaction between tip and sample, that is, by whether the forces there are attractive or repulsive [48]. In Figure 6, an idealized illustration of the forces between tip and sample is shown, shaded parts are the areas where those two imaging modes operate. In the following we briefly describe the contact and non-contact modes and their operating principles.

2.2.1 Contact mode

The AFM is an instrument that is used to study the surface structure of a sample by measuring the force between atoms. In contact mode, the cantilever is in contact with surface while scanning. Due to this, strong repulsive forces cause the cantilever to deflect as it passes over topographical features.

As mentioned above (subheading 2.1.3), there is a very sharp cone-shaped or pyramid-shaped tip at the free end of the cantilever. When the distance between the atoms at this tip and the atoms on the surface of the sample becomes shorter, these two sets of atoms will interact with each other. As shown in Figure 6, when the distance between the tip and the surface atoms becomes very short, the interaction force is repulsive due to electrostatic repulsion, and when the distance gets relatively longer, the attractive force becomes dominant due to the long-range Van der Waals forces.

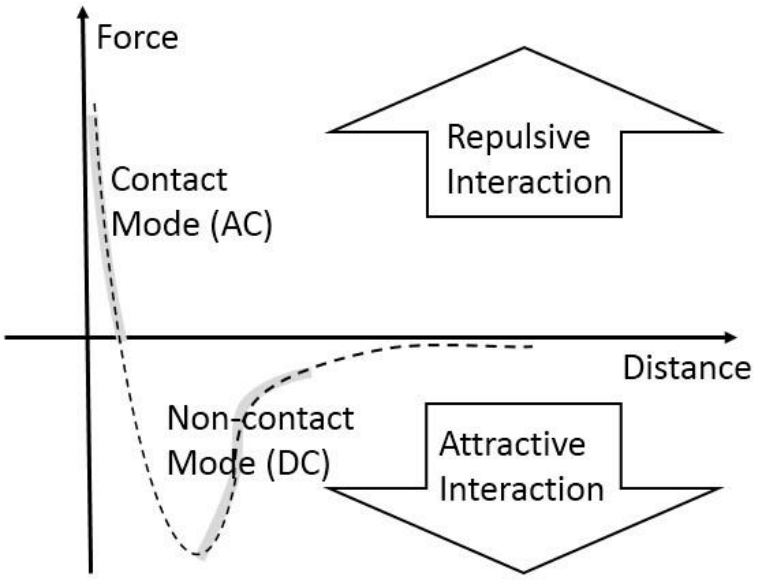

Figure 6: Relation between the force and the distance between atoms

This interatomic force between atoms can bend or deflect the cantilever, and the amount of the deflection will cause a change in the reflection angle of the laser beam that is bounced off the upper

surface of the cantilever. Then, the change in laser path will in turn be detected by the PSPD, thus enabling the computer to generate a map of the surface topography

In contact mode, AFM probe makes "soft contact" with the sample surface, and the sample's topography is then conducted by utilizing the repulsive force that is exerted vertically between the sample and the probe tip. The interatomic repulsive force in contact mode is merely 1~10 nN, the spring constant of the cantilever is also sufficiently small (less than 1 N/m), thus allowing the cantilever to react very sensitively to very minute forces. The AFM is able to detect even the slightest amount of a cantilever's deflection as it moves across a sample surface. Therefore, when the cantilever scans a convex area of a sample, it will deflect upward, and when it scans a concave area, it will deflect downward. This probe deflection will be used as a feedback loop input that is sent to an actuator (z-piezo). In order to produce an image of the surface topography, the z-piezo will maintain the same cantilever deflection by keeping a constant distance between the probe and the sample.

2.2.2 Non-contact mode

Two major forces are involved in AFM mechanisms: the static electric repulsive force and attractive force. Switch of operation modes relying on changing of the distance between probe tip and the sample surface. As shown in Figure 6, when the distance between the probe tip and the sample atoms is relatively large, the attractive force becomes dominant. Ion cores become electric dipoles due to the valence electrons in the other atoms, and the force induced by the dipole-dipole interaction is the van der Waals Force. In non-contact mode, AFM measures surface topography by utilizing this attractive atomic force in the relatively larger distance between the tip and a sample surface.

Figure 7 compares the movement of the probe tip relative to the sample surface for images being acquired between in contact mode and in non-contact mode. Under contact mode, AFM uses the "physical contact" between the probe tip and the sample surface, whereas noncontact mode does not require this "contact" with the sample. In non-contact mode, the force between the tip and the sample is very weak so that there is no unexpected deformation in the sample during the measurement. Therefore, non-contact mode is very adaptive when a biological sample or other very soft sample is being measured; the tip will also have an extended lifetime because it is not abraded during the scanning process. On the other hand, the force between the tip and the sample in the non-contact regime is very low, and it is not possible to measure the deflection of the cantilever directly. So, non-contact AFM detects the changes in the phase or the vibration amplitude of the cantilever that are

induced by the attractive force between the probe tip and the sample while the cantilever is mechanically oscillated near its resonant frequency.

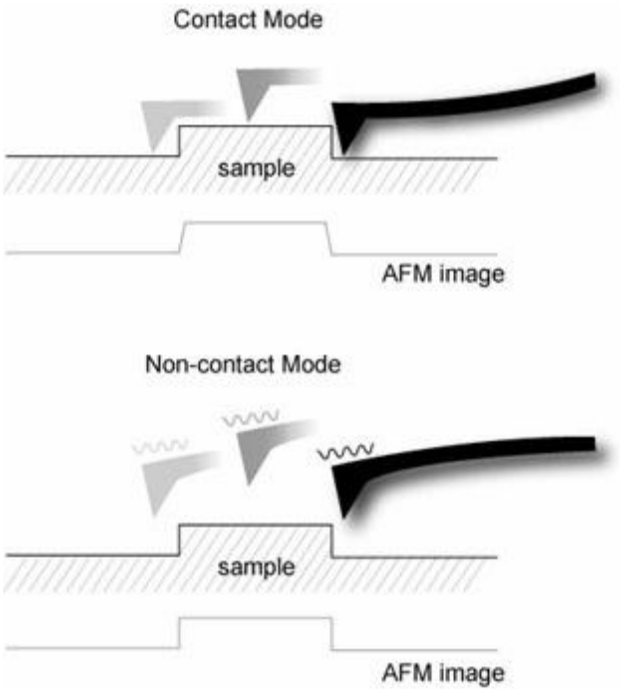

Figure 7: Concept diagram of Contact mode and Non-Contact mode [43]

A cantilever used in non-contact mode typically has a resonant frequency between 100 kHz and 400 kHz with vibration amplitude of a few nanometers. Because of the attractive force between the probe tip and the surface atoms, the cantilever vibration at its resonant frequency near the sample surface experiences a shift in spring constant from its intrinsic spring constant (k_o). This is called the effective spring constant (k_{eff}), and the following equation holds:

$$k_{eff} = k_o - F' \tag{2-1}$$

When the attractive force is applied, k_{eff} becomes smaller than k_o since the force gradient F' ($\partial F/\partial$) is positive. Accordingly, the stronger the interaction between the surface and the tip (in other words, the closer the tip is brought to the surface), the smaller the effective spring constant becomes. This alternating current method (AC detection) makes more sensitive responds to the force gradient as opposed to the force itself. Thus, it is also applied in such techniques as MFM (Magnetic Force Microscopy) and DFM (Dynamic Force Microscopy).

A bimorph is used to mechanically vibrate the cantilever. When the bimorph's drive frequency reaches the vicinity of the cantilever's natural/intrinsic vibration frequency (f_o), resonance will take place, and the vibration that is transferred to the cantilever becomes very large. This intrinsic frequency can be detected by measuring and recording the amplitude of the cantilever vibration while scanning the drive frequency of the voltage being applied to the bimorph. Figure 8 displays the relationship between the cantilever's amplitude and the vibration frequency. From this output, we can determine the cantilever's intrinsic frequency.

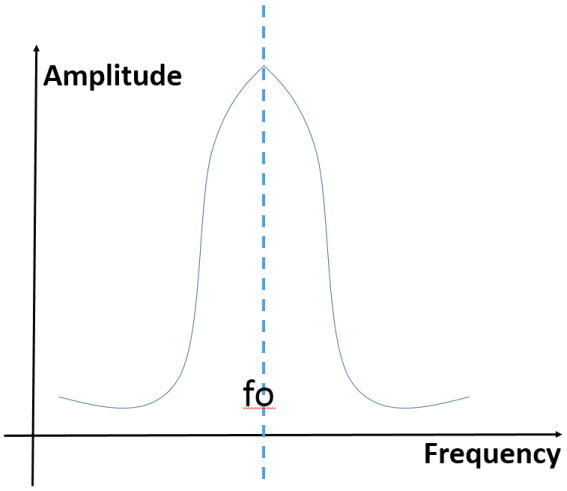

Figure 8: Resonant Frequency

On the other hand, the spring constant affects the resonant frequency (f_o) of the cantilever, and the relation between the spring constant (k_o) and the resonant frequency (f_o) is as in Equation (2-2).

$$f_o = \sqrt{\frac{k_o}{m}} \tag{2-2}$$

In Equation (2-1), since k_{eff} becomes smaller than k_o due to the attractive force, and f_{eff} becomes smaller than f_o as well (as shown in Figure 9(a)). If the cantilever vibrates at the frequency f_1 (a little bit larger than f_o), where a steep slope is observed in the graph representing free space frequency vs. amplitude, the amplitude change (ΔA) at f_1 becomes very large even with a small change of intrinsic frequency caused by atomic attractions. Therefore, the amplitude change measured in f_1 reflects the distance change (Δd) between the probe tip and the surface atoms. If the change in the intrinsic frequency resulting from the interaction between the surface atoms and the probe or the amplitude

change (ΔA) at a given frequency (f_1) can be measured, the non-contact mode feedback loop will then compensate for the distance change between the tip and the sample surface as shown in Figure 9(b). By maintaining constant cantilever's amplitude (A_0) and distance (d_0), non-contact mode can measure the topography of the sample surface by using the feedback mechanism to control the Z scanner movement following the measurement of the force gradient represented in Equation (2-1).

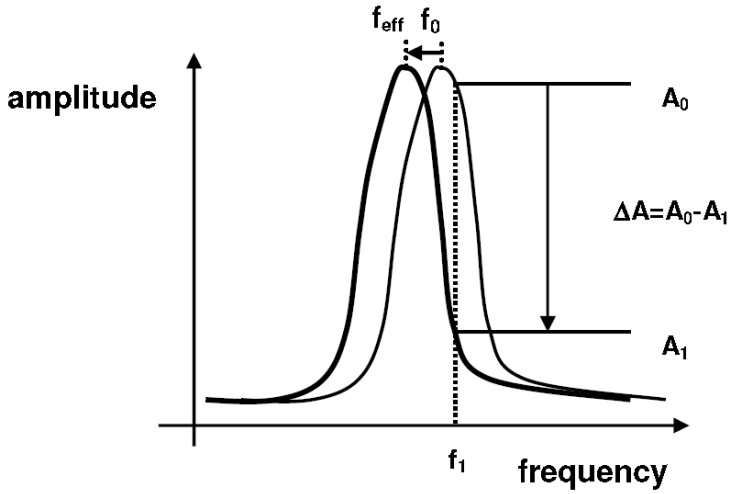

(a)

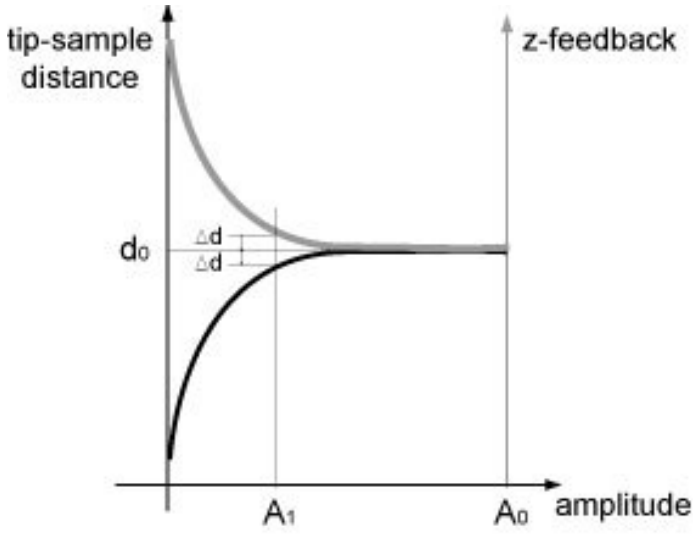

(b)

Figure 9: Noncontact mode frequency setup (a) Resonant frequency shift (b) Amplitude vs. Z-feedback [43]

2.3 Measurements of force & mechanical properties by using AFM

2.3.1 Force-distance spectroscopy

In force-distance spectroscopy, the vertical force that the tip applies to the surface can be measured by a force vs. distance curve while a contact-AFM image is being taken. This technique can also be used to analyze surface contaminants' viscosity, lubrication thickness, and local variations in the elastic properties of the surface [43].

As described in previous sections, the force that tip applies to sample surface can be measured by the deflection of the cantilever; in addition, the distance between tip and sample surface can be obtained by measuring the extension of the piezoelectric scanner. Strictly speaking, a force vs. distance curve is a plot of the deflection of the cantilever versus the extension of the piezoelectric scanner. Local variations in the form of the force-displacement curve indicate changes in the local elastic properties.

In the laboratory, force-distance curves are quite specific to the given system under study. Contaminants and lubricants are the most common factors that affect the accuracy of measurement, as the thin layer of water is often present when operating an AFM in air. To have a better understanding of these problems, a detailed discussion of each condition is presented below.

In Figure 10, a gross simplification is represented, where shapes, sizes, and distances should not be taken literally. With this in mind, consider the simplest case of AFM in vacuum as shown in Figure 10(a). At the left side of the curve, the scanner is fully retracted and the cantilever is undeflected since the tip is not touching the sample. As the scanner extends, the cantilever remains undeflected until it gets close enough to the sample surface for the tip to experience the attractive van der Waals force. The tip snaps into surface at point a as shown in Figure 10(a). At this point, the cantilever suddenly bends slightly towards the surface. As the scanner continues to extend, the cantilever deflects away from the surface, approximately linearly in region b of Figure 10(a). After full extension, at the extreme right of the plot, the scanner begins to retract. The cantilever deflection retraces the same curve as the scanner pulls the tip away from the surface.

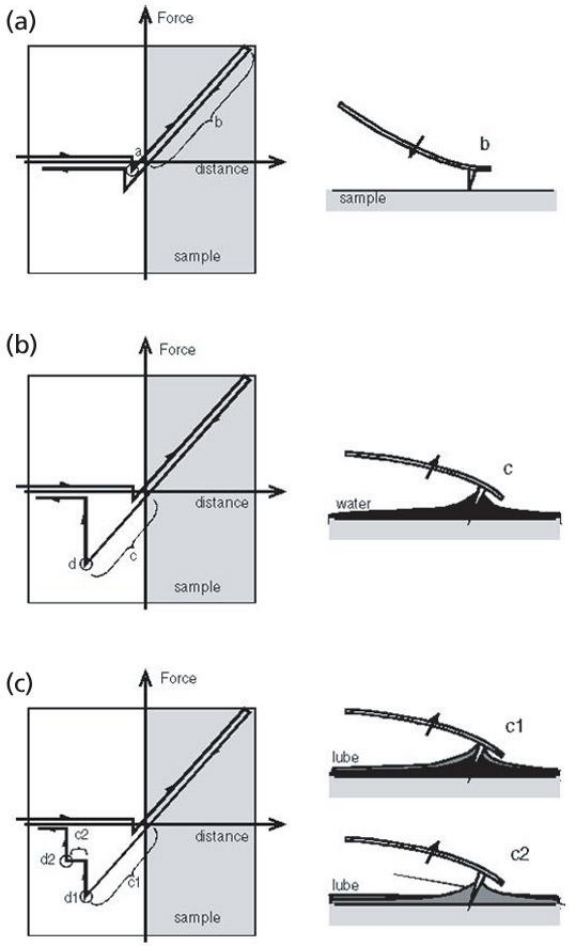

Figure 10: Force vs. displacement curves (a) Force vs. distance curves in vacuum, (b) force vs. distance curves in air (c) force vs. distance curves in air with a contamination layer. [43]

In air, the retracting curve is often different as a monolayer or a few monolayers of water are usually present on many sample surfaces (on the right side of Figure 10(b)). This water layer exerts a capillary force that is very strong and attractive. As the scanner pulls away from the surface, the water holds the tip in contact with the surface, bending the cantilever strongly towards the surface in region c (on the left side of Figure 10(b)). At some point, depending upon the thickness of the water layer, the scanner retracts enough that the tip springs free at point d. This is known as the snap-back point. As the scanner continues to retract beyond the snap-back point, the cantilever remains undeflected as the scanner moves it away from the surface in free space. If a lubrication layer is present along with the water layer, multiple snap-back points can occur, as shown in Figure 10(c). The positions and

amplitudes of the snap-back points depend upon the viscosity and thickness of the layers present on the surface.

Along the linear portion of the force vs. distance curves (in regions B or C of Figure 11), operations can be processed under contact mode. Operations in region C might be used for soft samples to minimize the force interaction between the tip and the sample. Operating with the cantilever bent towards the surface is inherently a less stable situation, and maximum scan speeds have to be sacrificed. One should note that operations in region C is under contact mode, since the tip is still contacting with the sample surface. Non-contact mode should be operated to the left of point a on the force-displacement curve, where just right above the snap-back point because of the attractive van der Waals force.

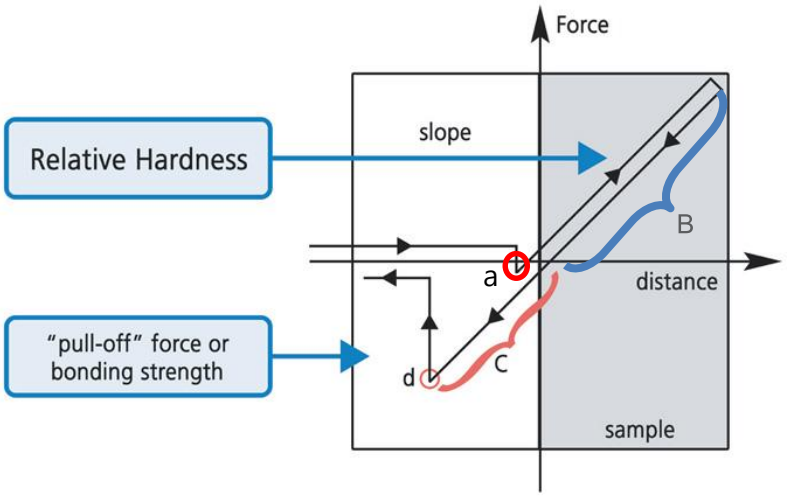

Figure 11: The various elastic properties that can be measured from Force vs. Distance curves.

In the linear region of the force-displacement curves, the slope can be used for calculating elastic modulus of the system. When the cantilever is much softer than the sample surface, as is the case for non-destructive imaging, the slope of the curve mostly reflects the spring constant of the cantilever. Nevertheless, when the cantilever is much stiffer than the sample surface, the slope of the force-displacement curve allows investigation of the elastic properties of the sample as shown in Figure 11.

2.3.2 Nano-indentation

Hardness measures the resistance of a sample to material deformation due to a constant compression load from a sharp object. Nanoindentation is one of the modes provided by XE-100 AFM to

determine the hardness of sample surface in a specific local region. Its application includes hard coating (titanium nitride coating), microelectronics (reliability of metal bond), thin film technology (adhesion failure), and polymers [43]. An indent is made by a sharp tip pressing down on a sample as shown in Figure 12. The depth and area of the indent are correlated with the hardness. Other properties such as elasticity, adhesion, creep, and tribology can be calculated from the indentation data as well.

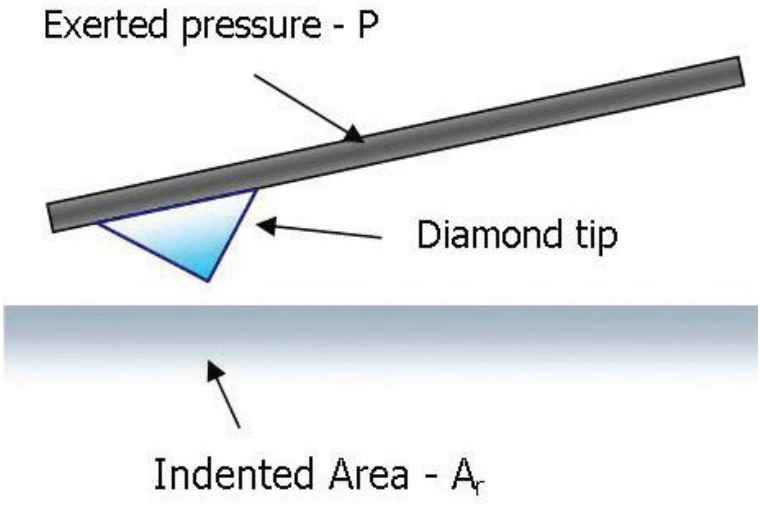

Figure 12: Nano-indenter diagram: AFM probes with diamond coating

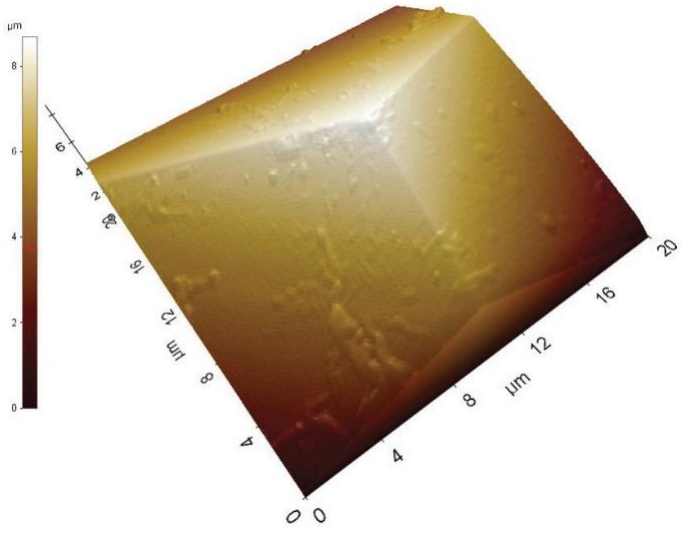

Figure 13: The image of Berkovich indenter (imaged under non-contact mode). [43]

The physical indentation itself is not hard for AFM system; however, the analysis of indentation result is highly demanded. The important factors involved in analyzing results are the force calibration and the indentation depth, or so-called displacement. The force constant of a cantilever, the shape of the tip (e.g. conical, four-sided pyramid), and other properties such as tip dimension determine the total force exerted onto a sample. Therefore, the accurate imaging of the shape and geometries of the indenter can result in a huge advantage when it comes to a reliable force calibration. To enable a precise and accurate imaging of indentation tip, AFM is the best method capable of exact geometry determination of such tiny areas. An AFM image of the typical nano-indenter (Berkovich indenter) is shown in Figure 13. The advantage of Berkovich indenter is that it can provide a quantitative force measurement without damaging the indenter tip.

Instead of applying Berkovich indenter, four-sided pyramid indenters are chosen for our measurements, which are more effective in high resolution and sensitivity indentation; however, it is very difficult to precisely measure the shape of sharp tip features because any physical contact or applied force (i.e. contact AFM and non-contact AFM) will break the tip. Instead of taking AFM images, we selected and took the SEM images. Figure 14 shows those SEM images, which were taken in Materials Lab, University of Waterloo, with a 3D sketch attached. All dimensions and angles were manually measured and calculated.

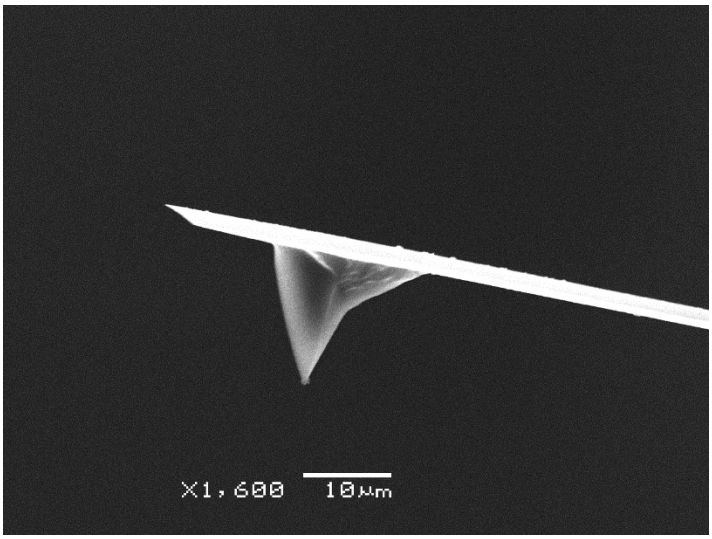

(a)

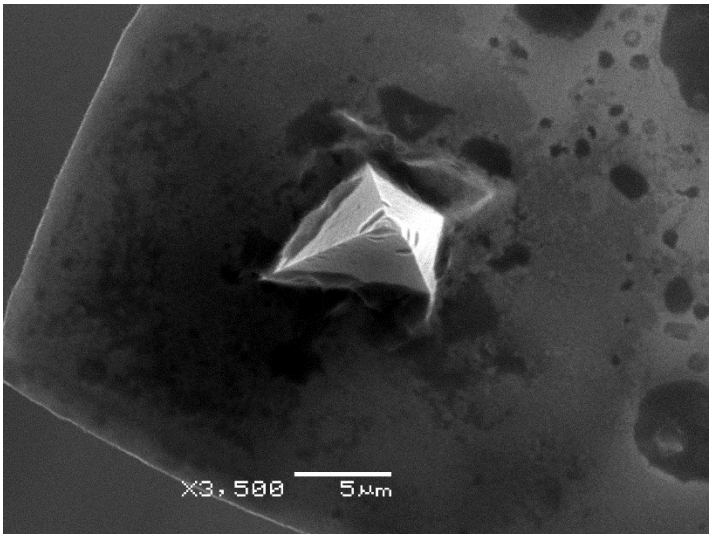

(b)

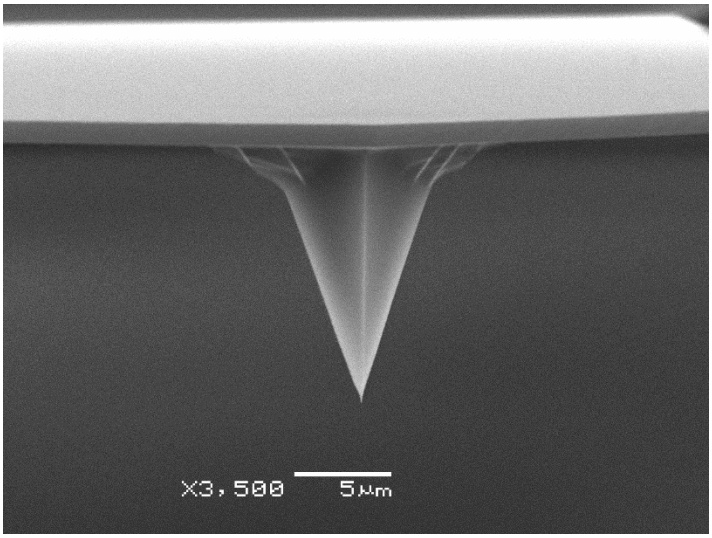

(c)

Figure 14: SEM images of AFM cantilevers (a) side view (b) top view (c) front view

The indenter is mounted on the beam such that one sharp edge is parallel to the long axis of the beam. Indenter stresses the surface of a sample at a specified force for about 1-2 seconds. Being similar to force-displacement spectroscopy, a load and indentation depth curve is recorded during the indentation process (as shown in Figure 15). These curves can be used to extract mechanical properties of the material such as young's modulus and hardness [49].

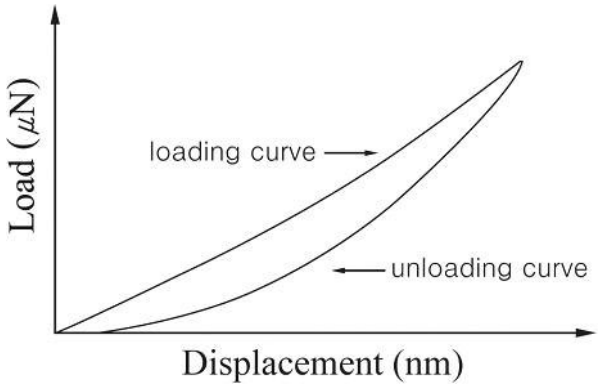

Figure 15: A loading and unloading displacement curves during nanoindentation.

Hardness is calculated by dividing the loading force by the projected residual area of the indentation. Besides hardness, the Young's modulus of elasticity can be obtained from the slope of the unloading curve. A typical loading and unloading displacement curves during a nanoindentation cycle are depicted in Figure 15. The results of young's modulus or hardness can be directly obtained by XEI (XE-100 AFM imaging processing software).

One should also note that the hysteresis indicates that the deformation is not fully elastic but partially inelastic. For purely elastic materials the loading and unloading curves would be closely identical. In our AFM, Nanoindentation is primarily used for determination of elasticity and viscoelasticity.

Chapter 3
Development of DIC applications applied on AFM images

3.1 Introduction

Digital image cross-correlation (DIC) is an innovative non-contact optical method which applies tracking & image recognition techniques for accurate 2D measurements of changes in digital images. This technique is often used to measure deformation, strain and displacement by tracking multiple points on images of an object or certain material. For those materials which does not have obvious surface features, they are usually decorated with speckled patterns; the tracking is achieved by comparing the patterns in the digital images taken before and after deformation. As a non-contact measurement technique, DIC gains a lot of popularity in micro- and nano-scale mechanical testing applications as a result of its relative ease of implementation and use [40]. For instance, some researchers applied DIC method to study fracture and fatigue behaviors of material [50, 51]. Not only solid materials, but also it extends to applications in biomechanics. Thompson et al. employed DIC technique to investigate the local distribution of mechanical strain within regenerating soft tissue sections [52].

This chapter mainly deals with development of DIC codes written in Matlab and their applications in tracking cells. From observing displacements of grid points, one could have some basic understanding of how cells migrate and deform. Specifically in subheading 3.2, the theoretical background on cross-correlation and supplementary algorithms (sub-pixel algorithm and data smoothing algorithm) to enhance the accuracy of DIC performance are discussed rigorously. In subheading 3.3, formation of AFM images is introduced as well as how DIC technique is applied to AFM images. Optimization of DIC is also fulfilled with respect to referencing method in this section. In subheading 3.4, application of DIC on AFM images can be divided into two steps: (i) applying DIC technique on AFM images of ceramic surface and fixed cells (ii) applying DIC technique on AFM images of live cells. The first step was to test the feasibility of DIC techniques on AFM images. Then the next step was to apply DIC techniques on images of live cells to observe cell migrations, which validates the possible application of DIC to track live cells and enables further studies on cell migration.

3.2 Theoretical background

3.2.1 Fundamental of cross-correlation

3.2.1.1 Basic concept of cross-correlation

Cross-correlation is a method to judge the similarity of two sets of signals or data that are acquired with a time-lag. This is also known as a sliding dot product or sliding inner-product. In this paper, we emphasize on its application in pattern recognition.

For continuous functions, f and g, the cross-correlation is defined as:

$$(f \cdot g)(t) \equiv \int_{-\infty}^{+\infty} \overline{f(\tau)} g(t+\tau) d\tau \tag{3-1}$$

where $\overline{f}$ denotes the complex conjugate of f and t is the degree of lagging. Similarly, for discrete functions, with the integer lagging n, the cross-correlation is defined as:

$$(f \cdot g)(n) \equiv \sum_{m=-\infty}^{+\infty} \overline{f(m)} g(n+m) \tag{3-2}$$

The cross-correlation value indicates level of similarity; therefore, n yielding the highest value can be regarded as the actual lagging between two functions assuming that they have the same form. The concept of the cross-correlation can be understood by considering two real valued functions f and g differing only by an unknown shift along the x-axis. The formula essentially slides the function g along the x-axis, calculating the integral (or summation) of product at each point. When the functions match, the value of $(f \cdot g)$ is maximized. This is because when peaks (positive or negative areas) are aligned, they make a large contribution to integral.

3.2.1.2 Discrete Fourier transform (DFT)

The discrete Fourier transform (DFT) is one type of discrete transform. It transforms one function into another, which is called the frequency domain representation. It is defined as:

$$F\{x\}_k = X_k = \sum_{n=0}^{N-1} x_n e^{-\frac{2\pi i}{N} kn} \qquad k = 0,\ldots, N-1 \tag{3-3}$$

The inverse discrete Fourier transform (IDFT) can be done by following equation

$$F^{-1}\{X\}_n = x_n = \frac{1}{N}\sum_{k=0}^{N-1} X_k e^{\frac{2\pi i}{N}kn} \quad n = 0,\ldots,N-1 \tag{3-4}$$

3.2.1.3 Convolution, and Convolution theorem

In mathematics convolution is a mathematical operation of two functions f and g producing a third function that is typically considered as modified version of one of the original functions by the other function called weighting function. It is defined as the integral of the product of the two function after one is reversed and shifted by t.

$$(f * g)(t) \equiv \int_{-\infty}^{+\infty} f(\tau)g(t-\tau)d\tau \tag{3-5}$$

It may be described as the average of the function f at the moment t weighted by the reverse of the function g. Similarly for discrete functions, it is defined as:

$$(f * g)(n) \equiv \sum_{m=-\infty}^{+\infty} f(m)g(n-m) \tag{3-6}$$

Assuming function f and g are periodic with period N, and if we add a constraint to the interval [0, N-1], the equation can be modified as:

$$(f * g)(n) \equiv \sum_{m=0}^{N-1} f(m)g(n-m) \tag{3-7}$$

Now one can apply the convolution theorem to equation 3-7. The convolution theorem states that the Fourier transform of a convolution is the pointwise product of Fourier transforms. In this case it can be expressed as:

$$F\{\sum_{m=0}^{N-1} x(m)y(n-m)\}_k = F\{x\}_k \cdot F\{y\}_k \quad k = 0,\ldots,N-1 \tag{3-8}$$

Proof.

$$
\begin{aligned}
F^{-1}\{F\{x\}\cdot F\{y\}\}_n &= \frac{1}{N}\sum_{k=0}^{N-1} X_k \cdot Y_k \cdot e^{\frac{2\pi i}{N}kn} \\
&= \frac{1}{N}\sum_{k=0}^{N-1}\Big(\sum_{m=0}^{N-1} x_m e^{-\frac{2\pi i}{N}km}\Big)\cdot\Big(\sum_{l=0}^{N-1} y_l e^{-\frac{2\pi i}{N}kl}\Big)\cdot e^{\frac{2\pi i}{N}kn} \\
&= \sum_{m=0}^{N-1} x_m \frac{1}{N}\sum_{k=0}^{N-1}\Big(\sum_{l=0}^{N-1} y_l e^{-\frac{2\pi i}{N}kl}\Big)\cdot e^{\frac{2\pi i}{N}k(n-m)} \\
&= \sum_{m=0}^{N-1} x_m \frac{1}{N}\sum_{k=0}^{N-1} Y_k \cdot e^{\frac{2\pi i}{N}k(n-m)} \\
&= \sum_{m=0}^{N-1} x_m y_{n-m} = \sum_{m=0}^{\mathrm{N\text{-}1}} x(m)y(n-m) \qquad n = 0,\ldots,N-1
\end{aligned}
$$

Note that x and y were used here instead of f and g to avoid any confusion in using F for the symbol of Fourier transform operator and Fourier transform of the function f.

3.2.1.4 Similarity between convolution and cross-correlation

According to the property of cross-correlation, one can find that cross-correlation of function $f(t)$ and $g(t)$ is equivalent to the convolution of $f(t)$ and $g(-t)$. Therefore, it can be found that:

$$
F\{\sum_{m=0}^{\mathrm{N\text{-}1}} x(m)y(n+m)\}_k = \overline{F\{x\}_k}\cdot F\{y\}_k \qquad k = 0,\ldots,N-1 \tag{3-9}
$$

Using this relationship, the computational load significantly can be reduced by Fast Fourier Transforms (FFT) which is referred to efficient algorithm to compute the discrete Fourier transform and the inverse process. Since there are too many distinct FFT algorithm, they are not discussed here.

3.2.1.5 Normalized cross-correlation and fast normalized cross-correlation

The cross-correlation equation can be modified by subtracting the average value from each function before performing cross-correlation. For discrete real functions f of size N and g of size N or even larger, it can be expressed as:

$$
\sum_{m=0}^{\mathrm{N\text{-}1}} (f(m) - f_{ave})(g(n+m) - g_{ave}) \tag{3-10}
$$

Digital image is a numeric representation of a two-dimensional image, which contains a fixed number of rows and columns of pixels (matrix form). The higher the number of rows and columns is, the higher the resolution of image is. One of the most common digital images is grayscale image in which the value of each pixel is a single sample to carry intensity information. It is also known as black-and-white images varying from black at the weakest intensity to white at the strongest. For instance, for an 8-bit grey image each pixel is expressed in terms of numeric between 0 and 255 (i.e. color depth). In other words, the tone gradually changes from black to white as the value increases from 0 to 255. When the functions f and g are cross correlated by Eq. (3-2), the contributions from the pixels with a high grey value are maximized; however, those from the pixels with low grey values are ignored. Eq. (3-10) makes the minimum values negative peaks and take full advantage of the contribution of them while keeping the maximum values as positive peak and their contribution. It also produces negative contribution when two opposite values overlap. Therefore, the resulting correlation values have a better contrast in expressing similarity.

The accuracy of cross-correlation can be further improved by normalizing Eq. (3-10) as:

$$\frac{\sum_{m=0}^{N-1}(f(m)-f_{ave})(g(n+m)-g_{ave,n})}{[\{\sum_{m=0}^{N-1}(f(m)-f_{ave})^2\}\{\sum_{m=0}^{N-1}(g(n+m)-g_{ave,n})^2\}]^{0.5}} \tag{3-11}$$

This is called the normalized cross correlation (NCC) and yields a value of 1 when two data sets are exactly matched and close to 0 when no match is made. Note that in real application function g is not periodic and its size is usually bigger than the size of function f. Due to the non-periodicity of g and size differences between f and g, computational problem arises. Looking into the numerator which is the same as Eq. (3-10) and the second half of the denominator of Eq. (3-11), respectively, we have,

$$\begin{aligned}\sum_{m=0}^{N-1}(f(m)-f_{ave})(g(n+m)-g_{ave,n}) &= \sum_{m=0}^{N-1} f(m)g(n+m) - Ng_{ave,n}f_{ave} \\ &= \sum_{m=0}^{N-1} f(m)g(n+m) - f_{ave}\sum_{m=0}^{N-1} g(n+m)\end{aligned} \tag{3-12}$$

$$\sum_{m=0}^{N-1}(g(n+m)-g_{ave,n})^2=\sum_{m=0}^{N-1}\{g(n+m)^2-2g(n+m)g_{ave,n}+{g_{ave,n}}^2\}$$
$$=\sum_{m=0}^{N-1}\{g(n+m)^2\}-g_{ave,n}\sum_{m=0}^{N-1}g(n+m) \tag{3-13}$$
$$=\sum_{m=0}^{N-1}\{g(n+m)^2\}-\frac{1}{N}\{\sum_{m=0}^{N-1}g(n+m)\}^2$$

When the sizes of f and g are different, we cannot apply convolution theorem and FFT to the first term in Eq. (3-12), $\sum_{m=0}^{N-1}f(m)g(n+m)$ resulting in huge computation load. Nevertheless, this can be easily solved by padding zeros to f and increasing its size up to that of g. However, the terms, $\sum_{m=0}^{N-1}g(n+m)$ and $\sum_{m=0}^{N-1}\{g(n+m)^2\}$ are still problematic regarding the computational load as the number of n increases since one has to calculate the local sum of g and g^2 for each n. This problem can be relieved by adopting the sum table suggested by Lewis [35]. Sum table is the pre-calculated look-up table over the whole region of function g, and is referred to each time local sum is calculated. In this case we can make two sum tables:

$$S_1(l)=\sum_{k=0}^{l}g(k) \qquad l=0,1,2...,L-1 \tag{3-14}$$

$$S_2(l)=\sum_{k=0}^{l}\{g(k)\}^2 \qquad l=0,1,2...,L-1 \tag{3-15}$$

where L is the size of function g. Using these pre-calculated sums, S_1 and S_2 along the l, One can determine the local sums of g and g^2 following scheme:

$$\sum_{m=0}^{N-1}g(n+m)=\sum_{k=0}^{n+N-1}g(k)-\sum_{k=0}^{n-1}g(k)=S_1(n+N-1)-S_1(n-1) \tag{3-16}$$

$$\sum_{m=0}^{N-1}\{g(n+m)\}^2=\sum_{k=0}^{n+N-1}\{g(k)\}^2-\sum_{k=0}^{n-1}\{g(k)\}^2=S_2(n+N-1)-S_2(n-1) \tag{3-17}$$

NCC applying with the sum-table method in computation is called Fast Normalized Cross Correlation (FNCC). In FNCC, it requires large computational load to make sum-table, but once sum table is completed, it needs little computation to find the local sum. Comparing to NCC which calculates local sum for every n , FNCC can save huge computational resource and time.

3.2.1.6 Multidimensional expansion and its application to images processing (DIC)

The concepts of DFT, convolution, cross-correlation, NCC, and FNCC can be expanded to multidimensional function or dataset. For digital-image-processing, 2D images are usually expressed positive two-dimensional matrix of pixels, respectively. After applying the above algorithms, one can track points of interesting by finding the maximum cross-correlation value effectively while sliding latter images over the original or previous image with high efficiency. Based on this, DIC (Digital Image Correlation) algorithms have been developed for 2D images with 2D matrix data sets by using Matlab.

3.2.2 Sub-Pixel algorithm

Due to the intrinsic nature of discontinuities of digital images, which are composed of a certain number of pixels, the accuracy of cross-correlation is limited to the size of a pixel and the estimated displacement fields necessarily contain sub-pixel scale errors. To solve this problem, the sub-pixel algorithm based on the quadratic interpolation is additionally implemented. Sub-pixel precision is achieved by fitting a 2nd order polynomial to the maximum correlated point and its surrounding points and finding the local extremum of the polynomial. If the extremum is inside the region enclosed by the surrounding points, its position can be considered to be the position of the actual correlated point while the maximum correlated point from the correlation is considered to be real correlated point when it falls outside of the region.

In case of 2D image, assume f is the 2nd order polynomial fitted to the maximum correlated point and the 8 points surrounding it and then

$$\begin{bmatrix} u_{-1,-1} & u_{0.-1} & u_{1,-1} \\ u_{-1,0} & u_{0,0} & u_{1,0} \\ u_{-1,1} & u_{0,1} & u_{1,1} \end{bmatrix} \cong \begin{bmatrix} f(-1,-1) & f(0,-1) & f(1,-1) \\ f(-1,0) & f(0,0) & f(1,0) \\ f(-1,1) & f(0,1) & f(1,1) \end{bmatrix} \tag{3-18}$$

where $f(x,y) = A + Bx + Cy + Dxy + Ex^2 + Fy^2$

Writing this in matrix form

$$u \cong \phi X \text{ , where } u = \begin{bmatrix} u_{-1,-1} \\ u_{-1,0} \\ u_{-1,1} \\ u_{0,-1} \\ u_{0,0} \\ u_{0,1} \\ u_{1,-1} \\ u_{1,0} \\ u_{1,1} \end{bmatrix}, \quad \phi = \begin{bmatrix} 1 & -1 & -1 & 1 & 1 & 1 \\ 1 & -1 & 0 & 0 & 1 & 0 \\ 1 & -1 & 1 & -1 & 1 & 1 \\ 1 & 0 & -1 & 0 & 0 & 1 \\ 1 & 0 & 0 & 0 & 0 & 0 \\ 1 & 0 & 1 & 0 & 0 & 1 \\ 1 & 1 & -1 & -1 & 1 & 1 \\ 1 & 1 & 0 & 0 & 1 & 0 \\ 1 & 1 & 1 & 1 & 1 & 1 \end{bmatrix} \quad X = \begin{bmatrix} A \\ B \\ C \\ D \\ E \\ F \end{bmatrix} \tag{3-19}$$

The least square solution, X of this form, i.e., ($\|u - \phi X\|$ is as small as possible) can be found through matrix calculation.

$$X = (\phi^T \phi)^{-1} \phi^T u \tag{3-20}$$

Once the approximate f is found, the coordinates of the extremum can be obtained through partial derivatives such as

$$\begin{aligned} \frac{\partial f}{\partial x} &= B + Dy_{extremum} + 2Ex_{extremum} = 0 \\ \frac{\partial f}{\partial y} &= C + Dx_{extremum} + 2Fy_{extremum} = 0 \end{aligned} \tag{3-21}$$

Finally the real correlated position is determined depending on where the point, $(x_{extremum}, y_{extremum})$ falls.

3.2.3 Data smoothing

One of the superior application of DIC is to measure deformation of materials in form of strain and displacement. Strains are calculated from displacement gradient based on infinitesimal strain theory. However, strains are quite sensitive to the displacement errors especially when the distances between the grid points are small. Tracking multiple grid points to generate strain field usually involves highly dense grid arrays, and rough strain field is frequently generated even from a reasonably smooth displacement data set. To resolve this problem we employed a smoothing algorithm for uniformly

constructed dataset [53]. It is worth noting that image data can be considered equally spaced data set. Smoothing function reduces small-scale experimental noise or error while keeping the most important imprints of a dataset by eliminating random error e_i from the original data y_i.

$$y_i = \hat{y}_i + e_i \tag{3-22}$$

, where $\hat{y}_i$ is an unknown smoothing function or smoothed data which is the goal of the smoothing process. It would be a suitable method to smoothen coarse strain field image. The employed approach to smoothing is the penalized least square regression [54] that minimize a criterion function F while balances the fidelity to the data using the following equation:

$$\min\{F(\hat{y})\} = \min\{\sum_{i=1}^{n}(\hat{y}_i - y_i)^2 + sP(\hat{y})\} \tag{3-23}$$

, where the first term in right-hand side is the residual sum of squares (RSS), s is a real smoothing parameter, that controls the degree of smoothing, and $P(\hat{y})$ is roughness of smoothed data which can be expressed by using a second-order divided difference [55] as

$$P(\hat{y}) = \left\|D\hat{y}\right\|^2 \tag{3-24}$$

, where $\left\| \right\|$ denotes the Euclidean norm and D is a tri-diagonal square matrix, for which the equally spaced data is given.

$$D = \begin{pmatrix} -1 & 1 & & & \\ 1 & -2 & 1 & & \\ & \ddots & \ddots & \ddots & \\ & & 1 & -2 & 1 \\ & & & 1 & -1 \end{pmatrix} \tag{3-25}$$

Minimizing $F(\hat{y})$ in Eq. (3-23) using Eq. (3-24) gives following linear system that allows the determination of smoothed data

$$\hat{y} = (I_n + sD^T D)^{-1} y \tag{3-26}$$

, where I_n and D^T are the n by n identity matrix and the transpose of D, respectively. At this point it is important to use an appropriate smoothing parameter to avoid over- or under- smoothing as much as possible. Such a correct value can be estimated by the method of generalized cross validation (GCV) introduced by Wahba [56]. Assuming that one wants to solve the smoothing linear system

$$\hat{y} = H(s)y \tag{3-27}$$

, where H is the so-called hat matrix (here, $H(s) = (I_n + sD^T D)^{-1}$), the GCV method picks the parameter s that minimizes the GCV score given by

$$GCV(s) \equiv \frac{\sum_{i=1}^{n} (\hat{y}_i - y_i)^2 / n}{(1 - Tr(H)/n)^2} \tag{3-28}$$

, where Tr denotes the matrix trace, which can be simply reduced to

$$Tr(H) = \sum_{i=1}^{n} \frac{1}{1 + s\lambda_i^2} \tag{3-29}$$

, where $(\lambda_i^2)_{i=1,2,...,n}$ are the eigenvalues of $D^T D$. The GCV score thus reduces to

$$GCV(s) \equiv \frac{n\sum_{i=1}^{n} (\hat{y}_i - y_i)^2}{(n - \sum_{i=1}^{n} \frac{1}{1 + s\lambda_i^2})^2} \tag{3-30}$$

The smoothing algorithm can be fully automated through finding a s value that minimizes the GCV score expressed in Eq. (3-30). However, since the components of $\hat{y}$ appear in the expression of the GCV score, $\hat{y}$ has to be calculated at each step of the minimization process giving rise to huge computational load. Nonetheless, this can be avoided in our case because of equally-spaced data set.

An Eigen-decomposition tri-diagonal square matrix D for the equally spaced yields

$$D = U\Lambda U^{-1} \tag{3-31}$$

, where Λ is the diagonal matrix containing the eigenvalues of D defined by Yueh [57]:

$$\Lambda = diag(\lambda_1,...,\lambda_n) \text{ with } \lambda_i = -2 + 2\cos((i-1)\pi/n) \tag{3-32}$$

And U is a unitary matrix (i.e. $U^{-1} = U^T$ and $UU^T = I_n$), where U^T and U are n-by-n type-2 discrete cosine transform (DCT) and inverse discrete cosine transform matrices (IDCT), respectively [57]. Therefore, we can rewrite Eq. (3-26)

$$\hat{y} = U(I_n + s\Lambda^2)^{-1}U^T y \equiv U\Gamma U^T y = IDCT(\Gamma DCT(y)) \tag{3-33}$$

, where the components of the diagonal matrix Γ are given by

$$\Gamma_{i,i} = [1 + s(2 - 2\cos((i-1)\pi/n))^2]^{-1} and \Gamma_{i,i} = 0 \qquad if \quad i \neq j \tag{3-34}$$

Moreover, from Eq. (3-33), the residual sum of squares (RSS) can be written as

$$\begin{aligned} \sum_{i=1}^{n}(\hat{y}_i - y_i)^2 &= \left\|\hat{y} - y\right\|^2 \\ &= \left\|((I_n + s\Lambda^2)^{-1} - I_n)DCT(y)\right\|^2 \\ &= \sum_{i=1}^{n}\left(\frac{1}{1+s\lambda_i^2} - 1\right)^2 DCT_i^2(y) \end{aligned} \tag{3-35}$$

, where DCT_i refers to the i^{th} component of the discrete cosine transform. Note unitary matrix preserves length. Substituting Eq. (3-34) into Eq. (3-30) gives

$$GCV(s) \equiv \frac{n\sum_{i=1}^{n}\left(\frac{1}{1+s\lambda_i^2} - 1\right)^2 DCT_i^2(y)}{\left(n - \sum_{i=1}^{n}\frac{1}{1+s\lambda_i^2}\right)^2} \tag{3-36}$$

The computation of the GCV score from this equation is straightforward and does not require any matrix operation and manipulation, which improves the speed of automated smoothing. Once s value is determined, smoothed function, $\hat{y}$ can be obtained by Eq. (3-26).

3.3 AFM image scanning mode and image reconstruction

AFM images are generated by recording the interaction forces between tip and surface while the cantilever is scanned over the sample surface. The scanner and the electronic feedback circuit, together with sample, cantilever, and optical lever form a feedback loop set up for the purpose. The

presence of a feedback loop is a key difference between AFM and other classical instruments so that AFM not only measures the force on the sample but also controls it, allowing acquisition of images at very low tip-to-sample force [58].

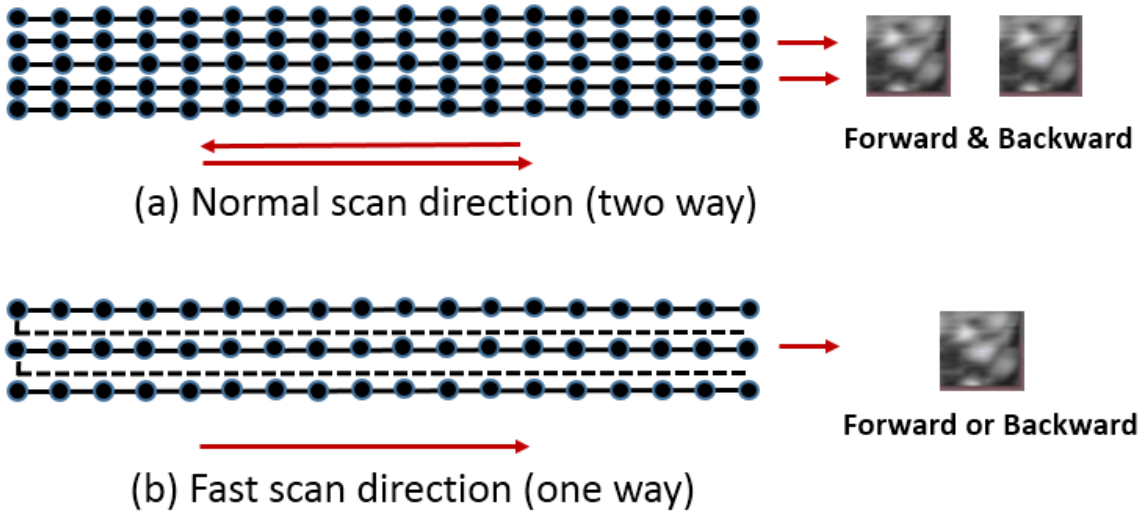

Figure 16: Two typical image acquisition. (a) The AFM scanner go across the first line from left to right then scan back from the right to the left, and so forth. (b)The AFM electronics drive the scanner across the first line of the scan and then lift it back. After stepping in the perpendicular direction to the second scan line, moves across it and back, then to the third line, and so forth.

The scanner is an extremely accurate positioning stage used to move the tip over the sample (or the sample under the tip) to form an image, which is made from a piezoelectric tube. Two general scanning methods have been demonstrated in Figure 16. The two-way scanning mode generates two images (one is for forward direction, the other is for backward direction), which provides more reliable images than one-way scanning mode does but sacrifices scanning speed (one-way scanning is two times faster than two-way scanning). In most of research, two-way scanning mode is more preferable since the forward and backward trace will show how well the tip is contacting the sample surface. For example, when AFM scans over a calibration grid (a side view of sample surface is shown in figure 17 (a)), topography signal of surface can be observed in real time. If and only if forward and backward trace

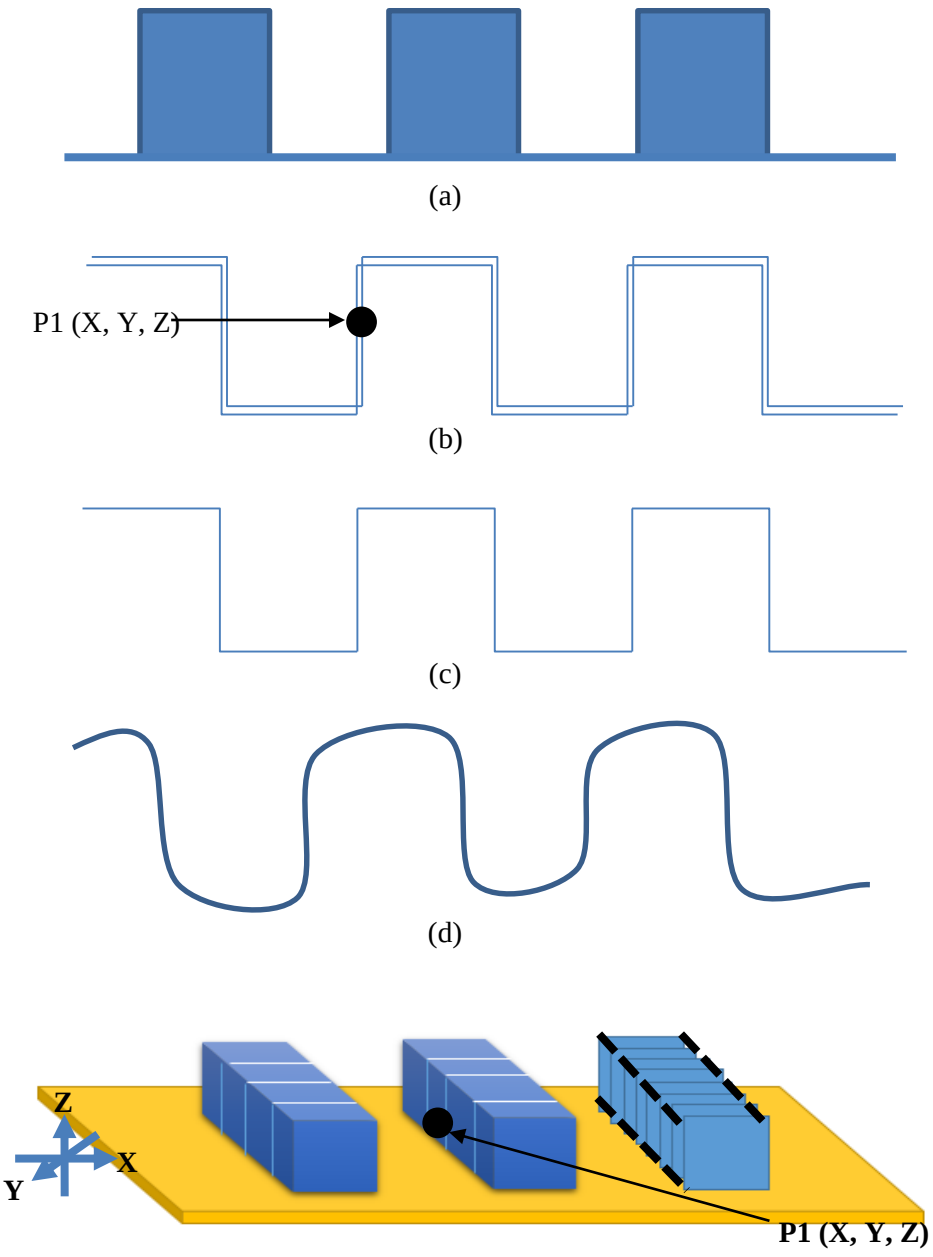

Figure 17: Topography view of sample surface and image reconstruction. (a) Side view of a calibration grid base. (b) Topography signal of sample surface in two-way direction mode. (c) Topography signal of sample surface in one-way direction mode (good contact). (d) Topography signal of sample surface in one-way direction mode (bad contact). (e) AFM image generated by using cross section stack method. Each cross section is scanned through progressive scanning and stack together to form a 3D images. P1 is the same point in line view shown in (b).

match with each other (as shown in figure 17(b)), the topography information can be regarded as reliable results. On the other hand, in figure 17(c) & (d), topography information in fast scan mode is presented. Figure 17 (c) shows the topography of sample surface where tip fit to sample surface very well; however, sometimes the tip can't fit the surface well, which has been shown in Figure 17(d). No one can judge its validity since there is no backward trace that can be referred.

As the probe is scanning over the surface, a topographic image is obtained storing the vertical control signals (Z signals from Z scanners) and plane control signals (X-Y signals from XY scanners) sent by the feedback circuit to the scanner moving it up and down (left and right) to follow the surface morphology. Those signals can provide the relative *x*, *y*, and *z* coordinates in space of the sample surface to generate 2D or 3D AFM images. The image data are sampled digitally at equally spaced intervals, generally from 64 up to 2048 points per line.

In order to employ DIC techniques, the original XEI image file need to be reconstructed since XEI image is unreadable by Matlab. Normally, the resolution of our AFM is set to 256×256, which contains 65536 pixels or x-y-z coordinate sets. After importing x-y-z coordinates (matrix form) into Matlab, we set x-y coordinates as 2D plane coordinates and make z coordinates as intensity index. Z height data will be normalized to a range of 0 (black) to 1 (white), where brightness of points will be scaled into 256 levels corresponding to the height acquired by the AFM.

3.4 The application of digital image techniques to track live cells and determine the deformation of cells

3.4.1 Introduction

Cell motility or cell migration are major activities in biological tissue formation and remodeling. During several physiological procedures such like embryonic morphogenesis, wound healing, as well as in different pathological situations (e.g. tumor invasion and metastasis [59], [60]), dynamic spatial organization of cells happens. Cell motility is the result of complex interactions involving the formation of cellular protrusion and cell adhesion to extra cellular substrata through the modulation of membrane receptor activity and binding [61]. The resulting changes in cell morphology are coupled to intracellular processes like cytoplasmic streaming, cytoskeleton reorganization, organelles, and cell nucleus movements [62]. A quantitative analysis of cell migration and deformation is a vital step to improve our understanding of cell motility properties. Furthermore, a quantification of the modifications in the motility response induced by extracellular factors is of major interest for

analyzing kinetic data where extracellular signals control individual and collective cell migration. The characterization of major macroscopic dynamic aspects of cell motility should give insights into the mechanisms regulating both single cell translocation and cell population behaviors [63].

Cell displacement and local strain are evaluated to quantify cell migration and deformation. However, accurate measurements in a large deformation region has been regarded extremely challenging for soft materials, especially for cells in vivo, due to limitation of conventional mechanical sensors(i.e. size restriction, low accuracy, contact drawback). Recognizing this, some researchers introduced non-contact sensors such as video and laser extensometers supplemented with computer-assisted image analysis methods for characterizing cell motion [64]. For some years, some applications of image motion analysis to biology have been developed, such as amoebae motion characterization [65] or heart motion quantification [66]. Among numerous analysis methods or algorithms, DIC is one the most popular one which can measure the strain field in a large domain. This method tracks the movement of multiple points on the sample surface by comparing images from different deformed states to a reference image. Using relative displacements of the points the complete strain field can be estimated with sub-pixel accuracy [30,49].

There are two general types of referencing schemes: fixed referencing and dynamic referencing. Under fixed referencing, an image from the undeformed state is used as a reference image [67]. This scheme is not susceptible to accumulated error as all comparisons are made back to the undeformed state; however, when specimen deformation becomes severe, the difference between images may prevent accurate results from being obtained. Dynamic referencing overcomes this difficulty by using the previous deformed state as a reference but at the cost of allowing the potential for accumulated error. Many studies, e.g. [68,69] , have used DIC to characterize mechanical properties of materials; however, few studies published in the literature that have considered the effect of referencing scheme on the performance of DIC. This may be partly because the commercial codes utilized do not allow dynamic referencing [70].

Throughout our research, we expect to verify the feasibility of applying DIC techniques on AFM images as well as characterize the migration and deformation behaviors of live cells. Three experiments were designed to realize our goal of study, in which one experiment for solid sample (ceramic) and two for soft samples (fixed and live cells). The first two experiments validated the displacement and strain measurements with actual test results, and the third experiments showed a probably trend of cell motility including migration and deformation.

3.4.2 Experimental setup

3.4.2.1 Ceramic

3.4.2.1.1 Specimen preparation

As a pattern recognizing method, DIC technique requires proper features on the specimen surface so as to "recognize" patterns. Furthermore, AFM requires a relatively smooth sample surface, which at least should be observed very smooth by eyes. According to these two mandatory requirements, a square ceramic base was selected, where random speckle patterns can easily be found and surface can be regarded as smooth one. The geometries of specimen and one gridded AFM image are shown in Figure 19. It was verified in preliminary tests that the surface patterning did not affect the mechanical properties of the specimen. Therefore, scanning area was randomly chosen as long as the peak of surface fluctuation is less than 5 µm (due to Z scanner range limit).

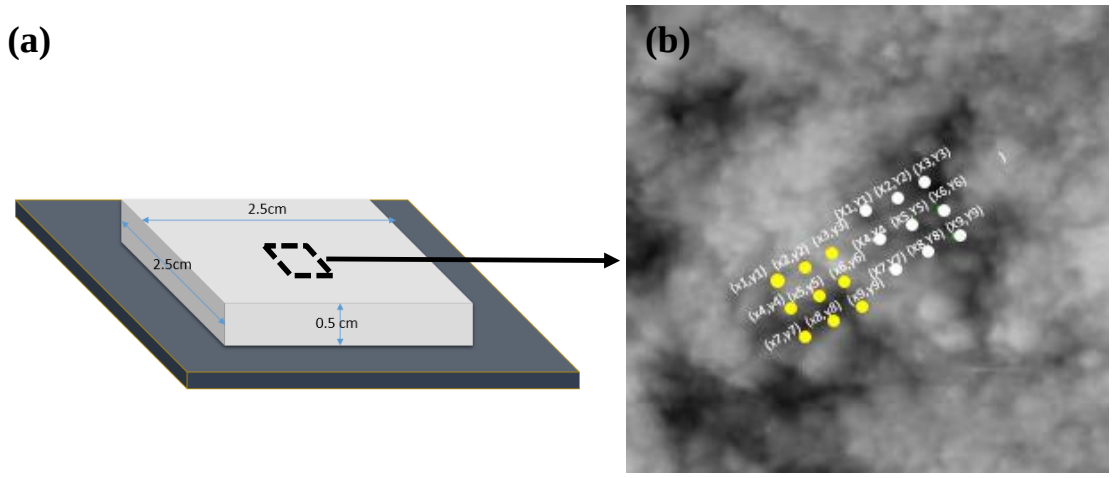

Figure 18: Specimen schematic diagram (a) The geometries of the specimen. (b) Grid points on AFM image for DIC analysis are indicated: undeformed (X_i, Y_i) and deformed (x_i, y_i) positions of grid points.

3.4.2.1.2 Test setup

The ceramic sample base were fixed securely onto the sample plate by magnetic attraction (bottom part is made of iron). AFM images were acquired in contact mode in air medium, using an aluminum coated contact cantilever with thickness of 2 µm, mean with of 50 µm, length of 450 µm, force constant of 0.2 N/m, resonance frequency of 13 kHz, and a pyramidal tip shape (PointProbe®Plus Contact Mode, Nanosensors). The scanning rate was set as 0.5 Hz in order to obtain a good-quality

image without sacrificing scanning speed. A 30 µm x 30 µm smooth area was chosen from optical camera and tip force was set as 40 nN to protect both AFM probes and sample. Seven images was taken continuously, of which a known displacement was made between each two adjacent images (as shown in Figure 19a). The displacement was set from XEP via changing X-Y position of XY scanner.

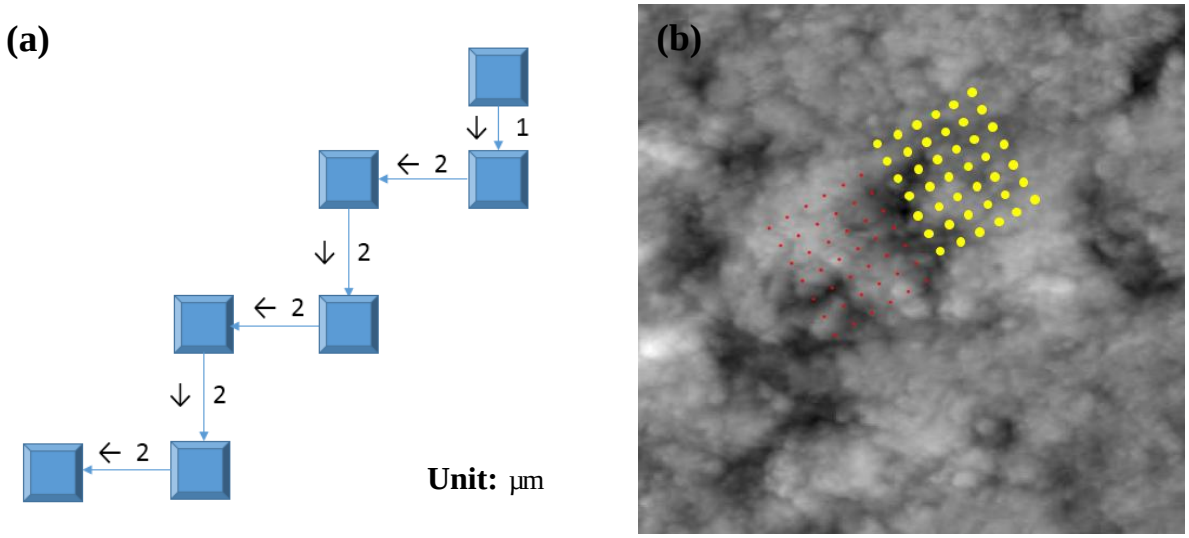

Figure 19: Ceramic surface setup (a) Actual movement plan (b) Gridded (yellow points) AFM image of ceramic sample surface.

Both fixed and dynamic referencing schemes were applied to the list of AFM shifted images to investigate the effect of referencing scheme on DIC performance. Data smoothing function was also applied to all of the images in the list.

3.4.2.2 Fixed cells

3.4.2.2.1 Cell culture

Cells were seeded on polyacrylamide substrates with different concentrations and thus different mechanical properties. Substrates were prepared by mixing acrylamide, bis-acrylamide monomers and APS and TEMED were added to start the polymerization process. Immediately after adding TEMED and APS to the monomer mixture, before polymerization continues a drop of the solution was placed on a microscope slide and a previously activated coverslip was placed on the top of the drop. Solution was flattened due to the weight of the coverslip and polymer coated the surface of the coverslip. After waiting for 15 to 20 minutes, coverslips were peeled from the surface and surface was treated by ECM protein collagen for better cell adhesion. After preparing the substrates, Human

Corneal Epithelial Cells (HCECs) were cultured on the substrate and samples were kept in an incubator at 37C in 5% CO2 and 95% humidity.

3.4.2.2.2 Test setup

The coverslip attached with cell sample was glued firmly onto the petridish by using vacuum grease (Dow corning® high vacuum grease). AFM images were acquired in contact mode in aqueous medium (Phosphate Buffer Solution, or in short, PBS), using a contact cantilever with thickness of 2 µm, mean with of 50 µm, length of 450 µm, force constant of 0.2 N/m, resonance frequency of 13 kHz, and a pyramidal tip shape (PointProbe®Plus Contact Mode, Nanosensors). Instead of using aluminum coated cantilever, gold coated cantilever was selected since we found gold coated cantilever was not easily get contaminated, which allows to provide better reflection signal and reliable images. The scanning rate was set as 0.3 Hz in order to obtain a good-quality image though scanning speed is relatively slow (20 mins/image). A 50 µm x 50 µm clean area, which contained a single fixed cell, was observed and chosen by optical camera. The tip force is far lower than the previous setup (ceramic base), which was set as 0.35 nN to avoid damage to cells. Since feasibility of DIC technique on both X and Y direction had been verified through ceramic sample case (see subheading 3.4.2.1), only X direction (system symmetry) will be verified here. Four images was taken continuously, of which a known displacement was made between each two adjacent images (as shown in Figure 20a). The displacement was set from XEP via changing X-Y position of XY scanner.

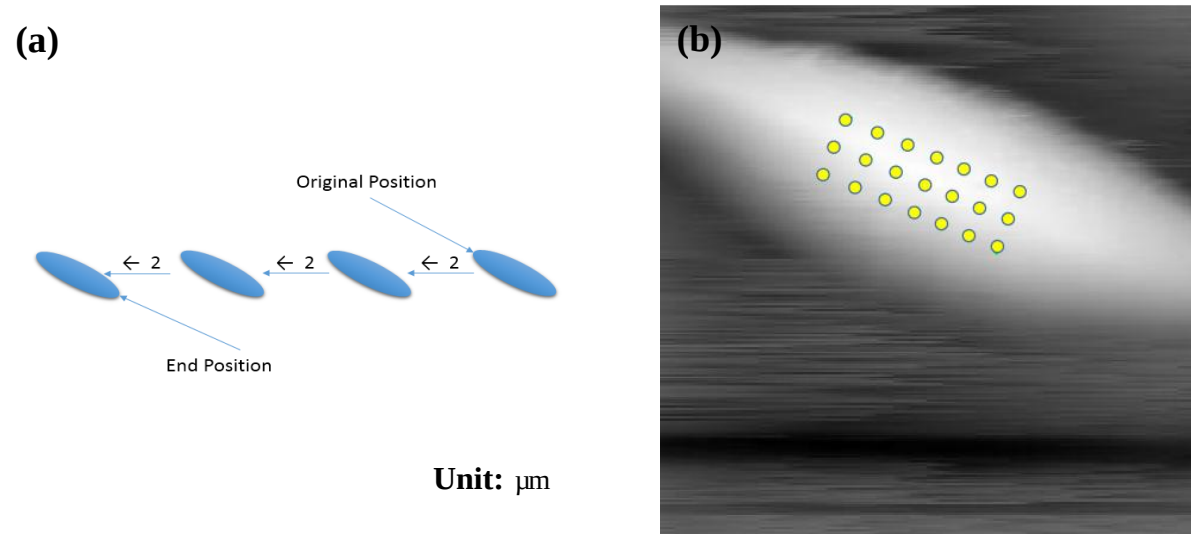

Figure 20: Fixed cell measurement setup (a) Actual movement plan (b) Gridded (yellow points) AFM image of fixed cell surface.

Similarly, both fixed and dynamic referencing schemes were applied to the list of AFM shifted images to investigate the effect of referencing scheme on DIC performance. Data smoothing function was also applied to all of the images in the list.

3.4.2.3 Live cells

3.4.2.3.1 Cell culture

Cells were seeded on polyacrylamide substrates with different concentrations and thus different mechanical properties. Substrates were prepared by mixing acrylamide, bis-acrylamide monomers and APS and TEMED were added to start the polymerization process. Immediately after adding TEMED and APS to the monomer mixture, before polymerization continues a drop of the solution was placed on a microscope slide and a previously activated coverslip was placed on the top of the drop. Solution was flattened due to the weight of the coverslip and polymer coated the surface of the coverslip. After waiting for 15 to 20 minutes, coverslips were peeled from the surface and surface was treated by ECM protein collagen for better cell adhesion. After preparing the substrates, Human Corneal Epithelial Cells (HCECs) were cultured on the substrate and samples were kept in an incubator at 37C in 5% CO2 and 95% humidity.

3.4.2.3.2 Test setup

The test setup of live cells is very similar to the one for fixed cells. The sample coverslip was also glued firmly onto the bottom of petridish by using vacuum grease. AFM images were acquired in contact mode in aqueous medium (PBS), using a gold coated contact cantilever with thickness of 2 μm, mean with of 50 μm, length of 450 μm, force constant of 0.2 N/m, resonance frequency of 13 kHz, and a pyramidal tip shape. The scanning rate was set as 0.2 Hz in order to obtain a good-quality image though scanning speed is relatively slow (30 mins/image). Unlike fixed cells, it is hard to find a single live cell to scan and obtain a successive set of images since “good” (healthy) cells intend to gather together. Thus, a maximum area (90.91 μm x 90.91 μm) was observed and chosen by optical camera. The tip force was set as 0.32 nN to prevent destruction of cells. Because live cells are alive and have motility, there is no need to create displacements artificially. Four images was taken continuously to show the whole process of cell growth and death.

The other difference of test setup is cell culture environment. Live cells need to be kept in an incubator at 37C° in 5% CO2 and 95% humidity to remain active. To realize a living environment for

live cells, we built up a feasible physiological condition for live cells experiments. A diagram of setup for live cells culture environment is shown in Figure 21. Based on our cell culture environment, the live cells can be alive in around three to four hours, which allow us to obtain 6 images ideally.

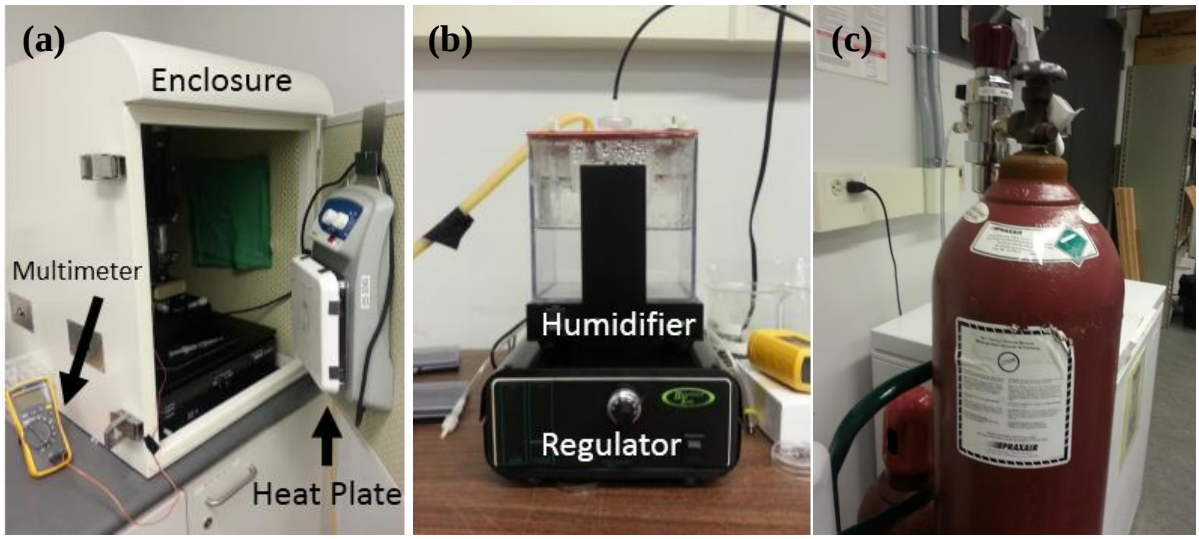

Figure 21: Live cell culture environment setup (a) AFM acoustic enclosure: a heat plate was hang on the door to provide 33-36 C° temperature environment in enclosure, and temperature could be checked by RMS multimeter (116 Industrial Multimeter, Fluke) in real time. (b) Gas control and heated humidifier (Gas control system, Bioscience Tools): A pressure regulator that controls, humidify and heat the flow of 5% CO_2. (c) 5% CO_2 mixed with air gas cylinder.

3.4.3 Results and discussion

3.4.3.1 DIC referencing selection

In Figure 22, the abilities of fixed and dynamic referencing to track the progress of specimen movement are compared. Since the results of both sets of AFM images (ceramic surface and fixed cells) were consistent with each other, only one set of AFM images (ceramic sample) were presented here due to the length of article. When actual displacement of specimen is small, both schemes yield almost the same results; however, as the displacement becomes significant, fixed referencing cannot follow the movements of the grid points (Figure 22(a)), while the dynamic referencing consistently demonstrated excellent tracking capability (Figure 22(b)).

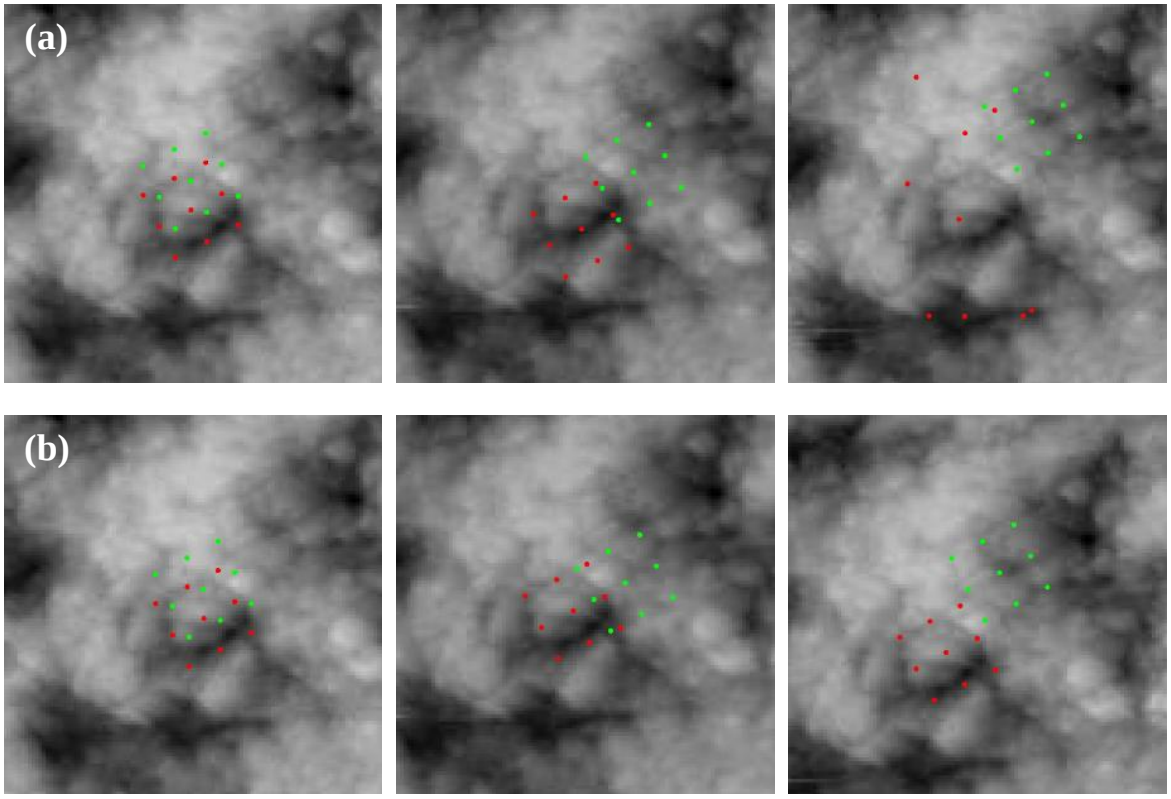

Figure 22: Qualitative comparison of image tracking abilities: (a) fixed referencing, and (b) dynamic referencing.

To demonstrate quantitative comparison between the two referencing schemes, the normalized correlation coefficient (NCC) values of the 9 grid points in Figure 22(a) and 22(b) are plotted in

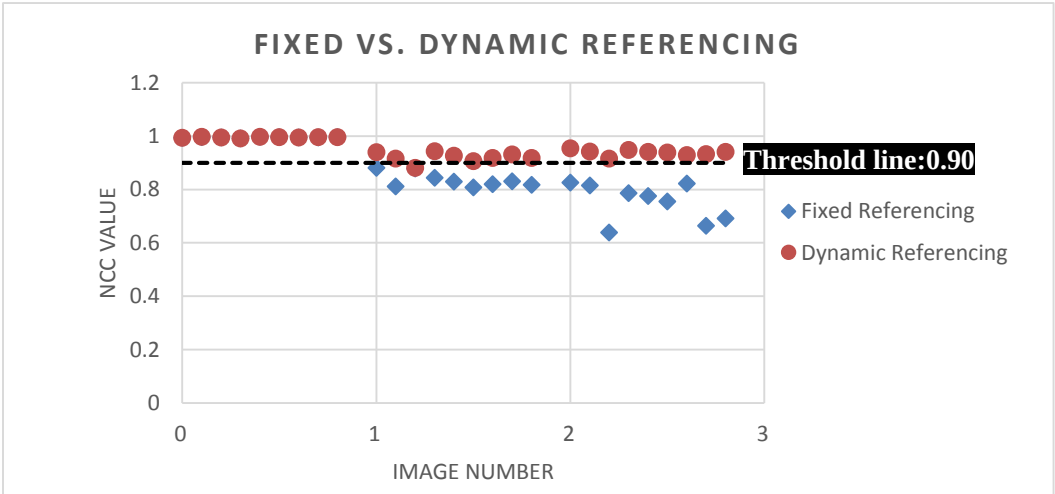

Figure 23: Quantitative comparison between fixed and dynamic referencing schemes

Figure 23. While the NCC value for dynamic referencing is very consistent in the vicinity of 0.95 out of a possible 1.0; a steady decline and increasing scatter for the fixed referencing scheme indicate a decreasing ability to identify the new location of a point with increasing displacement. When the actual displacement exceeds 2 μm, the NCC value drops below the threshold of 0.90 indicating that the result is unreliable (black dashed line: threshold line).

3.4.3.2 Error analysis

In order to evaluate actual effect of applying DIC technique on AFM images, we employed error analysis to examine its functionality. The trace of ceramic surface and fixed cells were shown in Figure 19a and Figure 20a respectively. After applying DIC technique, we have the results shown as following:

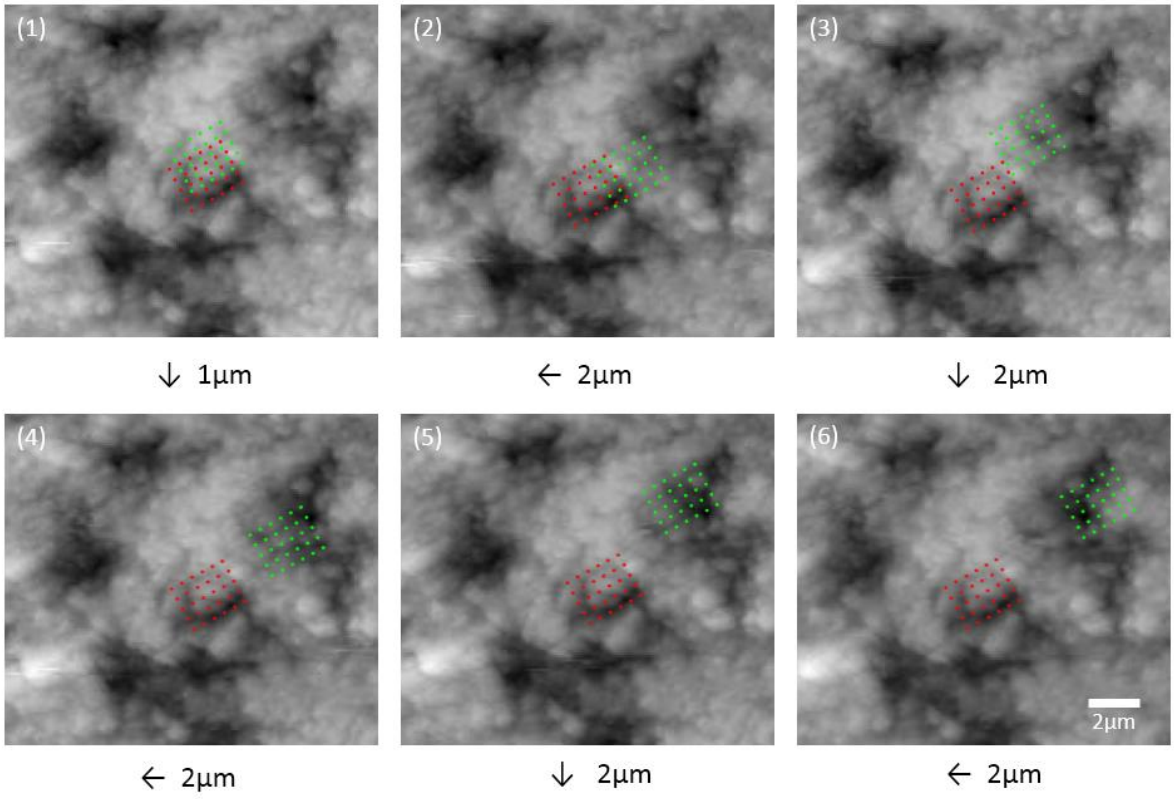

(a) Ceramic sample surface

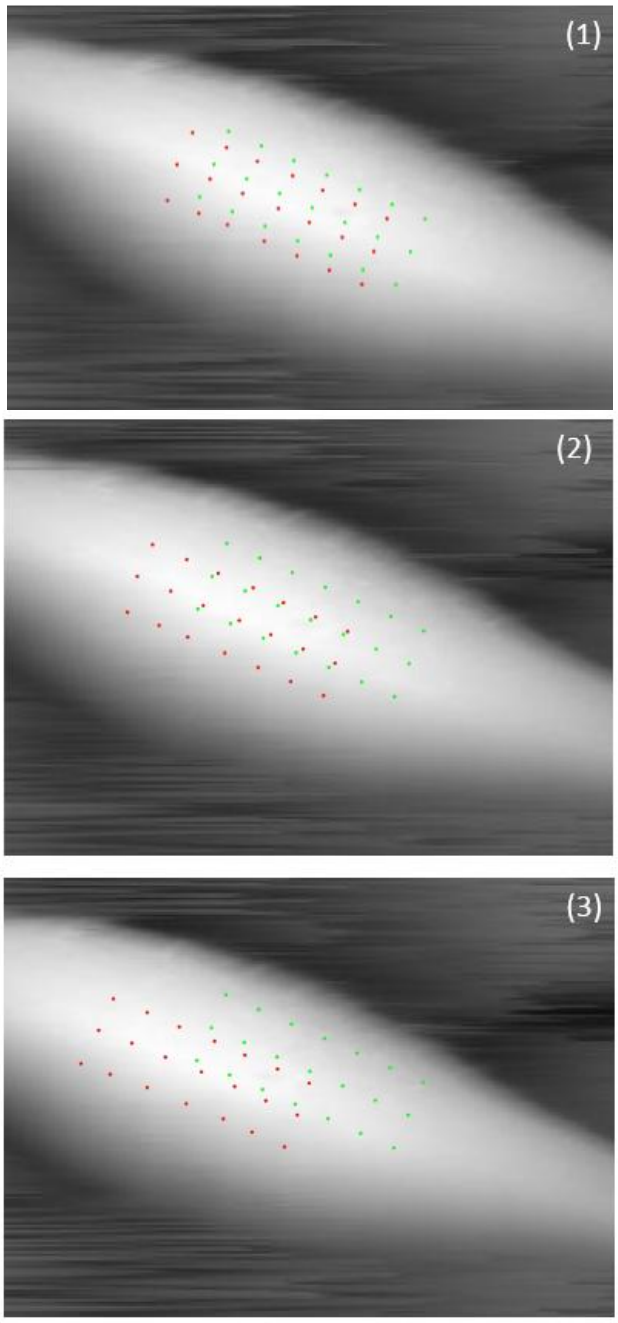

(b) Fixed cells

Figure 24: DIC tracking results of AFM images: (a) ceramic surface (b) fixed cells

Figure 24 shows the trace of AFM images. All of the NCC values of grid points in Figure 24(a) are above 0.9 along with average value at 0.9935 and standard deviation (STD) at 0.0027, while the NCC values of grid points in Figure 24(b) are above 0.9 along with average value at 0.9963 and STD at

0.0028. Therefore, the above results can be regarded as reliable ones. Statistic results of NCC values were shown in Table 1.

Table 1. Statistic results of NCC values for ceramic sample and fixed cells

	Maximum	Minimum	Average Value	Standard Deviation
Ceramic sample	0.997432	0.982697	0.993474	0.002711
Fixed cells	0.999485	0.988132	0.996275	0.002844

Through comparing the difference between displacements of X, Y position obtained from DIC results and actual displacement of sample (known in advance), we conducted the error analysis, which including: the normalized average of absolute error and corresponding percentage error. Since the actual displacement is not all the same (varies from 1 to 2μm), it is essential to normalize data so that comparison can be made. The normalized absolute error on X (or Y) direction can be defined as:

$$e_{Abb\_X} = \left| \frac{D_{DIC\_X} - D_{Actual\_X}}{D_{Actual\_X}} \right| \;\&\; e_{Abb\_Y} = \left| \frac{D_{DIC\_Y} - D_{Actual\_Y}}{D_{Actual\_Y}} \right| \qquad (3\text{-}36)$$

where $D_{DIC\_X} = (X_i - X_R)$, $D_{DIC\_Y} = (Y_i - Y_R)$, X_i and X_R can be directly obtained from DIC results while D_{Actual_X} and D_{Actual_Y} is set via assigning value to X, Y position in XEP software. Here, we assume that there is no systematic error on our X, Y scanner since we cannot find relevant materials from manufacture and the scanner should be calibrated automatically by XEP built-in function.

After calculating normalized absolute error of a single grid point, we consider the whole gridding area by taking an average of normalized absolute error for all grid points. Detailed information has been illustrated in Figure 25.

Table 2. Total error average

	Total error average (X direction)	Total error average (Y direction)
Ceramic sample	1.28%	6.67%
Fixed cells	2.85%	N/A

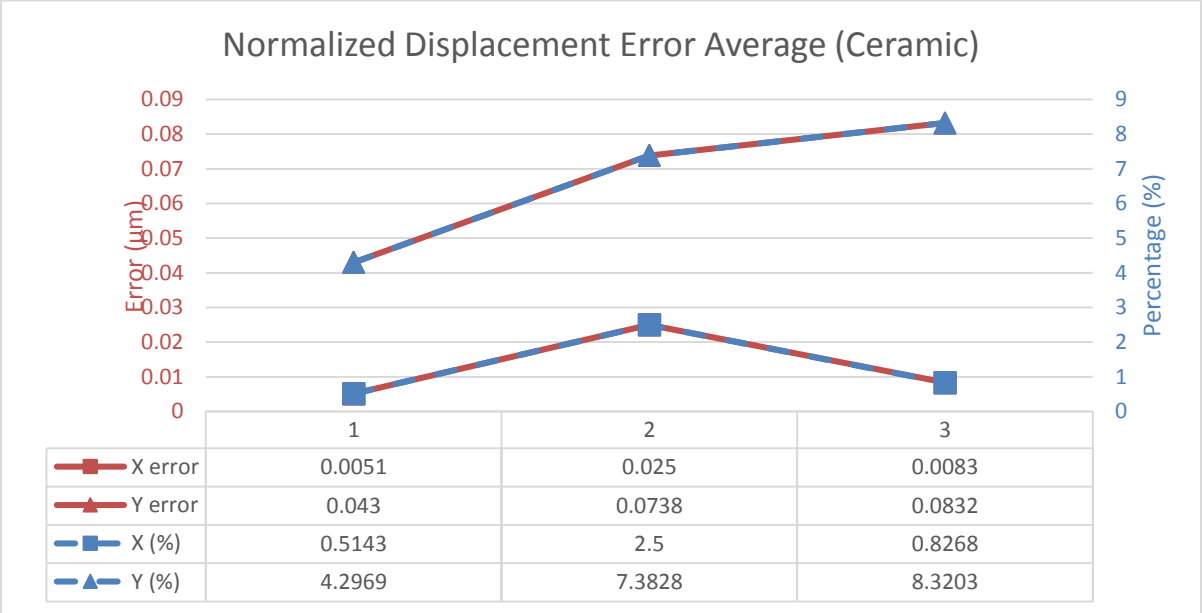

	1	2	3
X error	0.0051	0.025	0.0083
Y error	0.043	0.0738	0.0832
X (%)	0.5143	2.5	0.8268
Y (%)	4.2969	7.3828	8.3203

(a)

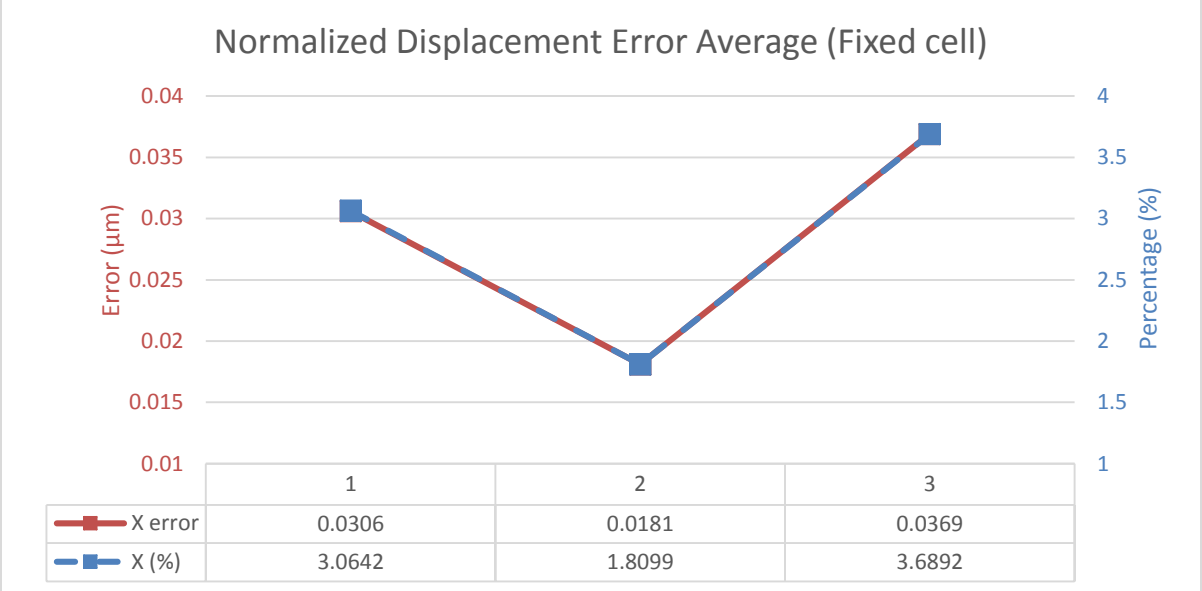

	1	2	3
X error	0.0306	0.0181	0.0369
X (%)	3.0642	1.8099	3.6892

(b)

Figure 25: Error between DIC results and actual displacements (a) Normalized displacement error average (Ceramic) (b) Normalized displacement error average (Fixed cell)

The total error average on X direction of ceramic sample is 1.28% (0.01 µm), which of fixed cells is 2.85% (0.03 µm). The reason is inherent characteristic of materials. Ceramic sample is in solid

form, which allows AFM to obtain very stable images if there is no deformation made by external load. However, the fixed cells is more vulnerable to a few external factors, such as floating hazards in fluid and unexpected strain caused by tip force, which are unpredictable. Thus, it is harder and almost impossible to maintain exact the same topography of cell sample (AFM images) via successive shifting scanning (by moving sample plate). Moreover, there is an obvious gap between displacement error on X direction and Y direction, which will be discussed later.

For further verification of error data, we introduced standard deviation (STD). STD could be used to reveal the discrete degree of data or dispersion from the average value. A small STD value of a data set indicates the robustness of data set. The equation for calculating STD value can be defined as:

$$STD = \sqrt{\frac{1}{N}\sum_{i=1}^{N}(x_i - \bar{x})^2} \tag{3-36}$$

Calculated STD of displacement error is illustrated in Figure 26.

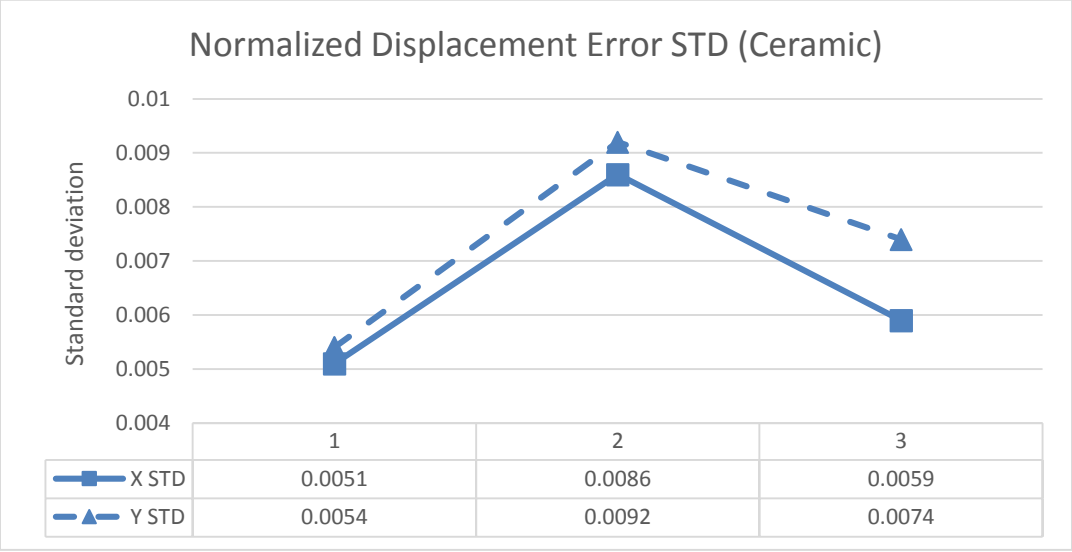

(a)

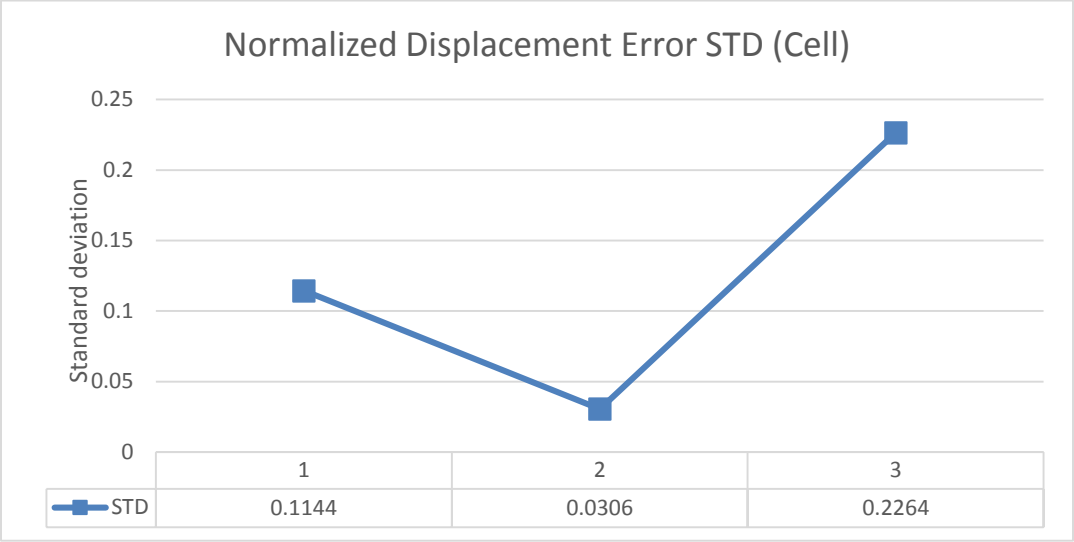

(b)

Figure 26: Displacement Error STD (a) Ceramic sample (b) Fixed cells

According to Figure 26a, we found that the STD is small compared with its actual displacement (at about 0.05%~0.1%). While figure 26b, revealed STD in cell test relatively significant (at about 3%~20%).

Also, we found the STD value in cell test was not as stable as the ones in ceramic test, which may raise the concern of instability of test data.

3.4.3.3 Strain and displacement analysis

3.4.3.3.1 Stress/strain Calculation

The frequently used- Engineering stress, σ_E and strain, ε_E were calculated using the following relationships,

$$\sigma_E = \frac{F}{A_0} \tag{3-37}$$

$$\varepsilon_E = \frac{\Delta L}{L_0} \tag{3-38}$$

, where F is the force measured by the load cell, A_0 initial cross-sectional area, L_0 original length and ΔL elongation. Take the Figure 18b as an example, the nine rectangular grid points were chosen in

the middle of ceramic surface to be tracked by the FNCC algorithm. The engineering strain was calculated by averaging the strains of those points as:

$$\varepsilon_E = \frac{\Delta L}{L_0} = \frac{(y_3 + y_6 + y_9 - y_1 - y_4 - y_7) - (Y_3 + Y_6 + Y_9 - Y_1 - Y_4 - Y_7)}{(Y_3 + Y_6 + Y_9 - Y_1 - Y_4 - Y_7)} \tag{3-39}$$

, where Y_i are the y-directional coordinates of grid points on the undeformed image, and y_i y-coordinates of the same grid points on the deformed images tracked by DIC. True strains in x- and y-axis directions were also calculated from the displacements of grid points as

$$(\varepsilon_x)_T = \ln \frac{L_f}{L_0} = \ln \frac{(x_3 + x_6 + x_9 - x_1 - x_4 - x_7)}{(X_3 + X_6 + X_9 - X_1 - X_4 - X_7)} \tag{3-40}$$

$$(\varepsilon_y)_T = \ln \frac{L_f}{L_0} = \ln \frac{(y_3 + y_6 + y_9 - y_1 - y_4 - y_7)}{(Y_3 + Y_6 + Y_9 - Y_1 - Y_4 - Y_7)} \tag{3-41}$$

Note that displacement rate (i.e. infinitesimal strains, $\varepsilon_{ij} = 0.5(\partial u_i / \partial x_j + \partial u_j / \partial x_i)$) are commonly adopted for strains in DIC applications; however, this is not valid in large deformations. By using built-in gradient function in Matlab, we obtain the strain field map.

For large deformations (over 10%), we designed a new algorithm (as shown in Figure 27). The basic

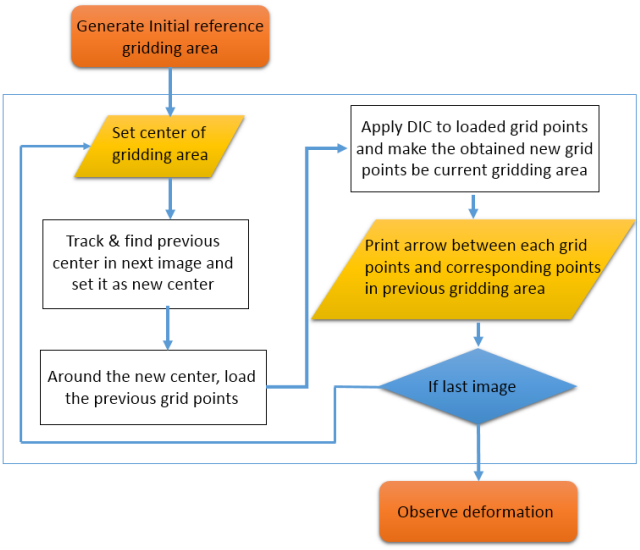

Figure 27: New algorithm for large deformation

idea of new algorithm is to couple nucleus displacement with local deformations in other part of cell. Currently, this method is only able to show the trend of deformation, which is not as accurate as strain field images, but is worthy to be developed and improved in future.

3.4.3.3.2 Strain and displacement results

Since there is only translational motion of ceramic surface, no deformation will happen. Therefore, none of grid point should have displacement and no point performs strain. 2D strain field images estimated by DIC are presented with ceramic images in Figure 28. Strain results showed strain obviously showed that there was no deformation on ceramic surface. It is notable that the strain was not exactly zero (0.5% ~ 2% strain) due to the intrinsic sensitivity of strain (displacement gradient errors). The sub-pixel errors and displacement errors discussed in previous section (3.4.3.2).

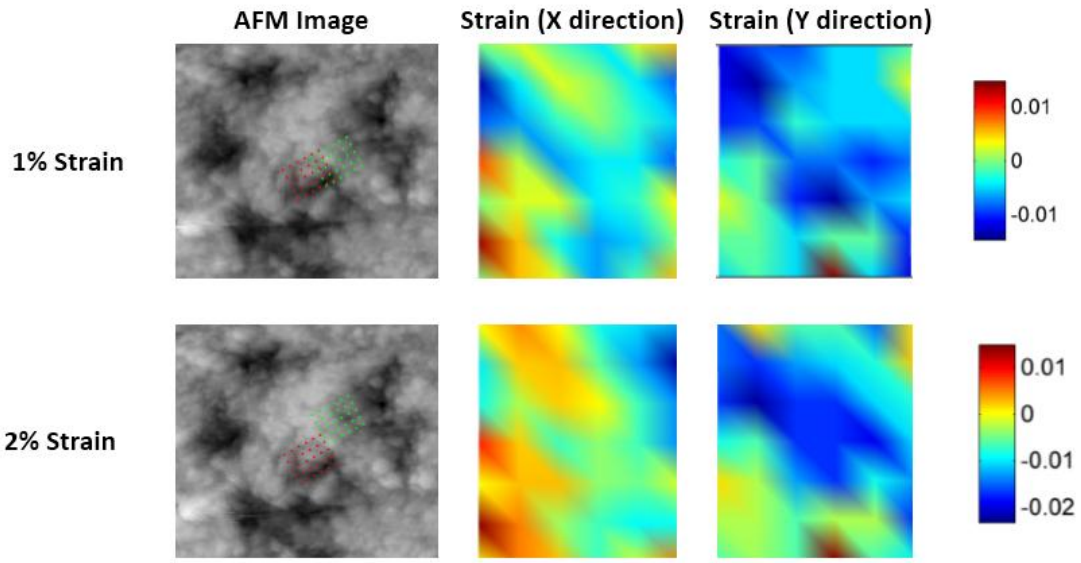

Figure 28: AFM images, strain field (X, Y direction) images of ceramic surface

After verifying DIC codes on ceramic surface, we applied the DIC technique on live cells and observe the deformation of cells throughout its life cycle. Nevertheless, strain field images cannot be generated due to large displacements raised by live cell migration. The strain of each point was larger than 10%; therefore, we performed DIC with new algorithm on each AFM images of live cell (as shown in Figure 29).

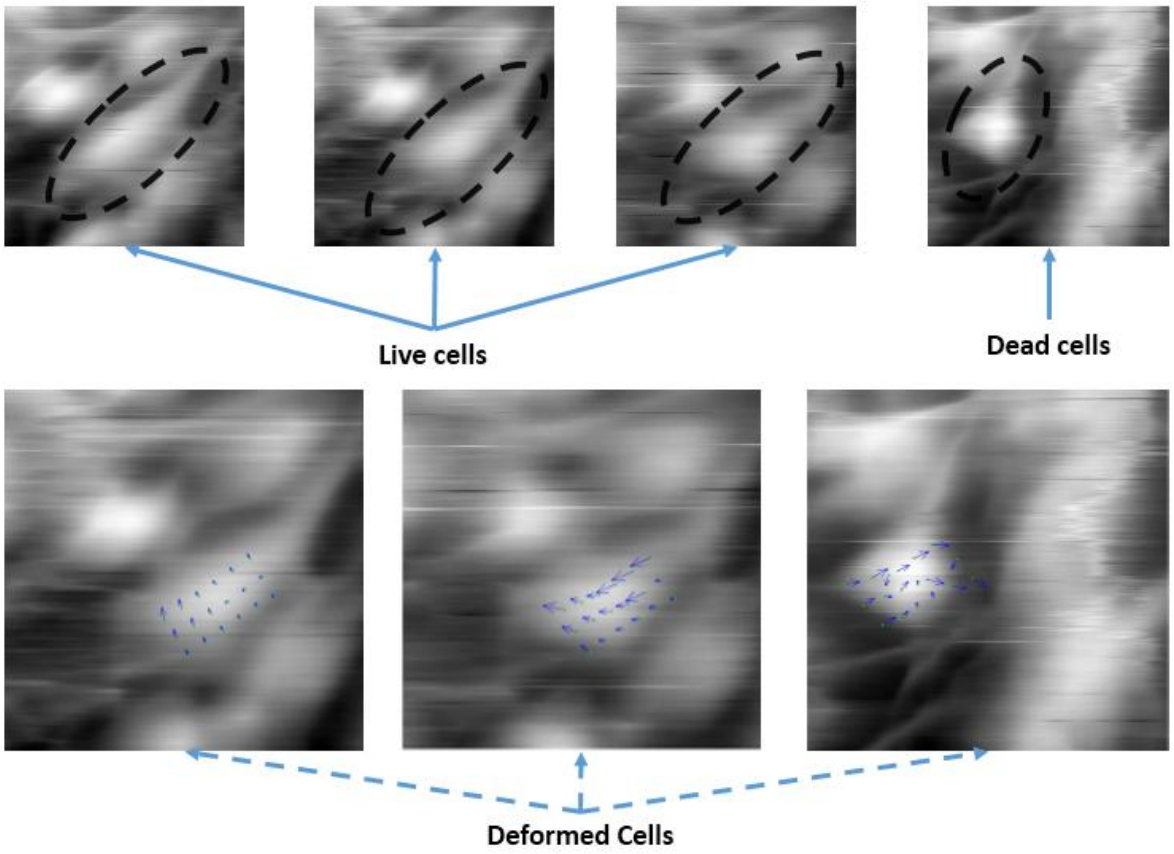

Figure 29: AFM images of live cells applied with new algorithm

"Good" (healthy) live cells intend to gather together. Thus, it is hard to find a single live cell to scan and obtain a successive set of images. As shown in Figure 29, we had four AFM images that recorded the life cycle of a live cell. The healthy cell is elongated, as time goes on, it migrates along with deformation. Finally, it shrinks to a round shape cell. In Figure 29 (second line), the blue arrows indicated the local deformation of live cells. The long arrow represents an elongation while a short one shows a shrinkage. Via comprehensive consideration on all arrows, one could judge the trend of cells (elongating or shrinking).

3.4.4 Conclusion

This study showed the capability of DIC as a cell migration tracker and suggested the potential as a deformation sensor. The selection of referencing scheme has a major influence on the accuracy of DIC results, and the adoption of dynamic referencing in DIC analysis can yield much better results than fixed referencing. Verified by measurement results of ceramic sample and fixed cells, DIC

technique had been successfully applied to AFM images. Comparing with the experiment results of fixed cells, which of ceramic sample is better due to diversity of inherent characteristic of materials. The very soft material resulted in the low quality of AFM images so that the accuracy of DIC decreased. The error analysis results showed that DIC technique is robust, yet there was an obvious difference between the results of X and Y direction. Overall, the displacement error on Y direction is larger than the one on X direction; however, the STD values showed data distribution of both direction was quite similar. Thus, we deduced that the error was caused by systematic error of X-Y scanner (Y direction) in our AFM. Finally, a new algorithm was created in DIC method which could be applied to a large deformation of soft materials. A set of live cell images were obtained and a life cycle of live cell could be observed. The trend of deformation across a large deformation region was revealed by displacement arrows.

To sum up, the feasibility of applying DIC technique and analysis method to AFM images is positive; furthermore, it could be used as a cell migration tracker and deformation sensor. It also may be able to be applied to the studies of other elastomers, gels and biological tissues.

Chapter 4
Mechanical characterization of human corneal epithelial cell by using atomic force microscopy

4.1 Introduction

The cell is the basic building block of all living organisms, hence its function is closely linked with the performance of various tissues in human body. As a result, a good understanding of cell behaviors and properties is fundamental of knowing ourselves clearly. It is now well accepted that the structure of cells essentially determines the cell functions. At different hierarchy levels, many fundamental aspects of cellular function, including shape, deformability, motility, division, and adhesion, is critically characterized by certain mechanical properties (e.g., stiffness, nonlinearity, anisotropy, and heterogeneity). Therefore, the mechanical properties of living cells are strongly associated with the onset and progression of some human disease. For example, any deviations in the mechanical properties may affect its physiological functions and lead to diseases such as malaria [62, 63]. Besides, diseases can also result in structural and mechanical property changes in individual living cells such as cancer [62]. It is obvious that cell structure and properties should be different both in a variety of physiological processes (such as cell differentiation, growth, adhesion, etc.) and under pathogenesis (oxidative stress, attack of viruses, parasites, etc.). As such, cell mechanics can play a pivotal role in the study of human diseases and further help to understand how diseased cells differ from healthy ones.

Cell mechanics mainly deals with the mechanical properties and functions of cells. For a long time there have been two approaches for the study of cell mechanics: (i) the cell mechanical properties were integrally studied, when the cell was considered as a single whole. (ii) Mechanical properties of the cell structural components were studied in details using isolated lipid bilayers, biomembrane and cytosolic proteins [64]. A number of techniques were invented to characterize the mechanical properties of living cells with a well-defined cytoskeleton, such as micropipette aspiration [65], magnetic twisting cytometry [66], laser tracking microrheology [67], magnetic tweezers [68], the optical stretcher [69], and various cell indenters [70–71]. In particular, following its invention in 1986 as a high-resolution imaging tool, the atomic force microscope (AFM) has rapidly become a popular method for studying mechanical properties of living cells in culture [36,27]

This chapter elaborated mechanical characterization of human corneal epithelial cell by using atomic force microscopy. In section 4.2, an overview (together with restraints and assumptions) of the most commonly used nanoindentation model, Hertzian model, were expounded. In section 4.3, experimental setups and implementations of AFM nanoindentation were introduced. In the section 4.4, we quantified and compare the apparent Young's modulus of cells. Basically, the whole mechanical characterization of HCECs can be divided into three parts: (i) measuring elastic modulus distribution across a single cell; (ii) comparing the elastic modulus difference between living cells and dead ones (iii) exploring the effect of Polyacrylamide (PAA) substrate (with different elastic moduli) on HCECs. Lastly, the conclusion and future trend will be stated.

4.2 Theoretical background

4.2.1 Hertzian model (original model)

The general Hertzian model views two half space of spheres in contact. It is assumed that there are no interactions other than elasticity (e.g. viscosity); therefore, no plastic deformation occurs on contact surface. Including linear elasticity, several assumptions are made that the surfaces in contact should be perfectly smooth, that there is no frictional force and that surfaces of bodies in contact can be expressed in equations of the second degree. The mathematical theory of this model was first given by Hertz [72]. In this section, we will introduce the mathematical derivation based on modeling of two spheres.

Assuming that two bodies are in mathematical contact (i.e. unstressed and undeformed) so that the common normal line lies parallel to the applied force, the common tangent plane is the xy plane and the common normal line is the z axis (as shown in Figure 30).

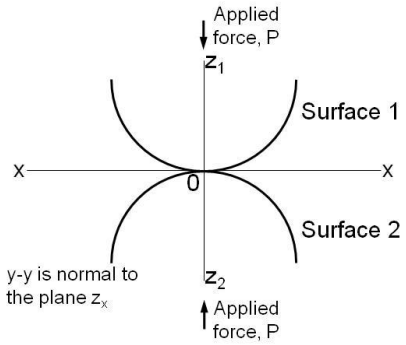

Figure 30: Mathematical contact of two bodies whose surfaces can be expressed in equations of the second degree

First, let's consider the upper surface. The general equation of the second degree is

$$ax^2 + by^2 + cz^2 + 2fyz + 2gzx + 2hxy + 2ux + 2vy + 2wz + d = 0 \quad (4\text{-}1)$$

At the origin, $x = y = z = 0$ then $d = 0$. Differentiating Eq. (4-1) regarding to x and y respectively, which gives:

$$2ax + 2cz\frac{\partial z}{\partial x} + 2fy\frac{\partial z}{\partial x} + 2gz + 2gx\frac{\partial z}{\partial x} + 2hy + 2u + 2w\frac{\partial z}{\partial x} = 0 \quad (4\text{-}2)$$

$$2by + 2cz\frac{\partial z}{\partial y} + 2fz + 2fy\frac{\partial z}{\partial y} + 2gx\frac{\partial z}{\partial y} + 2hx + 2v + 2w\frac{\partial z}{\partial y} = 0 \quad (4\text{-}3)$$

Similarly, $x = y = z = \frac{\partial z}{\partial x} = \frac{\partial z}{\partial y} = 0$ and then $u = v = 0$. Therefore, Eq. (4-1) can be written as

$$ax^2 + by^2 + cz^2 + 2fyz + 2gzx + 2hxy + 2wz = 0 \quad (4\text{-}4)$$

Differentiating Eq. (4-2) and Eq. (4-3) with respect to x and y respectively, and Eq. (4-1) once more with respect to y, which gives:

$$2a + 2cz\frac{\partial^2 z}{\partial x^2} + 2c(\frac{\partial z}{\partial x})^2 + 2fy\frac{\partial^2 z}{\partial x^2} + 2g\frac{\partial z}{\partial x} + 2g\frac{\partial z}{\partial x} + 2gx\frac{\partial^2 z}{\partial x^2} + 2w\frac{\partial^2 z}{\partial x^2} = 0 \quad (4\text{-}5)$$

$$2b + 2cz\frac{\partial^2 z}{\partial y^2} + 2c(\frac{\partial z}{\partial y})^2 + 2f\frac{\partial z}{\partial y} + 2f\frac{\partial z}{\partial y} + 2fy\frac{\partial^2 z}{\partial y^2} + 2gx\frac{\partial^2 z}{\partial y^2} + 2w\frac{\partial^2 z}{\partial y^2} = 0 \quad (4\text{-}6)$$

$$2c\frac{\partial z}{\partial x}\frac{\partial z}{\partial y} + 2cz\frac{\partial^2 z}{\partial x \partial y} + 2f\frac{\partial z}{\partial x} + 2fy\frac{\partial^2 z}{\partial x \partial y} + 2g\frac{\partial z}{\partial y} + 2gx\frac{\partial^2 z}{\partial x \partial y} + 2h + 2w\frac{\partial^2 z}{\partial x \partial y} = 0 \quad (4\text{-}7)$$

At the origin, $x = y = z = \frac{\partial z}{\partial x} = \frac{\partial z}{\partial y} = 0$, and substituting this into Eqs. (4-5), (4-6), and (4-7) respectively, which obtains:

$$2a + 2w\frac{\partial^2 z}{\partial x^2} = 0 \rightarrow \frac{\partial^2 z}{\partial x^2} = -\frac{a}{w} \quad (4\text{-}8)$$

$$2b + 2w\frac{\partial^2 z}{\partial y^2} = 0 \rightarrow \frac{\partial^2 z}{\partial y^2} = -\frac{b}{w} \tag{4-9}$$

$$2h + 2w\frac{\partial^2 z}{\partial x \partial y} = 0 \rightarrow \frac{\partial^2 z}{\partial x \partial y} = -\frac{h}{w} \tag{4-10}$$

Then set $z = f(x, y)$, by using the Taylor's series, we can obtain the approximation form of Eq. (4-4) at the origin point ($x = y = 0$):

$$\begin{aligned} z = f(\partial x, \partial y) = {} & f(0,0) + \partial x f_x(0,0) + \partial y f_y(0,0) \\ & + \frac{1}{2!}\{\partial x^2 f_{xx}(0,0) + 2\partial x \partial y f_{xy}(0,0) + \partial y^2 f_{yy}(0,0)\} \\ & + higher \quad order \quad terms \quad (neglected) \end{aligned} \tag{4-11}$$

(where $f_x = \frac{\partial z}{\partial x}$, $f_y = \frac{\partial z}{\partial y}$, $f_{xx} = \frac{\partial^2 z}{\partial x^2}$, $f_{yy} = \frac{\partial^2 z}{\partial y^2}$, and $f_{xy} = \frac{\partial^2 z}{\partial x \partial y}$)

Since it is the approximation form, we can directly replace ∂x and ∂y by x and y respectively. Substitute $f(0,0) = f_x(0,0) = f_y(0,0) = 0$ and Eqs. (4-8), (4-9), and (4-10) into Eq. (4-11), then we will have:

$$z = f(x, y) = \frac{1}{2}\{-\frac{a}{w}x^2 - \frac{2h}{w}xy - \frac{b}{w}y^2\} \tag{4-12}$$

In any given plane which is parallel to the xy plane in Figure 30, z always keep constant, and then Eq. (3-35) is an ellipse with its principal axes rotated around its coordinate axes. If axes is rotated to a certain position so that the principal axes are aligned with the coordinate axes, the xy term will vanish.

$$x = X\cos\theta + Y\sin\theta \tag{4-13}$$

$$y = -X\sin\theta + Y\cos\theta \tag{4-14}$$

Substituting Eq. (4-13) and Eq. (4-14) into Eq. (4-12), then we have:

$$
\begin{aligned}
z = -\frac{1}{2}\{X^2(&\frac{a}{w}\cos^2\theta + \frac{b}{w}\sin^2\theta - \frac{2h}{w}\cos\theta\sin\theta) \\
&+ Y^2(\frac{a}{w}\sin^2\theta + \frac{b}{w}\cos^2\theta + \frac{2h}{w}\cos\theta\sin\theta) \\
&+ XY(\frac{2a}{w}\sin\theta\cos\theta - \frac{2b}{w}\sin\theta\cos\theta + \frac{2h}{w}(\cos^2\theta - \sin^2\theta)\} \\
= \alpha \times X^2 + \beta \times Y^2 &- XY\{(\frac{a-b}{w})\sin 2\theta + \frac{h}{w}(\cos 2\theta)\}
\end{aligned}
\tag{4-15}
$$

(, where α and β are constants)

When $\tan 2\theta = \frac{b-a}{h}$, the XY term vanishes. Through replacing X and Y by x and y respectively, the equation can be simplified in a form of:

$$z = Ax^2 + By^2 \text{ (, where } A \text{ and } B \text{ are constants)} \tag{4-16}$$

We can determine these constants in terms of geometries of the respective bodies. Let R and R' be the principle radius of curvature of the body for the planes $y = 0$ and $x = 0$, respectively. In the planes $y = 0$ and $x = 0$, we have $Ax^2 = z$ and $By^2 = z$, respectively. Here z is small enough so we can write $z^2 << z$. Therefore, we can assume that the curvature in the plane $y = 0$ is circular with a following equation,

$$x^2 + (z - R)^2 = R^2 \tag{4-17}$$

Reversely ignoring the second-order term of the small quantity z,

$$x^2 = 2Rz \tag{4-18}$$

Since $Ax^2 = z$, therefore,

$$A = \frac{1}{2R} \tag{4-19}$$

Similarly,

$$B = \frac{1}{2R'} \tag{4-20}$$

Therefore, now we can have the equation for upper body by substituting Eqs. (4-19) and (4-20) into the equation (4-16):

$$z_1 = A_1 x^2 + B_1 y^2 = \frac{x^2}{2R_1} + \frac{y^2}{2R_1'} \tag{4-21}$$

And similarly we can find the equation for lower body

$$z_2 = A_2 x^2 + B_2 y^2 = \frac{x^2}{2R_2} + \frac{y^2}{2R_2'} \tag{4-22}$$

Instead of z_2, $|z_2|$ should be used because it is negative. For calculation convenience, z_2 is indicating $|z_2|$ in the rest of derivation. These equations can be combined into a single equation via a summation of two parts.

$$z = z_1 + z_2 = (\frac{1}{2R_1} + \frac{1}{2R_2})x^2 + (\frac{1}{2R_1'} + \frac{1}{2R_2'})y^2 = Ax^2 + By^2 \tag{4-23}$$

Now we compress two bodies together by applying a force parallel to the z-axis as illustrated in Figure 31. If the displacements at a point are w_1 and w_2, then for points inside the area of contact,

$$\begin{aligned} (z_1 + w_1) + (z_2 + w_2) &= \alpha \\ Ax^2 + By^2 + w_1 + w_2 &= \alpha \end{aligned} \tag{4-24}$$

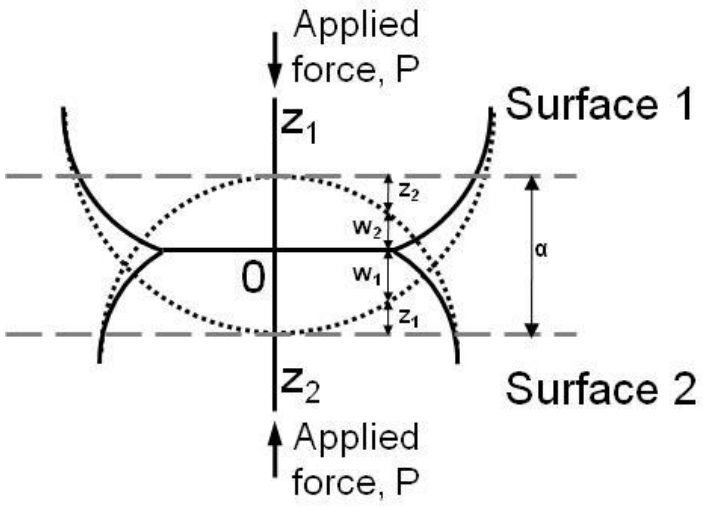

Figure 31: Two bodies in contact under the force applying parallel to the z-axis

While, outside the area of contact

$$(z_1 + w_1) + (z_2 + w_2) > \alpha \tag{4-25}$$

Note α is the sum of w_1 and w_2 at the origin.

Let the component of the pressure at a point (x', y') on the surface be $p(x', y')$. By assuming the surface to be plane, it can be shown that the deformation at a point (x, y) caused by this pressure is given by [71].

$$w(x, y) = \frac{1 - \nu^2}{\pi E} \times \frac{p(x', y')}{\sqrt{(x - x')^2 + (y - y')^2}} dx' dy' \tag{4-26}$$

(, where E and ν are elastic modulus and Poisson's ratio, respectively)

By superposition theorem, the displacement at a point (x, y) caused by the distribution of pressure over an area A is given by

$$w(x, y) = \frac{1 - \nu^2}{\pi E} \times \iint_A \frac{p(x', y')}{\sqrt{(x - x')^2 + (y - y')^2}} dx' dy' \tag{4-27}$$

Substituting Eq. (4-27) into Eq. (4-24), we obtain:

$$\left(\frac{1 - \nu_1^2}{\pi E_1} + \frac{1 - \nu_2^2}{\pi E_2}\right) \times \iint_A \frac{p(x', y')}{\sqrt{(x - x')^2 + (y - y')^2}} dx' dy' = \alpha - Ax^2 - By^2 \tag{4-28}$$

(, where the subscripts 1 and 2 designate the elastic constants for the two bodies)

A solution of Eq. (4-27) yields expression for the area of contact, the pressure distribution over the area, and the compression. This solution can be found by analogy with a problem in potential theory [72].

If an ellipsoid $x^2/a^2 + y^2/b^2 + z^2/c^2 = 1$ has a uniform volume, charge of density ρ, then it can be shown that the potential for points inside the ellipsoid is given by

$$\phi(x, y, z) = \pi \rho abc \int_0^\infty \left(1 - \frac{x^2}{a^2 + \psi} - \frac{y^2}{b^2 + \psi} - \frac{z^2}{c^2 + \psi}\right) \frac{d\psi}{((a^2 + \psi)(b^2 + \psi)(c^2 + \psi))^{1/2}} \tag{4-29}$$

If the ellipsoid is very much flattened, so that c becomes very small, we may write:

$$\phi(x,y)=\pi\rho abc\int_0^{\infty}(1-\frac{x^2}{a^2+\psi}-\frac{y^2}{b^2+\psi})\times\frac{d\psi}{((a^2+\psi)(b^2+\psi)\psi)^{1/2}} \tag{4-30}$$

The potential can also be expressed in a more elementary way as

$$\phi(x,y,z)=\iiint_V\frac{\rho dx'dy'dz'}{\{(x-x')^2+(y-y')^2+(z-z')^2\}^{1/2}} \tag{4-31}$$

If the ellipsoid is very much flattened, z and z' cab be written as zero in Eq. (4-31). Therefore, the resulting expression is integrated with respect to z' over the range $\pm c\sqrt{1-(x'^2/a^2)-(y'^2/b^2)}$

$$\phi(x,y)=2\rho c\iint[1-\frac{x'^2}{a^2}-\frac{y'^2}{b^2}]^{1/2}\frac{dx'dy'}{\sqrt{(x-x')^2+(y-y')^2}} \tag{4-32}$$

Equating Eq. (4-30) and Eq. (4-32) gives

$$\begin{aligned}&\iint[1-\frac{x'^2}{a^2}-\frac{y'^2}{b^2}]^{1/2}\frac{dx'dy'}{\sqrt{(x-x')^2+(y-y')^2}}\\&=\frac{1}{2}\pi ab\int_0^{\infty}(1-\frac{x^2}{a^2+\psi}-\frac{y^2}{b^2+\psi})\times\frac{d\psi}{((a^2+\psi)(b^2+\psi)\psi)^{1/2}}\end{aligned} \tag{4-33}$$

Let's compare Eq. (4-28) with Eq. (4-33). If the right-hand sides are viewed as quadratics in x and y, they have the identical form, while the left-hand sides are integrals of the same form:

$$p(x,y)=k(1-\frac{x^2}{a^2}-\frac{y^2}{b^2})^{1/2} \tag{4-34}$$

Equating the integral $\iint_A p(x,y)dxdy$ to the total force *P*, compressing the two bodies gives $k=3P/2\pi ab$ so

$$p(x,y)=\frac{3P}{2\pi ab}(1-\frac{x^2}{a^2}-\frac{y^2}{b^2})^{1/2} \tag{4-35}$$

Substituting Eq. (4-35) into Eq. (4-28) and using Eq. (4-33)

$$\frac{P}{K\pi}\int_0^{\infty}(1-\frac{x^2}{a^2+\psi}-\frac{y^2}{b^2+\psi})\times\frac{d\psi}{((a^2+\psi)(b^2+\psi)\psi)^{1/2}}=\alpha-Ax^2-By^2 \qquad (4\text{-}36)$$

(, where $\frac{1}{K}=\frac{3}{4}(\frac{1-\nu_1^2}{E_1}+\frac{1-\nu_2^2}{E_2})$ and K is called "Effective modulus of the contacting particles")

As this expression must hold for all values of x and y within contact ellipse, expressions forδ(α), A and B can be obtained by equating coefficients on both sides of Eq. (4-36).

$$\delta=\frac{P}{K\pi}\int_0^{\infty}\frac{d\psi}{((a^2+\psi)(b^2+\psi)\psi)^{1/2}} \qquad (4\text{-}37)$$

$$A=\frac{P}{K\pi}\int_0^{\infty}\frac{d\psi}{(a^2+\psi)((a^2+\psi)(b^2+\psi)\psi)^{1/2}} \qquad (4\text{-}38)$$

$$B=\frac{P}{K\pi}\int_0^{\infty}\frac{d\psi}{(b^2+\psi)((a^2+\psi)(b^2+\psi)\psi)^{1/2}} \qquad (4\text{-}39)$$

Note that A and B are geometric factors, $(1/2R_1+1/2R_2)$ and $(1/2R_1'+1/2R_2')$ given by Eq. (4-23). The constants a and b appeared in Eq. (4-37) are generally unknown, and are determined by from the known geometric factors A and B through Eq. (4-38) and Eq. (4-39).

4.2.2 Extensions of Hertzian model (AFM nanoindentation)

In order to use AFM nanoindentation for determining elastic properties, we need to employ and extend previous Hertzian contact model to a tip-sample system. A sketch of the tip-sample system is given in Figure 32. Instead of two spheres in original model, a sphere indenter and a flat surface (being special case of zero curvature of spheres) constitute the contact objects. The cantilever is bending into the opposite direction while the sample is indented by depth δ. Finally depth δ is calculated by subtracting the cantilever deflection (x) from the height measured (z).

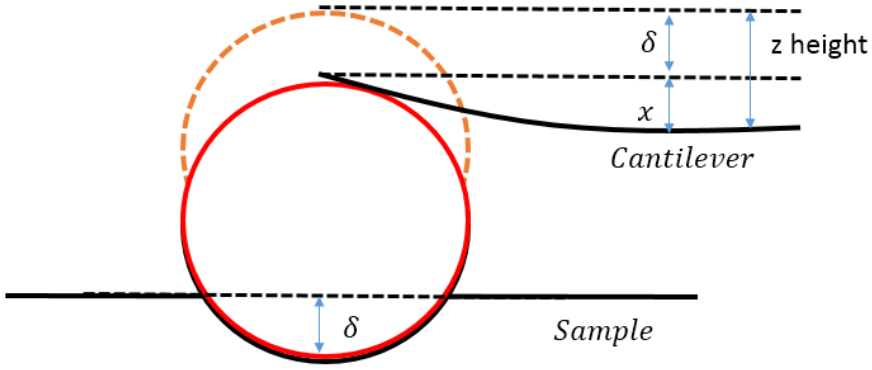

Figure 32: Sketch of the tip-sample system (AFM nanoindentation)

For an essentially nondeformable tip (i.e. with much higher modulus than sample) pushing into a flat compliant ample of elastic modulus E and Poisson's ratio γ, R is simply the tip end radius of curvature. With elastic response then given by:

$$K \approx \frac{4}{3}\left[\frac{E}{(1-\nu^2)}\right] \tag{4-40}$$

Substituting Eq. (4-40) into Eq. (4-37), and calculating the integral of the geometric factors, gives:

$$F = P = \frac{E}{1-\gamma^2}\left[\frac{a^2+R^2}{2}\ln\frac{R+a}{R-a} - aR\right] \tag{4-41}$$

(, where a is the radius of sphere indenter and F is the tip force applied to AFM probe)

Reforming the above equation, we can obtain the young's modulus:

$$E = \frac{F}{\frac{a^2+R^2}{2}\ln\frac{R+a}{R-a} - aR}(1-\gamma^2) \tag{4-42}$$

Similarly, based on Hertzian contact model, we can derive different equations for specific geometry of indenters. Table 3. shows equations for calculation of young's modulus using different tip geometries.

Table 3. Equations of AFM indenters in different geometries

Parabolic	Conical	Four-sided pyramid
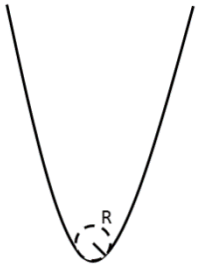	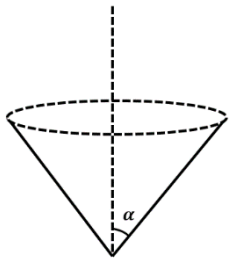	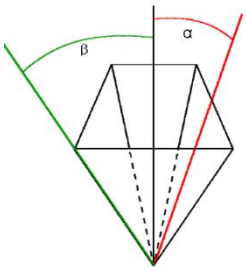
$F=\frac{4}{3}\frac{E}{1-\gamma^2}\sqrt{R}\delta^{3/2}$	$F=\frac{2\tan\alpha}{\pi}\frac{E}{1-\gamma^2}\delta^2$	$F=\frac{E}{1-\gamma^2}\frac{\tan\alpha}{\sqrt{2}}\delta^2$

R, δ, α and γ represent the radius of tip curvature, indentation depth, face angle with respect to vertical direction and Poisson's ratio of sample, respectively.

4.2.3 Issues to be considered

The Hertzian model assumes the indentation to be neglectable in comparison to the sample thickness, thus indentation depth has to be optimized. The Hertzian model is valid for small indentations (say up to 15% of the height of the cell). According to AFM images of HCECs obtained by our AFM, the average height is 2-3 μm. Thus, 200 - 500 nm indentation depth is applicable.

Besides, the Hertzian model assumes absolute elastic behavior as well as homogeneity of sample. But most biological materials are neither homogeneous nor absolutely elastic. The energy delivered by the indenter is not completely given back by a cell but dissipates owing to viscous behavior that also appears as hysteresis between extend and retract force curve (as shown in Figure 33). One time scale describing this behavior is the viscous relaxation time, which brings variations in force indentation measurements if different indentation velocities are tested [73]. Higher indentation velocities result in a higher resistance of the sample material and the overall interaction is more viscous. Thus, the higher loading rate can decrease the extent of indentation at a given force, and then lead to a higher stiffness result. On the contrary, a lower indentation velocity may cause a deeper indentations at a given force because of cell migration. Moreover, the indentation stress may give rise

to an irreversible reorganization of the cell, which increases the difficulties for next measurements. To reduce the influence brought by loading rate, an appropriate speed should be applied to prevent a high viscous response or reorganization of the cell. For HCECs experiment, we set 0.3 μm/s as the loading rate.

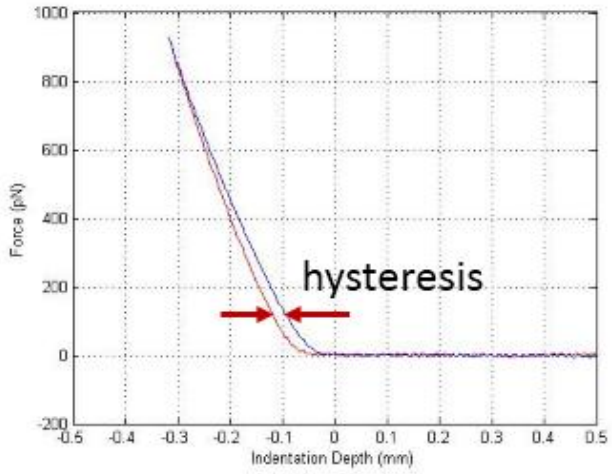

(a)

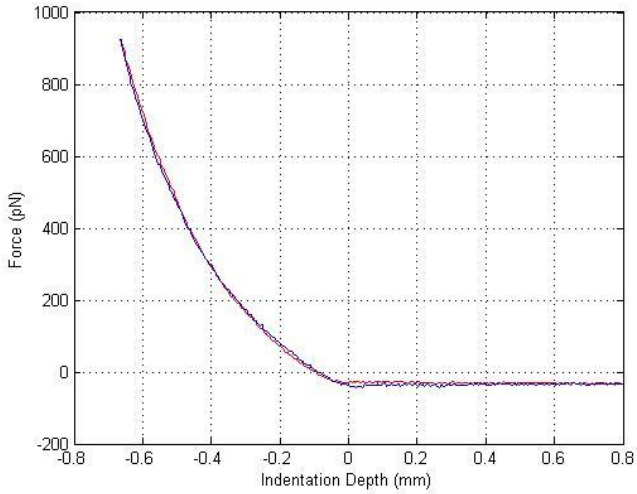

(b)

Figure 33: Force-displacement curve: (a) hysteresis between extend and retract force curve (b) no hysteresis between extend and retract force curve

Lastly, tip selection is also vital to be considered for HCECs experiment. As for AFM test, which cantilever should be used depends on the stiffness of the sample. Since cells are very soft, delicate and soft cantilever available with spring constants of around 0.1 – 0.3 N/m should be used. Another issue with our HECEs sample test was corrosion of coating on cantilever. Because our experiments is fully implemented in medium called Phosphate Buffer Solution (PBS), ordinary cantilever with Aluminum reacted with medium so that most of cantilevers lost coating after experiments (as shown in Figure 34). The loss of coating affect the reelection of laser signal thereby decrease the accuracy of measurements. Therefore, we applied gold coated cantilever to solve the problem.

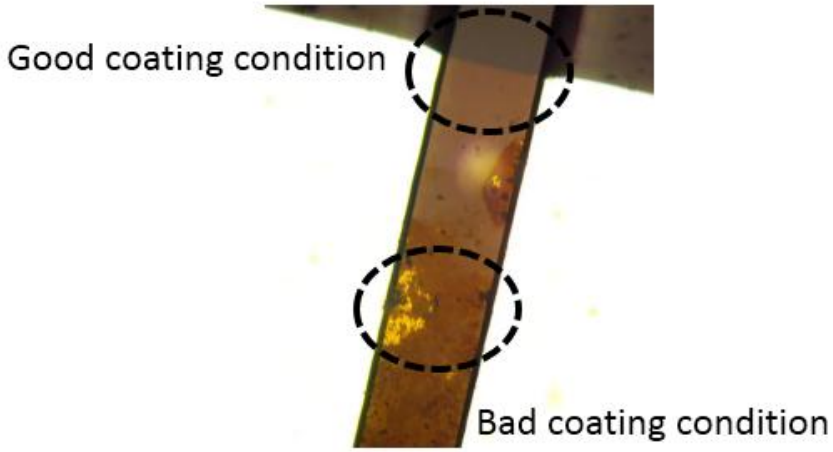

Figure 34: Loss of cantilever coating

4.3 Experimental setup

4.3.1 Sample preparation

Several steps are involved in preparing PAA membranes for cell culture: coverslip activation, membrane fabrication, surface functionalization, and ECM protein conjugation to the surface [74].

4.3.1.1 Coverslip activation

In order to fabricate PAA coated coverslips, glass coverslips (No. 1, 22 ×22 mm, VWR, Radnor, PA) were chemically activated to allow the polymer to covalently bond to them. Coverslips were first rinsed with ethanol. After drying, they were then immersed in 2% (3-aminopropyl) trimethoxysilane (APTMS) (Sigma-Aldrich Canada Co. Oakville, ON) solution in isopropanol for 10 minutes. After four washes in distilled water, coverslips were placed in 1% glutaraldehyde (Sigma-Aldrich Canada

Co. Oakville, ON) solution in distilled water for 30 minutes. Coverslips were then washed three times with distilled water and air-dried before membrane fabrication.

4.3.1.2 Polyacryamide (PAA) membrane fabrication

Membrane fabrication was started with mixing different concentration of acrylamide (40% w/v, Bio-rad, Hercules, CA) and bis-acrylamide (2% w/v, Bio-rad, Hercules, CA) monomers. Variation in elastic modulus was achieved through changing the concentration of acrylamide in the final specimen. The following samples concentrations were used in this study: (1) compliant: 7% acrylamide – 0.01% bis-acrylamide, (2) medium: 10% acrylamide – 0.01% bis-acrylamide, (3) stiff: 15% acrylamide – 0.01% bis-acrylamide. To initiate the polymerization reaction, 10% ammonium persulfate (APS) (Bio-rad, Hercules, CA) solution in water and tetramethylethylenediamine (TEMED) (Bio-rad, Hercules, CA) were added to the monomer mixture. A small volume of each solution (15 µl) was placed on a microscope slide (VWR, Radnor, PA) immediately following the addition of 10% APS solution and TEMED. An activated coverslip was placed on top of the drop so that the solution spread over the coverslip. These assemblies were left for 15 - 20 minutes (depending on concentration; lower concentration samples need more time for polymerization). Following polymerization, assemblies were left in ultra-pure water for 30 minutes before peeling the PAA coated coverslip from the microscope slide. To remove any unreacted monomer, all membranes were soaked in ultra-pure water overnight before surface functionalization.

4.3.1.3 Surface functionalization of membranes and ECM coupling to the surface

In order to conjugate the ECM protein (in this study, collagen type I) to PAA membranes, the surface of the samples was functionalized with a heterobifunctional crosslinker (sulfo-SANPAH). Sample surfaces were covered with 2mg/ml solutions of sulfo-SANPAH (Thermo Scientific, Rockford, IL) in water and membranes were exposed to a UV light source for 10 minutes. Samples were then thoroughly washed with distilled water to clean the surface from excess sulfo-SANPAH. Following functionalization, membranes were covered with 0.05 mg/ml rat tail collagen type I (Sciencell, Carlsbad, CA) solution and incubated for at 37C° for 45 minutes.

4.3.1.4 Cell culture

Human Corneal Epithelial Cells (HCECs) were maintained in an incubator with keratinocyte medium (KM) (Sciencell, Carlsbad, CA) supplemented with keratinocyte growth supplement (KGS)

(Sciencell, Carlsbad, CA) and penstrep (Sciencell, Carlsbad, CA) at 37C° , 5% CO_2 and 95% humidity. Cell culture medium was replaced every 2 to 3 days. After the PAA coated coverslips had been prepared, functionalized and collagen-coated, 4×10^4 HCECs were seeded on these surfaces and samples were kept at 37C° , 5% CO2 and 95% humidity.

Swiss Albino 3T3 fibroblasts were kept in Dulbecco's Modified Eagle Medium (DMEM) supplemented with fetal bovine serum (FBS) and penstrep at 37C° , 5 % CO2, and 95 % humidity incubator. Cell culture medium was changed every two to three days. 3T3s were cultured on PAA samples in the same manner as HCECs.

4.3.2 AFM test setup

The test setup of HECEs is very similar to the one for fixed and live cells discussed in section 3.4.2.2 and section 3.4.2.3. The sample coverslip was glued firmly onto the bottom of petridish by using vacuum grease. AFM images were acquired in contact mode in aqueous medium (PBS), using a gold coated soft contact cantilever for biological applications (PPP-CONTAuD®, Nanosensors). The probe is with thickness of 2 µm, mean with of 50 µm, length of 450 µm, force constant of 0.2 N/m, resonance frequency of 13 kHz, and a pyramidal tip shape. To obtain elasticity of cells, two steps need to be proceeded: imaging and indentation.

During imaging of HECEs, the scanning rate was set as 0.2 Hz in order to obtain a good-quality image though scanning speed is relatively slow (30 mins/image). The tip force was set as 0.32 nN to prevent destruction of cells. Single HCEC is selected by optical camera from XEC software (as shown in Figure 35). The maximum scanning area of our AFM is 90.91 µm x 90.91 µm, which allows to scan all kinds of HECEs (average size of HECE cell is 60 µm x 60 µm).

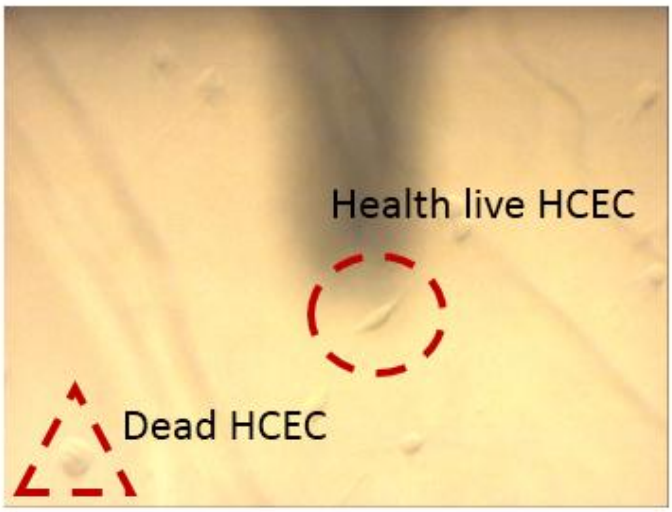

Figure 35: Optical view of HCEC from XEC software

After achieving the image of cells as shown in Figure 36, force-distance spectroscopy mode needs to be proceeded to make indentations on designated spot of cells. Auto Z offset option was checked all the time during the indentation, which protected the probes and sample from damage by XEP software. Loading rate was set as 0.3 µm/s with a tip force at 5 nN. The indentation depth varied from 200 – 500 nm according to specific case.

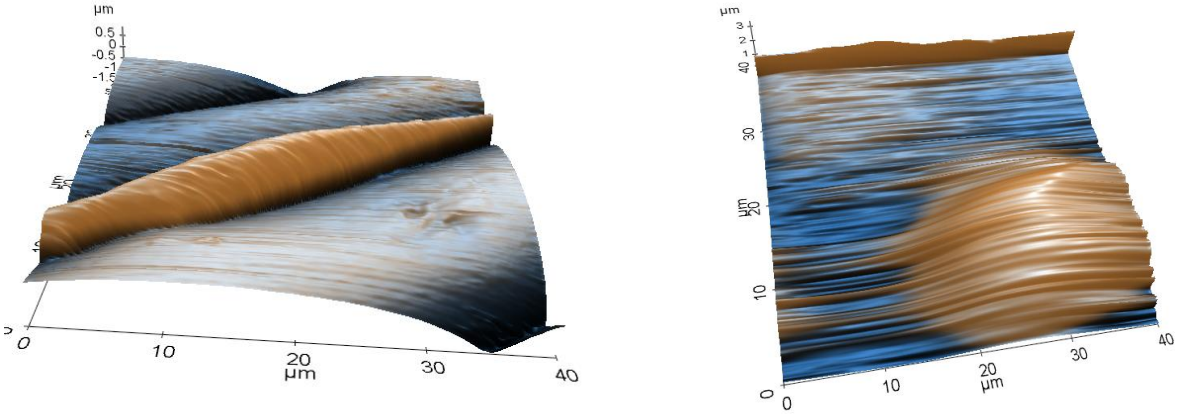

(a) **(b)**

Figure 36: 3D images of HECEs: (a) live cell (elongated shape) (b) dead cell (round shape)

During the AFM test, HCECs were kept inside the enclosure of AFM. The setup for live cells culture environment was demonstrated and shown in Figure 21 in subheading 3.4.2.3.2.

4.3.3 Data processing

The XEI software gives the possibility to derive the Young's modulus from force curves obtained from XEP software (two steps described in above section). Figure 37 shows the interface of force-displacement spectroscopy. The first step of the processing is to select the curves of designated spot. Then we need to find the contact point by dragging two cursors on F-D curve (one is on the top, the other is at the end of curve but ahead of flat line). The rest of steps are to set the tip shape, Poisson's ratio, and face angles. In our experiments, four-sided pyramid was selected as tip shape. Poisson's ratio was set to 0.5 since soft biological samples can be regarded as incompressible materials like rubber. Face angle was set to 9.21 which was measured from the SEM images shown in Figure 14.

After setting all the parameters, XEI can calculate the young's modulus via built-in functions. Those functions are based on Hertzian model that discussed in subheading 4.2.2.

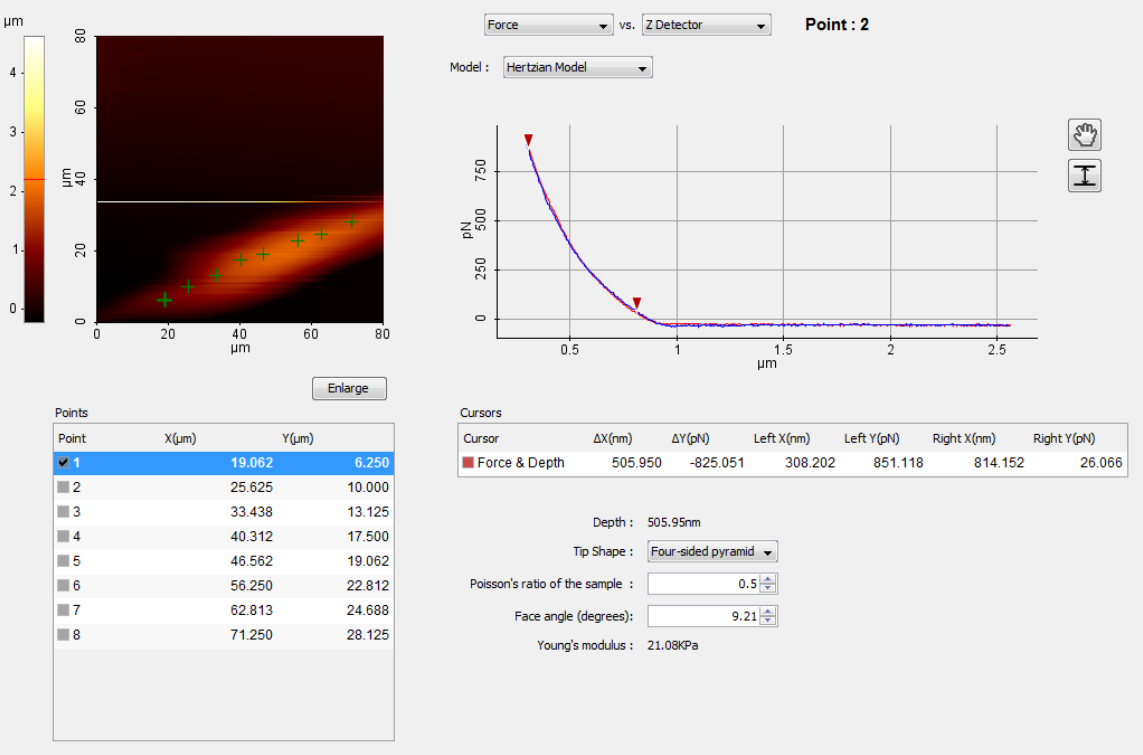

Figure 37: XEI data processing interface: calculating Young's modulus

4.4 Results and discussion

AFM topographic images were taken from four live HCECs and three dead HCECs (no dead cell was tested on glass cover slip). To investigate the effect of elastic modulus on HCECs behavior, those

five HCECs were cultured on different stiffness of substrate. Their young's modulus results were shown in Table 4.

Table 4: Elastic moduli of substrates

Location#	Soft (kPa)	Medium Stiff (kPa)	Very Stiff (kPa)	Glass (GPa)
1	1.08	5.11	69.48	9.33
2	0.904	4.22	81.59	11.24
3	0.813	7.66	89.51	9.7
4	0.938	7.8	76	10.21
5	0.916	6.24	86.54	
AVG:	0.9302	6.206	80.624	10.12

Following the steps described in section 4.3.2, elastic moduli at 4 to 6 different locations for each image were estimated from force-displacement curves using Hertzian model. Each force-displacement curve contains 1024 points of data with an indentation depth at a given tip force (512 points for extend trace and 512 points for retract trace). Taking one of five live HECEs as an example, various locations were selected by making cursors along cells (Figure 38(a)). For each position, there is one corresponding force-displacement curve giving the young's modulus result (Figure 38(b)).

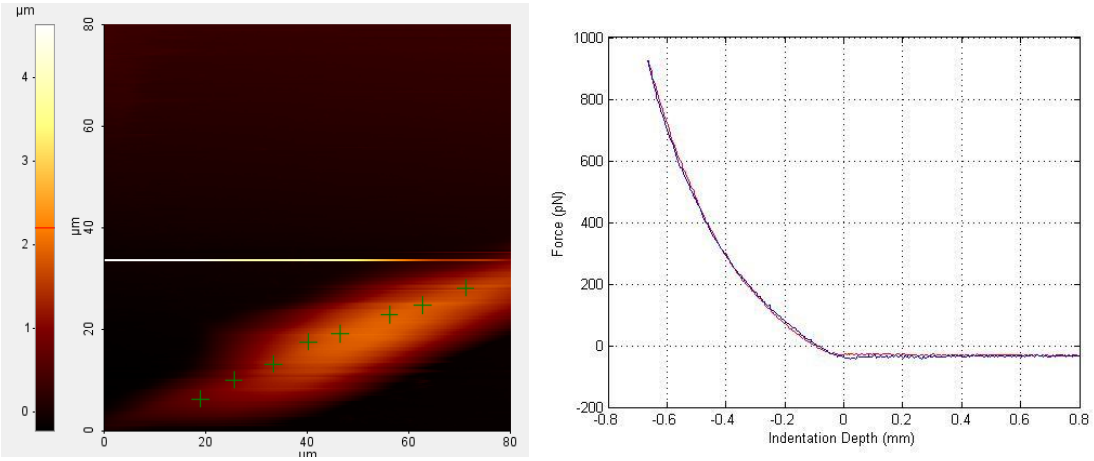

Figure 38: Example to show how force-displacement curves at various spots were generated.

Similar to the example shown in Figure 38, we obtained Young's modulus for the other four live HECEs, which is shown in Table 5.

Table 5: Elastic moduli of live HCECs (Unit: KPa)

Area of cells	Soft	Medium Stiff	Very Stiff	Glass
Outer Part	11.41 10.63	10.27 10.39	21.66 28.72	52.28 62.73
Outer AVG	11.02	10.33	25.19	57.505
Inner Part	8.72 5.96 6.66	9.39 8.52	16.63 14.41	44.97 44.67 48.54
Inner AVG	7.11	8.95	15.52	44.82

In order to show the results intuitively and make a comprehensive analysis of table 4 and table 5. We illustrate a three dimensional histogram in Matlab (as shown in Figure 39). The X, Y, Z axis respectively represents different parts of cells, young's modulus of substrates, and young's modulus of cells respectively.

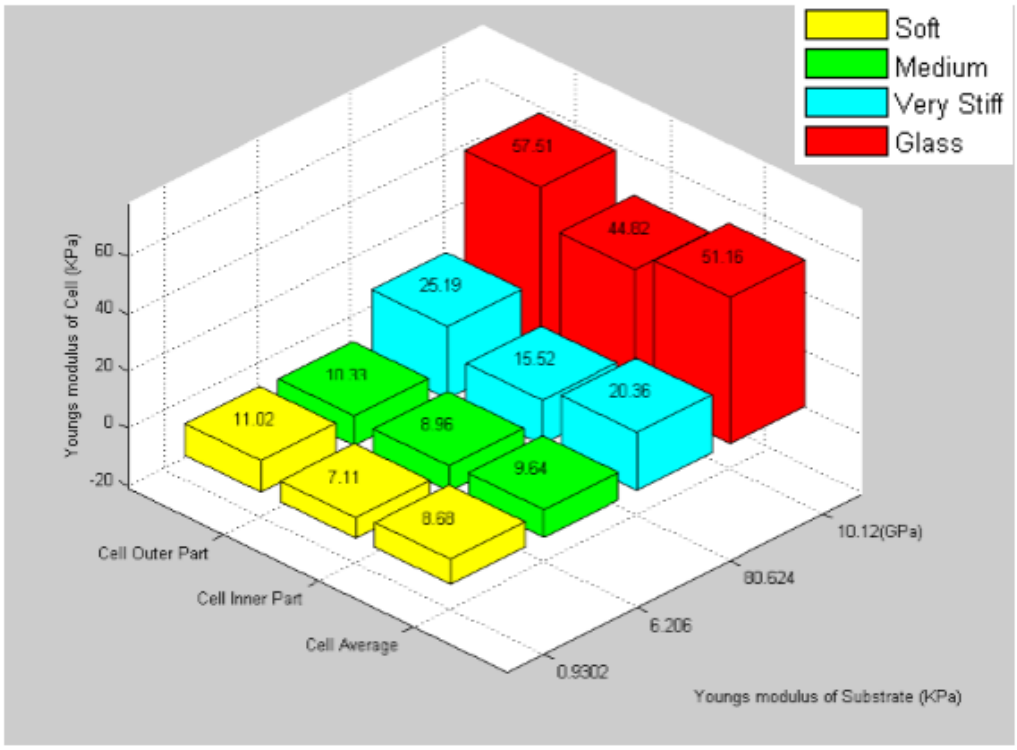

Figure 39: Histogram of Live HCECs elasticity results

As seen in the Figure 39, the elasticity varies along the body of HCECs. It can be easily found a trend that the outer part is higher than the inner part of the cell, which is due to the distribution of inner organization under cell membrane. On the other hand, we could also observe that the stiffness of Polyacrylamide (PAA) substrate do affect the elasticity of HCECs. This can also be explained by intrinsic properties of cells: stiffness sensing. "Stiffness sensing" means that cells have an ability to detect and respond to the mechanical resistivity of the extracellular environment. Stiffness sensing has been demonstrated in a variety of cell types including endothelial cells [75-77], smooth muscle cells [78, 79], and transformed cells [80, 81]. The ability to sense stiffness is partly dependent on actomyosin-generated contractility that is transmitted to the extracellular environment through transmembrane integrin receptors that, with a number of intracellular signaling and scaffold proteins, organize into focal adhesions. Cells, in turn, respond to the stiffness of their substrate by altering cytoskeletal organization (the h cell mechanical properties is mainly defined by membrane cytoskeleton); thereby, the stiffness of cells changes.

Three dead HECEs were also examined in order to make a comparison of stiffness between live and dead cells. Table 6 shows the young's modulus results of dead HCECs. The inner organization of cells changed dramatically because of the obvious deformation and transformation of live cell (from elongated shape to round shape).

Table 6: Elastic moduli of dead HECEs (Unit: KPa)

Location#	Soft	Medium Stiff	Very Stiff
1	20.01	69.48	99.31
2	32.04	81.89	102.24
3	49.51	89.51	103.31
AVG:	33.853	80.293	101.620

To have an integrated comparison between live and dead HCECs, we plotted two elastic moduli curves based on data shown in Table 5 and Table 6 (as shown in Figure 40). We found that the young's modulus of HCECs (cultured on three different substrate) increased 190%, 632%, and 400% respectively after the cells died. The trend of increase in young's modulus (after cell died) agrees with the situation of mouse embryonic stem cells (MESC) reported in Ladjal et al. [82] and ASCs reported in Kexiang Hu et al. [83]. Similar to live HCECs, the dead HCECs cultured on a stiffer substrate have a higher young's modulus value.

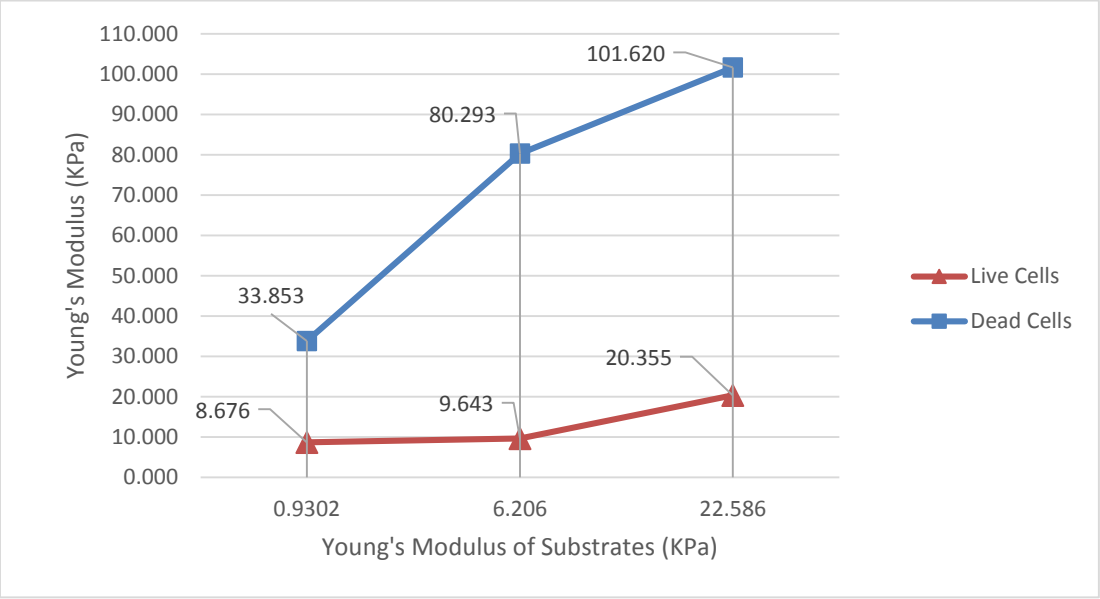

Figure 40: Comparison of live and dead HCECs

4.5 Conclusion

AFM probing of the whole cell is an effective tool for studying cell mechanics. Mechanical characterization of cells is so vital that it can be used to indicate cellular dysfunction and further disease progression. In our study, the mechanical characterization of HCECs has been divided into three parts: (i) measuring elastic modulus distribution across a single cell; (ii) comparing the elastic modulus difference between living cells and dead ones (iii) exploring the effect of Polyacrylamide (PAA) substrate (with different elastic moduli) on HCECs.

After analyzing the results, we obtained some key findings from each part mentioned above. Firstly, the stiffness of substrate influences the elasticity of HCECs. The higher the stiffness of substrate is, the higher the young's modulus of HCECs is. Secondly, the inner part of cell is less stiff than the outer part of cell. Both the results of inner part and outer part agree with the first finding (increasing cell stiffness with a stiffer substrate). The first and second finding is useful for making regenerative medicine strategies. A successful regenerative medicine strategy must consider the native mechanical environment so that they are able to elicit a favorable cellular response and integrate into the native tissue structure. The last key finding is that dead HCECs are stiffer than live ones. This is quite important to fundamental research on the differentiation of stem cells. In addition, cells have strict requirements on the culture environment; it is hard to keep them alive during differentiation. Thus,

distinguishing the dead and living stem cells is the prerequisite to carry out the investigation on differentiation process of the stem cells into specialized types of cells.

In future, the present study can be extended to make comparison between healthy and unhealthy HCECs, which can establish possible structure–mechanical property–disease connections in the context of disease using AFM.

Chapter 5
Conclusions and Recommendations

5.1 Conclusions

Two independent studies were performed in this thesis. In the first study, custom 2D digital image correlation (DIC) codes were developed to track certain patterns on materials and measure the deformation of sample in terms of strain or displacement. Supplementary algorithms (sub-pixel and smoothing algorithms) were also developed to enhance the accuracy of measurement. Developed codes were employed to atomic force microscopy (AFM) images for two applications:

(i) Determine the tracking ability of DIC applied on AFM images

DIC technique was further optimized for applications on AFM images regarding to referencing scheme, gridding function and displacement calculation. The selection of referencing scheme has a great effect on the accuracy of DIC results, and dynamic referencing scheme is more suitable than fixed referencing scheme in DIC analysis. The DIC technique was then applied to AFM images of solid and soft materials to verify the feasibility of codes. Through a complete error analysis, both image set validated the capability of DIC techniques applied on AFM images. But the results of solid materials are more closed to ideal results owing to the lower quality of soft materials images. Therefore, the tracking ability of DIC technique will be brought into play if good quality AFM images are provided.

(ii) Determining the deformation of live cells

Being different of static sample, live cells migrates and has a large deformation during its life cycle. A new algorithm was created in DIC method which could be applied to a large deformation of soft materials. A set of live cell images were achieved by AFM, where a life cycle of live cell could be observed. On account of limitation of infinitesimal strain theory (less than 10%), displacement vector was selected to reveal the trend of deformation across a large deformation region. The modified DIC technique and analysis method used here may be able to be applied to the studies of other elastomers, gels and biological tissues.

In the second study, the mechanical characterization of human corneal epithelial cells (HCECs) has been accomplished via making nanoindentation on live and dead HCECs. In elastic moduli measurement of live cells, the stiffness varies across the whole cell, where the inner part of cell is less

stiff than the outer part of cell. Moreover, we investigated whether changes in the elastic modulus of the substrate affected HCECs. Polyacrylamide (PAA) substrates with different elastic moduli (compliant, medium, and stiff) were prepared and HCECs were cultured on them. According to measurement, HCECs became stiffer in response to substrates with a higher elastic moduli. In the end, to carry out the investigation on differentiation process of HCECs in future, elastic moduli measurements were performed on dead HCECs as well. The measurement results clearly showed that dead HCECs are stiffer than live ones, which provided a more reliable way to distinguish live and dead cells.

5.2 Recommendations

For the future work, the following recommendations are suggested:

(i) In DIC-based strain or displacement measurement, smoothing algorithm was adopted to increase the accuracy of its performance in generating the field image. However, smoothing algorithm may distort the original data. Therefore, the effect of smoothing parameter that controls the degree of smoothing should be further investigated and optimized in the way that accuracy of tracking should be maximized while the distortion of the data be kept minimal.

(ii) The application of DIC technique on fixed cells performed worse than the one on ceramic surface due to poor image quality. The poorer image quality of fixed is mainly due to the floating objects inside PBS. Therefore, to solve this problem in further studies, one can try to scan the cells as soon as draining the PBS. Some paper indicated the cells can survive in 20 mins after draining the solution. Thus, the scanning can be proceeded in a semi-dry environment without the interference of impurity.

(iii) The impurity problem mentioned above is more severe in elastic moduli measurements of live cell. Not only the impurity comes from solution itself, but also comes from metabolism of cells. In addition to impurity, the cell migration also contributes to unreliable moduli results. For a more reliable and smooth operations in further studies, a technique known as mechanical trapping can be considered to apply to cells. The trapping technique could get rid of metabolin produced by other live cells. Furthermore, it can immobilize single, living cells in AFM experiments without the use of chemical immobilizers under physiological conditions in fluid; thereby, provide a robust indentation environment.

Bibliography

1. Hooke, Robert C. Micrographia: or Some Physiological Descriptions of Miniature Bodies Made by Magnifying Glasses. *London, England: Jo. Martyn, and Ja. Allestry*, (1665).
2. Maton, Anthea; Hopkins, Jean Johnson, Susan LaHart, David Quon Warner, Maryanna Wright, Jill D. *Cells Building Blocks of Life. New Jersey: Prentice Hall.* ISBN 0-13-423476-6. (1997)
3. Edward G. Ruestow , Images and ideas: Leeuwenhoek's perception of the spermatozoa, *Journal of the History of Biology,* 22, Volume 16, Issue 2, pp 185-224, (1983)
4. H.E. Huxley, Electron microscope studies of the organisation of the filaments in striated muscle, *Biochimica et Biophysica Acta,* Volume 12, Issues 1–2, October 1953, Pages 387–394, (1953)
5. Clinton J. Dawes, Flora Murray Scott and Edwin Bowler, Light and Electron Microscope Study of Cell Walls of Brown and Red Algae, *Science,* Page 1663 of 1663-1664, (1960)
6. N.J. de Both; J.M. van Dongen, B. van Hofwegen, J. Keulemans, W.J. Visser, H. Galjaard, The influence of various cell kinetic conditions on functional differentiation in the small intestine of the rat : A study of enzymes bound to subcellular organelles, *Developmental Biology*, Volume38(Issue1) Pagep.119To-137 (1974)
7. Jean Nofil BARBOTIN and Brigitte THO,MASSET. Immobilized organelles and whole cells into protein foam structures, *BIOCHIMIE*, 62, 359-365 (1980).
8. Gallo RC. "A reflection on HIV/AIDS research after 25 years". *Retrovirology* 3: 72. doi:10.1186/1742-4690-3-72. PMC 1629027. PMID 17054781 (2006)
9. Morris, V. J., Kirby, A. R., Gunning, A. P., Atomic Force Microscopy for Biologists, *World Scientific Publishing*, London (1999).
10. Radmacher, M. et al. From molecules to cells: imaging soft samples with the atomic force microscope. *Science* 257, 1900–1905 (1992)
11. Le Grimellec, C. et al. Imaging of the membrane surface of MDCK cells by atomic force microscopy. *Biophys*. J. 67, 36–41(1994)

12. Engel, A. and Gaub, H.E. Structure and mechanics of membrane proteins. *Annu. Rev. Biochem*. 77, 127–148 (2008)
13. Puchner, E.M. and Gaub, H.E. Force and function: probing proteins with AFM-based force spectroscopy. *Curr. Opin. Struct.* Biol. 19, 605–614 (2009)
14. Mu ¨ller, D.J. et al. Force probing surfaces of living cells to molecular resolution. *Nat. Chem.* Biol. 5, 383–390 (2009)
15. Sotomayor, M. and Schulten, K. Single-molecule experiments in vitro and in silico. *Science* 316, 1144–1148 (2007)
16. Neuman, K.C. and Nagy, A.K. Single-molecule force spectroscopy: optical tweezers, magnetic tweezers and atomic force microscopy. *Nat. Methods* 5, 491–505 (2008)
17. Dufreˆne, Y.F. et al. Five challenges to bringing single-molecule force spectroscopy into living cells. *Nat. Methods* 8, 123–127 (2011)
18. Vogel, V. and Sheetz, M. Local force and geometry sensing regulate cell functions. *Nat. Rev. Mol. Cell* Biol. 7, 265–275 (2006)
19. Dupres, V. et al. The yeast Wsc1 cell surface sensor behaves like a nanospring in vivo. *Nat. Chem.* Biol. 5, 857–862 (2009)
20. Krieg, M. et al. Tensile forces govern germ layer organization during gastrulation. *Nat. Cell* Biol. 10, 429–436 (2008)
21. Strilic´, B. et al. Electrostatic cell-surface repulsion initiates lumen formation in developing blood vessels. *Curr.* Biol. 20, 2003–2009 (2010)
22. Paluch, E. and Heisenberg, C-P. Biology and physics of cell shape changes in development. *Curr.* Biol. 19, R790–R799 (2009)
23. Kunda, P. and Baum, B. The actin cytoskeleton in spindle assembly and positioning. *Trends Cell* Biol. 19, 174–179 (2009)
24. Rotsch, C. and Radmacher, M. Drug-induced changes of cytoskeletal structure and mechanics in fibroblasts: An atomic force microscopy study. *Biophys. J.* 78, 520–535 (2000)

25. Cuerrier, C.M. et al. Real-time monitoring of angiotensin-II induced contractile response and cytoskeleton remodeling in individual cells by atomic force microscopy. *Pflugers* Arch. 457, 1361–1372 (2009)
26. Cuerrier, C.M. et al. Effect of thrombin and bradykinin on endothelial cell mechanical properties monitored through membrane deformation. *J. Mol. Recognit.* 22, 389–396 (2009)
27. David A.R. et al., Measurement of single-cell dynamics, *Nature* 465.7299, p736 (2010).
28. G. Gsell and J.J. Jonas, "Determination of the plastic behaviour of solid polymers at constant true strain rate," *Journal of materials science*, vol. 14, pp. 583-591 (1979).
29. R.D. Groot, A. Bot, and W.G.M. Agterof, "Molecular theory of strain hardening of a polymer gel: Application to gelatin," *The Journal of Chemical Physics*, vol. 104, pp. 9202-9219 (1996).
30. T.C. Chu, W.F. Ranson, and M. a Sutton, "Applications of digital-image-correlation techniques to experimental mechanics," *Experimental Mechanics*, vol. 25, Sep., pp. 232-244 (1985).
31. B.D. Lucas and T. Kanade, "An iterative image registration technique with an application to stereo vision," *Imaging*, vol. 130, pp. 121-129 (1981).
32. M. Kass, A. Witkin, and D. Terzopoulos, "Snakes: Active contour models," *International Journal of Computer Vision*, vol. 1, Jan., pp. 321-331 (1988).
33. N.P. Papanikolopoulos, "Selection of features and evaluation of visual measurements during robotic visual servoing tasks," *Journal of Intelligent & Robotic Systems*, vol. 13, pp. 279-304 (1995).
34. J. Lewis, "Fast template matching," *Vision Interface*, pp. 120–123 (1995).
35. M. Lekka, P. Laidler, D. Gil, J. Lekki, Z. Stachura, A.Z. Hrynkiewicz, Elasticity of normal and cancerous human bladder cells studied by scanning force microscopy, *Eur. Biophys*. J. 28 (4) 312–316 (1999)
36. Costa, K. D. Single-cell elastography: probing for disease with the atomic force microscope. *Dis. Markers* 19, 139–154 (2004).

37. Rosenbluth M.J., Lam W.A., Fletcher D.A.: Force microscopy of nonadherent cells: A comparison of leukemia cell deformability, *Biophy J* 90:2994-3003 (2006)
38. Docheva D.Padula D., Popov C., Mutschler W., Clausen-Schaumann H., Schieker M., Reasearching into the cellular shape, volume and elasticity of mesenchymal stem cells, osteoblasts and osteosarcoma cells by atomic force microscopy, *Journal of Cellular and Molecular Medicine* 12:537-552 (2007)
39. Chaudhuri, O. et al. Reversible stress softening of actin networks. *Nature* 445, 295–298 (2007)
40. Johnson, K. L, *Contact mechanics*, Cambridge University Press (1985)
41. W.C. Oliver and G.M. Pharr. "Measurement of hardness and elastic modulus by instrumented indentation: Advances in understanding and refinements to methodology". *Journal of Materials Research* 19: 3. doi:10.1557 (2011)
42. Binning, G. and Rohrer, H. Scanning tunneling microscopy. *Helv. Phys. Acta.*, 55, 726-735 (1982)
43. Park System Corporation, *XE-100 user manual*, [Online] Available at: http://www.parksystem.com (2010)
44. Park System Corporation, Park XE-Bio products introduction, [Online] Available at:http://www.parkafm.com/index.php/products/bio-afm-sicm/park-xe-bio/overview (2012)
45. Davide Ricci and Pier Carlo Braga, How the Atomic force microscope works, *Atomic Force Microscopy in Biomedical Research Methods in Molecular Biology* Volume 736, 2011, pp 3-18 (2011)
46. Wade, T., Garst, J. F., and Stickney, J. L., A simple modification of a commercial atomic force microscopy liquid cell for in situ imaging in organic, reactive or air sensitive environments. *Rev. Sci. Instr.* 70, 121–124. (1999)
47. Lehenkari, P. P., Charras, G. T., Nykanen, A., and Horton, M. A. Adapting atomic force microscopy for cell biology. *Ultramicroscopy* 82, 289–295 (2000).
48. Israelachvili, J. N. *Intermolecular and Surface Forces*, 2nd ed. Academic Press, London (1992).

49. F. Hild and S. Roux, “Digital Image Correlation: from displacement measurement to identification of elastic properties - a Review,” *Strain*, vol. 42, pp. 69-80 (2006).
50. R. Hamam, F. Hild, and S. Roux, “Stress Intensity Factor gauging by digital image correlation: application in cyclic fatigue,” *Strain*, vol. 43, pp. 181-192 (2007).
51. M.S. Kirugulige, H.V. Tippur, and T.S. Denney, “Measurement of transient deformations using digital image correlation method and high-speed photography: application to dynamic fracture,” *Applied optics*, vol. 46, pp. 5083-5096 (2007).
52. M.S. Thompson, H. Schell, J. Lienau, and G.N. Duda, “Digital image correlation: a technique for determining local mechanical conditions within early bone callus,” *Medical engineering & physics*, vol. 29, pp. 820-823 (2007).
53. D. Garcia, “Robust smoothing of gridded data in one and higher dimensions with missing values,” *Computational Statistics & Data Analysis*, vol. 54, pp. 1167-1178 (2010).
54. G. Wahba, “Spline Models for Observational Data,” *Society for Industrial and Applied Mathematics* (1990).
55. H.L. Weinert, “Efficient computation for Whittaker–Henderson smoothing,” *Computational Statistics & Data Analysis*, vol. 52, pp. 959-974 (2007).
56. W. Yueh, “Eigenvalues of several tridiagonal matrices,” *Applied Mathematics E-Notes*, vol. 5, pp. 66-74 (2005).
57. G. Strang, “The discrete cosine transform,” *SIAM Review*, vol. 41, p. 135 (1999).
58. Alexander, S., Hellemans, L., Marti, O., et al. An atomic-resolution atomicforce microscope implemented using an optical lever. *J. Appl. Phys*. 65, 164–167 (1989).
59. G.Y.H. Lee, C.T. Lim, Biomechanics approaches to studying human diseases, Trends *Biotechnol.* 25 (3) (2007) 111–118.
60. C.T. Lim, E.H. Zhou, A. Li, S.R.K. Vedula, H.X. Fu, Experimental techniques for single cell and single molecule biomechanics, *Mater. Sci. Eng. C—Biomimetic Supramol. Syst*. 26 (8) 1278–1288 (2006).
61. T.G. Kuznetsova, M.N. Starodubteseva, N.I. Yegorenkov, S.A. Chizhik, R.I. Zhdanov, Atomic force microscopy probing of cell elasticity, *Mircron* 38 824-833 (2007)

62. Miyazaki, H., Hasegawa, Y., and Hayashi, K. A newly designed tensile tester for cells and its application to fibroblasts. *J. Biomech*. 33, 97–104 (2000).
63. Wang, N., Butler, J. P., and Ingber, D. E. Mechanotransduction across the cell surface and through the cytoskeleton. *Science 260*, 1124–1127 (1993).
64. Yamada, S., Wirtz, D., and Kuo, S. C. Mechanics of living cells measured by laser tracking microrheology. *Biophys. J*. 78, 1736–1747 (2000)
65. Alenghat, F. J., Fabry, B., Tsai, K. Y., Goldmann, W. H., and Ingber, D. E. Analysis of cell mechanics in single vinculin-deficient cells using a magnetic tweezer. *Biochem. Biophys. Res. Commun*. 277, 93–99. (2000)
66. Guck, J., Ananthakrishnan, R., Mahmood, H., Moon, T. J., Cunningham, C. C., and Kas, J. The optical stretcher: a novel laser tool to micromanipulate cells. *Biophys. J*. 81, 767–784 (2001).
67. Petersen, N. O., McConnaughey, W. B., and Elson, E. L. Dependence of locally measured cellular deformability on position on the cell, temperature, and cytochalasin B. *Proc. Natl. Acad. Sci. USA* 79, 5327–5331 (1982).
68. Felder, S. and Elson, E. L. Mechanics of fibroblast locomotion: quantitative analysis of forces and motion at the leading lamellas of fibroblasts. *J. Cell Biol.* 111, 2513–2526 (1990).
69. Koay, E. J., Shieh, A. C., and Athanasiou, K. A. Creep indentation of single cells. *J. Biomech. Eng*. 125, 334–341 (2003).
70. H. Hertz, "On the contact of elastic solids," *JourTialfur die reine und angewandte Matlumatilc*, vol. 92, pp. 156-171 (1881).
71. J. Prescott, "Applied elasticity," *Longmans, Green and Co*, 1924.
72. O.D. Kellogg, "Foundations of potential theory," *New York: Murray Printng Company* (1929).
73. Q.S. Li, G.Y.H Lee, C.N, C.T. Lim, AFM indentation study of breast cancer cells, *Biochem Biophys Res com* 374:609-613 (2008)

74. Aratyn-Schaus Y, Oakes PW, Stricker J, Winter SP, Gardel ML. Preparation of complaint matrices for quantifying cellular contraction. *Journal of visualized experiments: JoVE* 2010.
75. Califano, J.P., Reinhart-King, C.A.: Substrate stiffness and cell area drive cellular traction stresses in single cells and cells in contact. *Cell. Mol. Bioeng.* 3(1), 68–75 (2010)
76. Deroanne, C.F., Lapiere, C.M., et al.: In vitro tubulogenesis of endothelial cells by relaxation of the coupling extracellular matrix-cytoskeleton. *Cardiovasc. Res*. 49(3), 647–658 (2001)
77. Reinhart-King, C.A., Dembo, M., et al.: Cell-Cell Mechanical Communication through Compliant Substrates. *Biophys.* J. 95(12), 6044–6051 (2008)
78. Engler, A., Bacakova, L., et al.: Substrate compliance versus ligand density in cell on gel responses. *Biophys*. J. 86(1 Pt 1), 617–628 (2004)
79. Isenberg, B.C., Dimilla, P.A., et al.: Vascular smooth muscle cell durotaxis depends on substrate stiffness gradient strength. *Biophysics J97(5)*, 1313–1322 (2009)
80. Levental, K.R., Yu, H., et al.: Matrix crosslinking forces tumor progression by enhancing integrin signaling. *Cell 139(5)*, 891–906 (2009)
81. Wang, H.B., Dembo, M., et al.: Substrate flexibility regulates growth and apoptosis of normal but not transformed cells. Am. J. Physiol. *Cell Physiol.* 279(5), C1345–C1350 (2000)
82. Ladjal H, Hanus JL, Pillarisetti A, et al. Atomic force microscopy-based single cell indentation: experimentation and finite element simulation. *IEEE/RSJ International Conference on Intelligent Robots and Systems, St. Louis, MO,* 10-15. New York: IEEE, pp.1326–1332 (2009)
83. Kexiang Hu, F.H Zhao, Q.K. Wang, mechanical characterization of living and dead undifferentiated human adipose-derived stem cells by using AFM, *Journal of engineering in medicine*, DOI:10.1177/0954411913503064 (2013)